STEADY-STATE AND TRANSIENT METHODS FOR MODELING CHEMICAL REACTIONS ON SUPPORTED CATALYSTS

by

Michael Roland Prairie

In Partial Fulfillment of the Requirements
for the Degree of
Doctor of Philosophy

1987

Department of Chemical Engineering
California Institute of Technology
Pasadena, California USA

(Submitted April 6, 1987)

To Richard R. Prairie, my father.

Without him I never would have been here (in more ways than one).

ACKNOWLEDGEMENTS

My Advisor

Professor James E. Bailey: Thank you for your support and guidance throughout this project. It was a pleasure working with you.

My Colleague

Brent H. Shanks: Our many discussions, arguments and collaborations added much toward a more enjoyable, educational, and productive stay at Caltech. Thanks Brent!

My Friends

Herman, Steve, and Dee: Oh did we have some fun! Let's never forget those times.

Mike Loewenberg: There are not as many pages in this thesis as it would take for me to express all you've meant to me. Friend, roommate, colleague, I've learned a lot from you. Thanks!

Karl Friehs(er): Through you I've seen new worlds and new possibilities. Let's try some of them, in Europe.

Kim Scharre: How I've grown since we met. I look in your eyes, I see my reflection, I like what I see. Star, I'll never be the same. Thanks.

My Family

Mom, Dad, Jenny, and Steve: You guys have been great! Infinite thanks for your support (and your money).

ABSTRACT

A systematic experimental strategy based on fluid-phase measurements is proposed for modeling dynamic behavior of heterogeneous catalytic reactions. The strategy utilizes steady-state rate, step-response, cycled-feedstream, and feedback-induced bifurcation techniques. Ethylene hydrogenation on Pt/Al_2O_3 was studied using this strategy. In addition, transmission infrared spectroscopy is applied to investigate support effects which accompany ethylene hydrogenation on Pt/Al_2O_3, and to the detailed study of CO adsorption, desorption and oxidation on Rh/Al_2O_3. The proposed experimental strategy combined with surface infrared spectroscopy provides a very powerful means for identification and validation of dynamic kinetic models.

Observed bifurcation behavior can be accurately attributed to a model for the catalytic reaction only if each dynamic element in the closed-loop experimental hardware is properly accounted for. Accordingly, time delay and feedback gain were the manipulated parameters in a feedback-induced bifurcation scheme aimed at validating a dynamic model for an experimental gas-phase reactor flow system without reaction. The apparatus consists of an isothermal, stirred, fixed-bed reactor, mass flow controllers, an infrared gas analysis system, and a computerized data acquisition and control system. Experimental bifurcations to sustained oscillations show that the stability of the reactor system is strongly influenced by delay. The relationships of time delay to Hopf bifurcation gains and frequencies provide a very sensitive basis for model comparisons.

Steady-state, step-response, feedback-induced Hopf bifurcation and forced concentration cycling experiments were applied to study ethylene hydrogenation over 0.05% Pt/Al_2O_3 at 80 °C. Step-response experiments indicate a time scale of 5000 s which is associated with chemisorbed hydrogen. Conversely, feedback-induced Hopf bifurcation data indicate this time scale to be on the order of 1 s in magnitude. In the overall strategy of dynamic modeling, the two techniques

are complementary since each inherently focuses on an opposite region in the spectrum of time scales for the reactor system. Cycling the feedstream composition resulted in improvement of the time-average reaction rate for the ethylene hydrogenation reaction compared to steady-state reactor operation.

Steady-state, step-response and Hopf bifurcation data are also presented for 0.5% Pt/Al_2O_3 at 30 °C and compared with results for the 0.05% Pt/Al_2O_3 catalyst. A single value of 2.5 s for the surface time constant associated with chemisorbed hydrogen is sufficient for modeling behavior on 0.5% Pt/Al_2O_3, whereas the lower-loaded 0.05% Pt/Al_2O_3 catalyst requires two very different values. In addition, the 0.5% catalyst was used to demonstrate the general result that small discrepancies between the actual and chosen reference steady state give rise to imperfect, cusp-like bifurcations. Steady-state bifurcation data are also shown to be useful for discriminating among rival kinetic models.

Ethylene hydrogenation on spillover-activated alumina is proposed as an explanation for the very slow transient behavior observed for 0.05% Pt/Al_2O_3. Transmission infrared spectroscopy was used to study hydrogen spillover dynamics on 0.05% Pt/Al_2O_3 at 80 °C via hydroxyl/deuteroxyl exchange. Ethylene in the gas-phase markedly slows the rate of spillover. The presence of ethylene likely reduces the concentration of platinum-adsorbed hydrogen adatoms, the precursors of hydrogen spilled onto alumina, due to catalytic hydrogenation on the platinum. Surface transport of hydrogen atoms on spillover-activated alumina is proposed as an explanation for the very slow transient behavior observed for ethylene hydrogenation on 0.05% Pt/Al_2O_3. Infrared spectra exhibit characteristics of both hydroxyl and deuteroxyl groups for reactor feed containing only D_2 and C_2H_4. This observation confirms the existence of a dissociative ethylene adsorption process.

A section of the thesis unrelated to ethylene hydrogenation investigates modeling applications of transmission infrared spectoscopy (TIR) by applying it to study adsorbed CO on Rh/Al_2O_3 during CO chemisorption, steady-state, step-response, and forced-cycling oxidation experiments at 900 torr. At 300 °C, the catalyst initially supported primarily a dicarbonyl CO species, but after use exhibited spectra characteristic of a surface mostly covered by linearly bound CO. A model that describes transient, diffusion-influenced CO adsorption and desorption for the supported catalyst is presented. It suggests that the CO desorption energy depends linearly on coverage, and that the magnitude of this dependence is a function of temperature. Observed rate dependence on bulk CO concentration for O_2 effluent levels of 0.5% and 0.25% is interpreted considering the effects of internal and external mass transport at 300 °C. Step-response and forced-cycling oxidation experiments across stoichiometric conditions exhibit oxygen and CO storage effects characteristic of CO oxidation catalysts. Data indicating autonomous oscillation of CO coverage and CO_2 production are also presented.

TABLE OF CONTENTS

CHAPTER 1

INTRODUCTION

Mathematical modeling of catalytic reaction kinetics is an area of chemical reaction engineering which continues to receive much attention. Along with achieving the primary goal of developing models useful for design, research in this area also produces sophisticated experimental techniques and introduces new problems which are very interesting from both practical and scientific points of view. The work reported in this thesis is aimed at examining some of the most modern experimental techniques being used for dynamic modeling of heterogeneous catalytic reaction kinetics. The methods applied represent a synthesis of steady-state, stimulus-response, and autonomous-dynamics approaches.

The primary difficulty in modeling catalytic reactions lies in the inability to observe adsorbed reaction intermediates whose existence, structure, chemistry and dynamics contribute greatly to overall behavior. Accordingly, researchers have developed sensitive techniques, based on direct and indirect evidence for adlayer characteristics, for deducing reaction mechanisms. Included in these techniques are direct spectroscopic measurements of adsorbed species (usually single-crystal, UHV studies), temperature programmed desorption (reduction, reaction), steady-state rate measurements as functions of gas composition and temperature, stimulus-response methods (step-response and cycled feed composition), and the utilization of sustained, autonomous transient behavior.

Ultra-high vacuum (UHV) techniques include methods for determining the existence of adsorbed intermediates, adsorption and desorption kinetics, activation energies, overall process energetics, adlayer (phase) structure, etc., and are most commonly applied to unsupported catalysts. Although UHV work demonstrates fundamentals of catalytic processes, these experiments do not necessarily agree with what is found for similar supported catalysts at more realistic operating conditions. The reasons for this disagreement are not well understood, and much research is devoted toward learning about this problem, which is the so-called *pressure gap*.

Recently, however, certain results from UHV studies have found application in the interpretation and modeling of behavior observed for supported systems operated at high pressure (in range of a few torr to one atmosphere.) In one example, phase transitions of a CO adlayer on single crystals which were observed by Ertl *et al.* (1982) collaborate the modeling work of Lynch *et al.* (1986) which accurately describes autonomous oscillations observed for CO oxidation on supported Pt catalysts in terms of phase transitions of the CO adlayer as a function of adsorbed oxygen concentration. In another study, Herz and Marin (1980) used parameters from the surface science literature in a mathematical model which accurately describes steady-state rate hysteresis data for CO oxidation on supported platinum. Their model is one of the first to successfully integrate surface science and applied catalysis results; its success is largely due to site exclusion properties which were incorporated in the model as a result of surface science observations.

The most powerful example in which UHV and higher-pressure results have found agreement is described in the collaborative effort of Oh *et al.* (1986). In this work, turnover number as a function of temperature and carbon monoxide pressure for alumina-supported Rh agree very well with UHV data for Rh(111). Also, data for both catalysts are well-described by a single model which includes structure-sensitive effects in the form of activation energy dependence on adsorbate coverages. In general, however, parameters and models from UHV studies cannot be directly applied, without first testing their validity, to higher-pressure reactions on supported catalysts.

Two classes of measurements are most commonly employed for studying the kinetics of reactions on supported catalysts. They encompass: (a) gas-phase composition measurements and (b) surface infrared measurements. Each of these classes can be applied in situations where external variables such as temperature, catalyst loading, pretreatment, metal precursor, and reactor

geometry are manipulated in order to study specific characteristics of the reaction in question.

In any work on supported catalysts, gas composition measurements are essential for determining reaction rates and the environment to which the catalyst is exposed. Unfortunately, the only connection between gas composition and adsorbed intermediates, from the point of view of observation, exists in hypothesized models for adsorption, desorption, and surface reaction. Therefore, due to nonuniqueness of nonlinear equations, it is quite possible that a model which correctly describes gas-phase behavior could be completely in error with respect to adlayer characteristics. Such a model is of limited value for design applications which require robustness in terms of the variety of conditions (e.g., temperature, pressure, gas composition, etc.) for which it should be valid. As a result, researchers continually search for new experimental methods aimed at sensitive model identification. Most new methods involve transient experiments which take advantage of the nonlinear, multi-time-scale behavior characteristic of many catalytic reactions.

The inadequacies of gas-phase measurements for inferring detailed kinetic models for supported catalysts can be overcome for some reactions using techniques of surface infrared spectroscopy. Transmission and reflectance infrared spectroscopies (dispersive and FTIR) allow for the direct observation of adsorbed intermediates on supported catalysts under reaction conditions. As early as 1957, Yang and Garland identified three forms of adsorbed CO on supported rhodium and postulated the linearly-bound, dicarbonyl, and bridge-bonded CO species. Similarly, infrared techniques have shown that linear and bridge-bonded CO are the predominant species on supported platinum. A few examples of systems studied using infrared spectroscopy include CO + NO on noble metals (Arai and Tominaga, 1976; Hecker and Bell, 1983), ethylene epoxidation on supported silver (Force and Bell, 1975), isocyanate formation on alumina (Hecker and Bell, 1984), and ethylene adsorption on supported platinum (Soma, 1979). Surface infrared experi-

ments invariably point out the extreme complexity of the catalytic reaction under study.

Using gas-phase composition and surface infrared measurements for studying catalytic reaction kinetics, the productivity of a particular modeling endeavor is limited by the types of experiments applied. Thus it is the task of the investigator to devise clever experiments for unraveling the significant details relevant to the development of an accurate model. A goal of the work presented here is to provide a well-defined experimental strategy, requiring equipment common in most catalysis laboratories, for dynamic model identification for a wide variety of reactions on supported catalysts.

The systematic investigation of steady-state kinetics is an important and necessary component of any strategy for catalytic modeling. However, because of important contributions of surface species dynamics, transient experiments must also be applied.

Much research has been devoted to utilizing transient methods for model identification. Step-response methods represent the simplest type of transient experiment and are useful for inferring qualitative features of the reaction network (Kobayashi; 1982a), estimating parameters (Kobayashi and Kobayashi, 1974; Shanks and Bailey, submitted), and discriminating among rival kinetic models (Kobayashi, 1982b; Feimer *et al.*, 1985). Another more powerful stimulus-response technique is forced periodic manipulation of external variables (e.g., temperature, feed composition, etc.) Since Bailey and Horn (1970) originally proposed using forced-cycling for discriminating rival mechanisms, the technique has seen widespread use (e.g., Barshad *et al.*, 1985; Cutlip *et al.*, 1983; Feimer *et al.*, 1982; Graham and Lynch, 1984; Lynch, 1984; Smith, 1983; Truffer and Renken, 1986). An excellent review on the subject of forced-cycling was written by Bailey (1977). Forced cycling not only provides a sensitive basis for model comparisons but also can indicate possibilities for productivity and/or selectivity enhancements via nonsteady operation.

Another category of experimental studies of transient kinetics arises from observations of sustained autonomous dynamics, such as periodic oscillations or chaos, which occur for steady inputs. Many explanations have been offered to account for the multitude of autonomous dynamics that have been observed; some of them are outlined in the review by Sheintuch and Schmitz (1977). The causes of oscillatory behavior give rise to nonlinear models which can be analyzed using bifurcation theory and computer simulation. Although quite powerful for dynamic modeling, observations of autonomous dynamics require that the system bifurcate naturally, and unfortunately this requirement is not satisfied for most catalytic reactions.

Systems that do not exhibit natural bifurcations can be referred to as *tame* systems. Tame systems can be forced to bifurcate by introducing feedback and then manipulating feedback gains in order to induce instability (e.g., steady-state multiplicity, Hopf bifurcation to harmonic oscillations, etc.) Nonlinear systems theory indicates that local dynamic behavior is intrinsically nonlinear at bifurcation, suggesting special significance of studies near bifurcation for sensitive model discrimination. Further, the possibility of bifurcation, and the conditions under which a model bifurcates, can be quite sensitive to the functional form of the model and certain parameters in the model.

Feedback-induced bifurcation for nonlinear model identification was first proposed by Kuszta and Bailey (1982) and later developed for catalytic kinetics by Lyberatos *et al.* (1984; 1985a,b). These workers (1984) showed that the loci of feedback gains which delimit a variety of bifurcations are distinctly different for two rival models representing NO_2 decomposition on nickel. Through simulation, these authors differentiated between two models which were difficult to distinguish based on steady-state and step-response data.

It was a goal of the work presented here to apply experimentally and evaluate the feasibility of the novel idea of feedback-induced bifurcation for catalysis studies. Much of the

theoretical foundation for the work here can be found in the doctoral dissertation of G. Lyberatos (1984).

Each type of experiment, namely steady-state rate determinations, step-response, forced concentration cycling, and feedback-induced bifurcation has potential for providing complementary kinds of information on the catalytic reaction system. It is the primary goal of this work to evaluate the merits and disadvantages of an experimental modeling scheme which uses all four methods. To that end the techniques were systematically applied to two catalytic reaction systems: (a) ethylene hydrogenation on Pt/Al_2O_3 and (b) carbon monoxide oxidation on Rh/Al_2O_3. Experiments were carried out using gas-phase composition measurements and infrared surface studies as described earlier. Specific details about each reaction are presented with more introductory material in the chapters that follow.

Each of the remaining chapters in this thesis, excluding Conclusions, is in itself a complete study concerning particular aspects of one of the model reactions as examined via one or more of the four techniques. Chapter 2 provides a complete description of the experimental system used throughout most of the work and examines the usefulness of the technique of feedback-induced bifurcation for model validation. Chapter 3 contains a detailed introduction on the philosophy of catalytic modeling and describes the application of steady-state rate, step-response, forced-cycling and feedback-induced bifurcation to ethylene hydrogenation on 0.05% Pt/Al_2O_3. This chapter also contains considerable details on the analysis of feedback-induced bifurcation data. Perfect and imperfect steady-state bifurcation are presented as a modeling tool and applied to ethylene hydrogenation on 0.5% Pt/Al_2O_3 in Chapter 4. Interesting questions which arose from the work presented in Chapters 3 and 4 prompted the infrared study of hydrogen spillover dynamics which is presented in Chapter 5. Finally, results from a transmission infrared study of carbon monoxide adsorption, desorption, and oxidation dynamics is presented in Chapter 6. This

work stresses the importance of noncatalytic effects such as internal and external mass transport limitations which typically arise in infrared studies. The underlying theme for the work in all of these chapters is, in addition to providing new information on the particular reaction being studied, the value of synthesizing information from several different types of experiments for investigating, understanding, and modeling catalytic kinetics.

REFERENCES

Arai, H., and H. Tominaga (1976). An infrared study of nitric oxide adsorbed on rhodium-alumina catalyst. *J. Catal.* **43,** 131-142.

Bailey, J.E. Periodic phenomena (1977). *Chemical Reactor Theory: A Review.* L. Lapidus and N. R. Amundson, Eds., Prentice-Hall, pp 758-813.

Bailey, J.E., and F. Horn (1970). Catalyst selectivity under steady-state and dynamic operation: an investigation of several kinetic mechanisms. *Ber. Bunsenges. Phys. Chem.,* **74,** 611-617.

Barshad, Y., X. Zhou, and E. Gulari (1985). Carbon monoxide oxidation under transient conditions: a FTIR spectroscopy study. *J. Catal.* **94,** 128-141.

Cutlip, M.B., C.J. Hawkins, D. Mukesh, W. Morton and C.N. Kenney (1983). Modelling of forced periodic oscillations of carbon monoxide oxidation over a platinum catalyst. *Chem. Engng. Commun.* **68,** 329-344.

Ertl, G., P.R. Norton, and J. Rustig (1982). Kinetic oscillations in platinum-catalyzed oxidation of CO. *Phys. Rev. Letters* **49,** 177-180.

Feimer, J.L., R.R. Hudgins, and P.L. Silveston (1985). Influence of forced cycling on the Fischer-Tropsch synthesis. Part III, a model for forced concentration cycling over promoted iron catalyst. *Canad. J. Chem. Eng.* **63,** 481-489.

Feimer, J.L., A.K. Jain, R.R. Hudgins, and P.L. Silveston (1982). Modelling forced periodic operation of catalytic reactors. *Chem. Engng. Sci.* **37,** 1797-1805.

Force, E.L., and A.T. Bell (1975). Infrared spectra of adsorbed species present during the oxidation of ethylene over silver. *J. Catal.* **38,** 440-460.

Graham, W.R.C., and D.T. Lynch Model validation through an experimental investigation of resonant behavior for the catalytic oxidation of carbon monoxide on platinum. In *Catalysis on the Energy Scene.* S. Kaliaguine and A. Mahay, Eds., Elsevier: Amsterdam, pp 197-204.

Hecker, W.C. and A.T. Bell (1983). Reduction of NO by CO over silica-supported rhodium: Infrared and kinetic studies. *J. Catal.* **84,** 200-215.

Hecker, W.C and A.T. Bell (1984). Infrared observations of Rh-NCO and Si-NCO species formed during the reduction of NO by CO over silica-supported rhodium. *J. Catal.* **85,** 389-397.

Herz, R.K., and S.P. Marin (1980). Surface chemistry models of carbon monoxide oxidation on supported platinum catalysts. *J. Catal.* **65,** 281-296.

Kobayashi, M. (1982a). Characterization of transient response curves in heterogeneous catalysis-I classification of the curves. *Chem. Engng. Sci.* **37,** 393-401.

Kobayashi, M. (1982b). Rival kinetic models in the oxidation of carbon monoxide over a silver catalyst by the transient response method. *Chemical Reaction Engineering-Boston,* J.Wei and C Georgakis, Eds., ACS Symposium Series, No. 196, pp 213-223.

Kobayashi, H., and Kobayashi, M. (1974). Transient response methods in heterogeneous catalysis. *Catal. Rev.-Sci. Engng.* **10,** 139-176.

Kuszta, B., and J. E.Bailey (1982). Nonlinear model identification by analysis of feedback-stimulated bifurcation. *IEEE Trans. Autom. Control* **AC-27,** 227-228.

Lyberatos, G. (1984) Dynamic and steady-state bifurcation for modeling chemical reaction systems. Doctoral dissertation, California Institute of Technology.

Lyberatos, G., B. Kuszta, and J.E. Bailey (1984). Discrimination and identification of dynamic catalytic models via introduction of feedback. *Chem. Engng. Sci.* **39,** 739-750.

Lyberatos, G., B. Kuszta, and J.E. Bailey (1985a). Normal forms for chemical reaction systems via the Affine transformation. *Chem. Engng. Sci.* **40,** 199-208.

Lyberatos, G., B. Kuszta, and J.E. Bailey (1985b). Versal families, normal forms, and higher order bifurcations in dynamic chemical systems. *Chem. Engng. Sci.* **40,** 1177-1189.

Lynch, D.T. (1984). On the use of adsorption/desorption models to describe the forced periodic operation of catalytic reactors. *Chem. Engng. Sci.* **39,** 1325-1328.

Lynch, D.T., G. Emig, and S.E. Wanke (1986). Oscillations during CO oxidation over supported metal catalysts. III. Mathematical modeling of the observed phenomena. *J. Catal.* **97,** 456-468.

Oh, S.H., G.B. Fisher, J.E. Carpenter, and D.W. Goodman (1986). Comparative kinetic studies of CO-O_2 and CO-NO reactions over single crystal and supported rhodium catalysts. *J. Catal.* **100,** 360-376.

Shanks, B.H., and J.E. Bailey. Modeling of slow dynamics in the oxidation of carbon monoxide over silver. Submitted to *AIChE J.*

Sheintuch, M., and R.A. Schmitz (1977). Oscillations in catalytic reactions. *Catal. Rev.-Sci. Eng.* **15,** 107-172.

Smith, C.B. (1983) Dynamic modelling and optimization of lumped chemical processes. Doctoral dissertation, University of Houston.

Soma, Y. (1979). Infrared spectra of ethylene adsorbed on transition metals at low temperature and hydrogenation of adsorbed species. *J. Catal.* **59,** 239-247.

Truffer, M.A., and A. Renken (1986). Transient behavior of heterogeneous catalytic reactions with educt inhibition. *AIChE J.* **32,** 1612-1620.

Yang, A.C., and C.W. Garland (1957). Infrared studies of carbon monoxide chemisorbed on rhodium. *J. Phys. Chem.* **61,** 1504-1512.

CHAPTER 2

INTENTIONAL MANIPULATION OF CLOSED-LOOP TIME DELAY FOR MODEL VALIDATION USING FEEDBACK-INDUCED BIFURCATION

INTRODUCTION

The use of external controllers for destabilizing laboratory chemical reactors to obtain sensitive bifurcation data has recently appeared in the chemical engineering literature as a promising modeling technique. An example of the usefulness of controller-destabilization for reactor modeling can be found in a recent article by McDermott *et al.* (1985). These workers were able to develop a very accurate model for the water-gas shift reaction in a fixed-bed, autothermal reactor based upon bifurcation points, steady-state data, and oscillation trajectories. In a more general framework, others have shown that static and dynamic feedback-induced bifurcation can be used for testing postulated kinetic models for catalytic reactions [Lyberatos *et al.*, 1984; Prairie and Bailey, 1986a,b]. Prairie and Bailey presented the experimental application of the technique to the study of ethylene hydrogenation over a supported platinum catalyst in an isothermal CSTR. Much of the analysis in that work rests on the presumption that each element in the closed-loop experimental system is adequately represented in the overall mathematical model describing the dynamic properties of the system.

The quality of information that can be derived using feedback-induced bifurcation to determine reaction kinetics is limited by the quality of the models used to describe the components that comprise the entire experimental apparatus. Thus, it is essential that a detailed analysis of closed-loop system dynamics be made in the absence of chemical reaction. The data presented here are results of a study of the system (without catalyst) which was used previously in the ethylene hydrogenation work.

A microcomputer controls the feed composition to an isothermal continuous stirred tank. Measurement of the effluent concentration of a single species is used to manipulate the feed. Accordingly, the feed delivery system, the gas transport system (tubing), the computer controller,

the tank, and the gas analysis system are the components that must be modeled. This goal is accomplished by performing individual open-loop experiments to arrive at independent mathematical expressions for the dynamic behavior of each component. These expressions are then combined to form one model that describes the entire closed-loop system. The ultimate test of the complete model is determined by its ability to describe data from feedback-induced bifurcation experiments. This paper provides the necessary experimental data to verify the postulated model and at the same time demonstrates the use of feedback-induced bifurcation experiments for testing dynamic models in both the frequency and time domains.

In a recent computational study, Lyberatos (1985) emphasizes the effect of delay on feedback identification of chemical reaction systems. In the experimental and modeling work presented here, this effect is exploited by manipulating delay as one of the bifurcation parameters. This results in Hopf bifurcations at a variety of frequencies, thus providing a powerful test of the proposed model.

In the absence of chemical reaction, the differential equation that describes the transient material balance for a two-component mixture in an isothermal, isobaric continuous stirred tank is one-dimensional, and, even with the addition of nonintegral feedback control, cannot, in general, admit dynamic (e.g., Hopf) bifurcations. Dynamic bifurcations can occur, however, if the feedback system contains any amount of time delay (e.g. transport lag, measurement lag, etc.). In this case, the one-dimensional material balance, which has one eigenvalue when linearized, takes on characteristics of a two-dimensional system (codimension 0 bifurcations, [Lyberatos *et al.*, 1984]). Even the slightest amount of delay produces an infinite eigenvalue spectrum. A continuous stirred tank without reaction but with feedback and delay can, for the proper value of the feedback gain, undergo Hopf bifurcation.

EXPERIMENTAL

Apparatus

The experimental system described here was designed and constructed by C. B. Smith (1983). A schematic diagram of the gas flow system is presented in Fig. 1. Two sets of mass flow controllers regulate the flow rates of helium (0 - 200 sccm), ethylene (0 - 20 sccm), hydrogen (0 - 20 sccm), and oxygen (0 - 20 sccm). The gases mix in line before the two streams flow into a valve system that selects one stream for flow into the reactor, and the other for flow into the vent line. The positions of the two low-volume solenoid valves (General Valve, part no. 1-35-900) that make up the switching system can be selected manually or with the computer control system. Pressure losses in the vent and reactor feed streams are equilibrated using an adjustable needle valve in the vent stream. Thus it is possible to avoid pressure surges that would normally occur upon switching from one feedstream to the other. Reactor effluent and vent streams enter another switching valve that selects one stream for infrared analysis. All tubing in the flow system is 1.59 mm (1/16 in.) OD thin-walled stainless steel.

A Wilkes Miran I infrared analyzer is equiped with a micro flow cell (0.35 cm^3) to continuously monitor the concentration of a single IR active component in either the reactor effluent or bypass streams. Voltage signals are related to mole fractions through empirical calibrations and are digitized and recorded with a Hewlett Packard 9825A data acquisition and control (DAC) system. Calibration curves have been determined at 10.4 μm for a variety of ethylene concentrations by recording the steady-state IR absorbance (voltage) for each concentration. These data were then fit to a simple empirical expression that is used for all conversions from IR absorbances to gas-phase mole fractions (constant temperature and pressure).

The DAC system is used to control mass flow controller set points, either interactively, at the user's command, or automatically as a user-defined function of any measureable variable(s), usually the IR analyzer voltage. During closed-loop operation, coded subroutines manipulate mass flow controller set points according to the IR signal in real time. Typically, data acquisition and control is implemented at 4 Hz. It was determined experimentally that operating the DAC system at higher sampling rates does not effect the performance of the closed-loop system. The microcomputer is also used to switch between the two feedstreams for step-response and cycled-feedstream experiments, and to select the effluent or vent streams for IR analysis.

Figure 2 shows an approximate view of the reactor cross-section. The entire reactor is constructed from stainless steel except for aluminum gaskets located at either end of the catalyst bed. Feed gas is directed through a 1.59 mm (1/16 in.) stainless steel tube to the center of a magnetically driven 6-blade impeller rotating at approximately 3000 rpm. The impeller is magnetically coupled to its drive motor, and the entire coupling system is isolated from the surrounding atmosphere [Smith, 1983]. Reactor effluent is withdrawn through another 1.59 mm (1/16 in.) stainless steel tube located at the top of the bed. In this configuration, the reactor, when packed with catalyst or 2 mm dia. glass beads, provides excellent internal mixing as determined by its exponential response to step changes in feed composition.

An annular region, approximately 5.8 cm^3 in volume, constitutes the catalyst bed which is separated from the rest of the reactor cavity by stainless steel screens. Under reaction conditions, the bed is loaded with catalyst particles mixed with 2 mm dia. Pyrex beads. However, the aim of the work described here is the study of the experimental system without reaction, so the reactor bed was loaded with Pyrex beads only. Two thermocouples are located within the catalyst bed. One is located approximately one-quarter of the way into the bed and is used soley for monitoring bed temperture. The other thermocouple sits approximately in the center of the bed and is

used for feedback control of the reactor bed temperature. The signal from this thermocouple is compared against a set point in a PI heater controller that supplies power to eight heating cartridges located in a large aluminum heatsink that surrounds the reactor. With the temperature controller it is possible to control the bed temperature up to 400 °C. The two thermocouples together provide an indication of axial temperature gradients.

A block diagram for the closed-loop experimental system is shown in Fig. 3. Here all state and manipulated variables are presented in vector notation for generality, although in the simple stirred tank configuration ethylene mole fraction is the only variable considered. In Fig. 3, $\mathbf{G_c}$ is the transfer function for the linearized contol algorithm, $\mathbf{G_{mfc}}$ is the transfer function for the mass flow controllers, and $\mathbf{G_p}$ is the transfer function for the linearized reactor (with or without reaction). The transfer function for delay in the measurement system is included as $e^{-\tau_D s}$. Delay only applies to gas-phase state variables for multidimensional analyses. Individual elements in the transfer function matrices **G** will be denoted with lower case g.

Methods

The discussion on the experimental apparatus has identified the major dynamic elements in the closed-loop system. They are (1) the mass flow controllers, (2) the reactor, (3) the IR analyzer, and (4) the computer controller and control algorithm, in addition to transport lag encountered between the flow controllers and the IR analyzer. This section first describes the experiments performed to characterize each of these elements in terms of a mathematical model. Then, the methods used for conducting the feedback-induced Hopf bifurcation experiments are summarized.

Mass flow controllers: The mass flow controllers were manufactured by Tylan Corporation (model FC-260). They regulate mass flow rate in response to an externally supplied voltage.

The mass flow controllers are individual feedback control units nested within the closed-loop reactor system. Their complexity and limited flow ranges undoubtedly endows them with non-linear features. However, over the frequency range of interest, it will be shown that the mass flow controllers can be adequately described with transfer functions for linear systems.

It is desired that the total molar feed rate, F_T, and hence the system transport lag, τ_D, and the reactor residence time, τ, remain constant. Accordingly, manipulations of reactant flow rates are always accompanied by compensating manipulations of the helium flow rate. Hence, the transient responses of the reactant mass flow controllers and the total flow rate to changes in set points must be characterized. This has been accomplished through the use of frequency response experiments.

Transfer functions for the mass flow controllers have been obtained by sinusoidal forcing of their set points according to $A + \alpha\sin\omega t$ over the frequency range $0 \leq \omega \leq 2$ rad/s. Monitoring the indicated flow rate as a function of time and comparing it with the input forcing function provides data for the amplitude ratio $AR(\omega)$ and the phase shift $\Phi(\omega)$ for construction of empirical transfer functions in the frequency domain

$$g_{mfc}(\omega) = AR(\omega)\exp[i\,\Phi(\omega)], \tag{1}$$

assuming linearity. The frequency response for each reactant mass flow controller is obtained individually, so only its set point and that of the helium mass flow controller are manipulated for any one experiment. These experiments are performed for total flow rates, temperatures and pressures that closely resemble conditions encountered during the feedback-induced bifurcation experiments. A very important parameter affecting the frequency response of the mass flow controllers is the upstream, gas-cylinder regulator pressure. Experimentation proved 30 psig to be a satisfactory inlet pressure at which to operate the controllers. The frequency response for the total flow rate is estimated by summing the indicated flow rates of the test and the helium mass

flow controllers. Ideally this quantity should be time-independent and always sum to the target value F_T.

The reactor: Residence time distribution experiments, in which the reactor reponse to a step change in a tracer concentration is determined, pose a reasonable test of reactor mixing dynamics. Step-response experiments also yield excellent estimates of transport lag between the mass flow controllers and the IR analysis system. Unfortunately, the contribution to observed step-response profiles by the IR analyzer/flow cell combination is difficult to extricate. This issue is addressed in a later section.

Step-response experiments are performed by setting one feedstream to contain pure helium, and the other to contain 10% ethylene in helium. Both streams flow at the same total flow rate. Reactor pressure drop is accounted for in the bypass line by fine tuning of the needle valve. The feedstream to the reactor is switched from the helium stream to the 10% ethylene stream and the ethylene concentration in the reactor effluent is monitored on the IR analyzer and recorded digitally at 10 Hz for 60 s. These experiments were performed for *two* total feed rates, 50 and 100 sccm. The volumetric flow units of sccm can be directly converted to molar flow units of mol/min with the conversion 22400 sccm = 1 mol/min.

The IR analyzer: The IR analyzer has basically two ways of contributing to system dynamics. First, and most importantly, the mixing within the flow cell and the averaging nature of a beam passing through the cell both affect dynamic behavior, probably as a stirred tank affects system dynamics. Secondly, filtering electronics in the analyzer tend to smooth fast transients.

The flow cell has 0.35 cm^3 internal volume which translates into a time constant of 0.2 s for a total flow rate of 100 sccm, at room temperature and pressure (in comparison to 4.7 s for the reactor at similar conditions). The dynamics of the IR analyzer/flow cell combination were determined by imposing switching experiments (similar to those described for the reactor) on the flow

system having bypassed the reactor with a 7.6 cm (3 in.) length of 1.59 mm (1/16 in.) dia. stainless steel tubing.

The controller: The versatility of the microcomputer controlled DAC system allows for nearly any control algorithm to be used to manipulate flow controller set points as functions of the IR analyzer signal. For the feedback experiments described here, and for those presented elsewhere [Prairie and Bailey, 1986a,b], the arctangent function is used as the feedback control algorithm. This function allows for direct representation of controller saturation, is continuous and differentiable over the range considered, and exhibits proportional response for small deviations from the set point. Thus, the ethylene feed rate, F_e^i, is manipulated based on the effluent ethylene mole fraction, x, according to

$$F_e^i = F_e^{ref} + \frac{2w}{\pi} \mathrm{Tan}^{-1}\left[u_e(x - x^{ref}) \right]. \qquad (2)$$

Here F_e^{ref} is the reference ethylene flow rate that results in the ethylene effluent mole fraction x^{ref}. The feedback gain u_e is analogous to a proportional controller gain, and in fact, is equivalent (within a multiple of $\frac{2w}{\pi}$) to a proportional controller gain locally near the reference condition. The variable w has the units of sccm and is the half-width of the arctangent feedback function. Transport lag in the experimental system requires that, for modeling purposes, x in Eq. (2) be replaced by the delayed value $x(t - \tau_D)$. Furthermore, to assure constant total flow rate, the helium feed rate, F_{He}^i, is manipulated according to $F_{He}^i = F_T - F_e^i$.

Feedback-induced bifurcation experiments: Hopf instability for the reference steady state occurs when feedback gain and time delay are such that the leading eigenvalues of the linearized system form a complex conjugate pair crossing the imaginary axis into the right-half plane. At the point of Hopf bifurcation, the parameters u_e, τ_D, and the Hopf bifurcation frequency, ω, can be related to the model and system parameters through simple relationships

derived from the characteristic equation.

The locus of Hopf bifurcation points in the τ_D versus u_e parameter plane and the accompanying frequency plot (ω versus τ_D) can be obtained experimentally and then compared to model calculations. If the two agree over a wide range of frequency space for the stirred tank without reaction, it can safely be assumed that the system model provides an accurate description of the closed-loop experimental apparatus. When such a model is obtained for the experimental system, bifurcation behavior observed for the system when it supports catalytic reaction can confidently be attributed to the reaction itself and hence related to a mathematical model for the reaction.

Hopf bifurcation experiments were performed for two total flow rates (50 and 100 sccm) and hence for two reactor residence times at 26 °C and ambient pressure. At each flow rate, seven Hopf bifurcation points were located in (τ_D,u_e) parameter space, along with their corresponding bifurcation frequencies. For all of these experiments, w is 5 sccm, and x^{ref} is 0.10 (*i.e.*, F_e^{ref} = 10 sccm for F_T = 100 sccm and F_e^{ref} = 5 sccm when F_T = 50 sccm).

Each point of Hopf bifurcation is located by manipulating u_e for a fixed value of τ_D until the reference steady state loses stability and the ethylene mole fraction in the reactor effluent begins to exhibit sustained oscillations. Time delay is experimentally manipulated by using an array of variable length in the control subroutine. The floating array stores measured values of x with the most recent value entering the array while the oldest value is being used to implement arctangent control. Computer-generated time delay adds to the intrinsic system transport lag which is a linear function of total flow rate. Hence, time delays that can be implemented experimentally are bounded from below by the naturally occurring transport lag.

RESULTS AND MODELING

Mass flow controllers: Figure 4 shows the ethylene mass flow controller (MFC 6) response to sinusoidal forcing at a period of 4.4 s (ω = 1.43 rad/s). In the figure, the forcing function (broken) is compared against the indicated flow rate (solid) for sinusoidal forcing centered around A = 10 sccm with an amplitude, α, of 1 sccm. The figure shows that the ethylene mass flow controller experiences an amplitude ratio of 0.95 and a phase shift of -0.571 rad for a forcing period of 4.4 s. During this and all frequency response experiments, the total flow rate was held constant at 100 sccm by manipulating the helium flow controller (MFC 5) according to $F_{He}^{i} = 100 - A - \alpha\sin\omega t$. At all frequencies, the indicated total flow rate never deviated by more than 2% from the ideal value, F_T. Another consideration is the question of whether the indicated flow rate provides a true reflection of the actual flow rate. To study this a bubble flow meter was placed in the effluent line and the actual flow rate was monitored by eye during the sinusoidal forcing experiments. For the frequency range of interest, the actual flow rate is equal to the indicated flow rate, although operation at higher frequencies (ω greater than approximately 0.5 Hz) resulted in jumpy actual flow rates corresponding to erroneous indicated values.

Experiments were performed for 11 periods ranging between π s and 60 s corresponding to a frequency range of 2 rad/s to 0.11 rad/s. This frequency range encompasses the entire spectrum of oscillation frequencies that was encountered during the Hopf bifurcation experiments. For this range of frequencies, the ethylene mass flow controller always produced an amplitude ratio between 0.95 and 1.0, so the value of unity was adopted. Phase shift response is shown in Fig. 5. The linearity of the data indicates that the transfer function for the mass flow controller can be adequately modeled as a pure delay of 0.39 s. Hence the transfer function is

$$g_{mfc6}(\omega) = e^{-0.39\omega i} \tag{3}$$

Transfer functions for the other mass flow controllers were also determined using this technique and are presented in other papers where relevant [Prairie and Bailey, 1986a,b].

The model presented in Eqs. (1) and (3) assumes that the mass flow controllers exhibit behavior characteristic of linear devices. Sinsoidal forcing always results in sinusoidal output at the same frequency as the forcing function. This observation indicates that the assumption of linearity is probably valid for the frequency range of interest.

Step-response experiments for the reactor and IR analyzer: Figure 6 shows experimental and calculated step-response profiles for the the reactor/IR analyzer/flow cell system at 25 °C and two different total flow rates, F_T = 50 and 100 sccm. In this figure, time 0 indicates when the feed was switched from pure helium to 10% ethylene in helium. For F_T = 50 sccm, the reactor exhibits a time constant of 8.8 s(based on a linear fit of $\ln\frac{x}{x_\infty}$ versus t). Similarly, when F_T = 100 sccm, a reactor time constant of 4.7 s is observed. The sharp rise of effluent concentration at the times indicated by $\tau_{D,50}$ and $\tau_{D,100}$ suggest little contribution from higher-order effects, an observation which supports the assumption that the IR analyzer contributes negligibly to overall dynamics. Inherent system transport lags of τ_D = 4.5 s and 3.0 s are indicated for the total flow rates of 50 sccm and 100 sccm, respectively.

It is seen that the estimated reactor residence times do not exhibit simple inverse proportionality (the ratio of τ's is 0.534). This discrepancy is a result of pressure effects. As the total feed rate increases, so does the reactor pressure (the mass flow conroller valves open wider), and hence the molar capacity of the tank increases. This results in a larger residence time for larger flow rates in comparison to that obtained for smaller flow rates. The estimated residence times indicate that the reactor pressure increased by 7% between the 50 sccm and 100 sccm experi-

ments. The inherent transport lags also do not exhibit simple inverse proportionality. This is a result of pressure effects and flow rate-independent delays that arise in the IR analyzer and DAC systems.

Also shown in Fig. 6 is the step-response for the IR analyzer/flow cell combination, having bypassed the reactor with 1.59 mm (1/16 in.) dia. tubing. The very fast response of the IR system in comparison to the observed CSTR dynamics indicates that the IR system may be assumed to be a quasi-steady state device in the overall model for the system.

The excellent fit of the ideal CSTR model to the observed step-response data indicates that an appropriate ethylene balance on the reactor (constant τ) is

$$\tau\frac{dx}{dt} = x_i - x \tag{4}$$

where subscript i denotes an inlet mole fraction and the reactor time constant τ is the total molar capacity of the reactor divided by the total molar feed rate. From this a transfer function can be derived

$$g_p = \frac{1}{\tau s + 1}. \tag{5}$$

The model: A time-domain model for the closed-loop system can now be written

$$\tau\frac{dx(t)}{dt} = x^{ref} + \frac{2w}{F_T\pi}\mathrm{Tan}^{-1}\left[u_e(x(t-\tau_D-0.39)-x^{ref})\right] - x(t) \tag{6}$$

along with the overall transfer function

$$G = \frac{\frac{2w}{F_T\pi}u_e e^{-0.39s}}{1+\tau s+\frac{2w}{F_T\pi}u_e e^{-(\tau_D+0.39)s}} \tag{7}$$

which provides the characteristic function

$$p(s) = 1 + \tau s + \frac{2w}{F_T \pi} u_e e^{-(\tau_D + 0.39)s}. \quad (8)$$

In Eq. (6), $x(t - \tau_D - 0.39)$ denotes the reactor effluent mole fraction $\tau_D + 0.39$ s after time t. The term τ_D accounts for transport lag and 0.39 s accounts for delay within the ethylene mass flow controller.

Hopf bifurcation: The progress of typical Hopf bifurcation experiments is shown in Fig 7. Computer simulations shown in this figure will be described later. Fig. 7a shows measured values of the ethylene deviation variable, $x - x^{ref}$, for $\tau_D = 8$ s and $F_T = 50$ sccm. For these operating conditions, Hopf bifurcation occurs for u_e between -35 and -40 at a frequency , ω, of 0.25 rad/s. Data for $\tau_D = 16$ s and $F_T = 100$ sccm are shown in Fig. 7b. Here the estimated Hopf bifurcation gain is -38 and $\omega = 0.14$ rad/s. Each frame in Figs. 7a and b presents ethylene effluent data for the last three minutes in a 10 minute run at the indicated u_e.

Similar experiments were performed for seven different time delays at each total flow rate. Observed Hopf bifurcation gains are presented in the time delay/bifurcation gain parameter space in Fig. 8. Bifurcation frequency data are displayed in Fig. 9.

The solid and broken curves in Figs. 8 and 9 are model calculations for $F_T = 100$ sccm and 50 sccm, respectively. As was described earlier, Hopf bifurcation occurs when a leading pair of complex conjugate eigenvalues crosses the imaginary axis into the right-half side of the complex plane. This condition is expressed by setting the characteristic function given in Eq. (8) equal to zero, thus relating all system eigenvalues to τ_D, τ, u_e, F_T, and w. At Hopf bifurcation, the condition $p(i\omega) = 0$ must be satisfied. From this condition on Eq. (8) the Hopf bifurcation curve is derived

$$u_e = -\frac{F_T \pi}{2w}\sqrt{1+\tau^2\omega^2} \tag{9}$$

$$\tau_D = \frac{1}{\omega}\left[-0.39 - \mathrm{Tan}^{-1}(\tau\omega)\right] \pm \frac{n\pi}{\omega} \quad n = 0,1,2,... \tag{10}$$

These equations locate curves in the τ_D versus u_e plane which are parametric in $\omega(>0)$. The curves in Figs. 8 and 9 were calculated by picking ω and plotting τ_D against u_e and ω against τ_D, respectively. The term $\frac{n\pi}{\omega}$ arises from the multivalued nature of arctangent function. The case n=1 corresponds to leading eigenvalues, and hence to bifurcation. All other values of n correspond to the crossing of pairs of eigenvalues that have smaller real parts than the leading eigenvalue(s), and hence do not correspond to bifurcation.

The vertical lines on the right-hand side of Fig. 8 indicate the steady-state bifurcation condition [Prairie and Bailey, 1986a]. The reference steady state is unstable and steady-state multiplicity is observed for feedback gains to the right of these lines which occur at $u_e = \frac{F_T \pi}{2w}$. As expected, steady-state bifurcation is not a function of time delay. To the left of the Hopf curves the reference steady state is unstable and sustained oscillations are observed. These oscillations would not be possible without time delay. The reference steady state is stable only in the regions bounded by the Hopf curves and the steady-state bifurcation lines. Experimental verification of the position of the steady-state bifurcation lines is presented in an earlier publication [Prairie and Bailey, 1986a].

The Hopf bifurcation curves exhibit some interesting features. For small τ_D, the system is stable to large gains and bifurcations in this region of parameter space result in very high frequency oscillations. The Hopf bifurcation gain is relatively independent of τ_D for large delay time, and bifurcation at these conditions results in rather low frequency oscillations. Also, notice that the system has a larger region of stability for larger F_T.

The good agreement between the observed and calculated bifurcation boundaries and the excellent agreement between observed and calculated bifurcation frequencies indicate that the Laplace domain model of Eq. (7) provides an excellent description of the linearized closed-loop system.

Simulations: In the preceding paragraphs, the experimentally determined Hopf bifurcation points are compared with those obtained by solving the model equations in the frequency domain. This comparison requires the experimental system with discrete sampling (4 Hz) to be closely approximated by a continuous model. To test the validity of this assumption, simulations of the feedback-induced bifurcation experiments were performed. Equation (6) was solved using DGEAR, an IMSL subroutine. By solving Eq. (6) for different sampling discretizations (≥4 Hz), it was ascertained for the range of oscillation periods observed in this study that the sampling rate employed in the experiments yielded analogous results with respect to the continuous case.

The simulations also provide a means for examining the effect of noise on the bifurcation point and oscillation frequency. Random noise in levels of ± 0.5, 1.0, 1.5, and 2.5% of the reference effluent ethylene concentration were used. Although some minor changes in the qualitative features were observed for different levels of noise, the simulations showed the bifurcation point and resulting limit cycle period to be relatively independent of noise level. Bifurcation points for small time delays are more difficult to locate precisely when noise is included because oscillation amplitudes are much smaller than those for larger time delays. The effect of offset in the programmed reference ethylene concentration from the true reference value was also investigated using model simulations. Hopf bifurcation behavior is relatively insensitive to this type of parameter variation.

Figure 7c and d present simulation results for operating conditions used in the experiments presented in Fig. 7a and b, respectively. The simulations exactly duplicate the experiments in

terms of discretization rate and duration of run and include random noise with maximum amplitude of ±1.5% of the reference measurement. As can be seen from the figure, the dynamic simulations provide excellent reproductions of the experimental data. It is concluded that the time-domain model, as well as the transfer function model, pose excellent descriptions of the closed-loop experimental CSTR system without reaction.

CONCLUSIONS

Manipulating closed-loop time delay provides an effective method for stimulating Hopf bifurcations of the one-dimensional stirred tank without reaction. Without delay, these bifurcations would not occur. Experimental bifurcation diagrams in time delay versus feedback gain space are easily generated and provide an excellent test of the validity of a mathematical model for the process. Through this technique, the validity of models in the frequency and time domains which describe the dynamic behavior of the components of the experimental reactor system has been demonstrated. The resulting closed-loop model can be extended with confidence to describe the experimental apparatus in the context of bifurcation experiments which include the effects of catalytic reaction.

NOTATION

A	Mean flow rate for sinusoidal forcing, sccm
AR(ω)	amplitude ratio for mass flow controller frequency response
F	molar flow rate, sccm or mol/s
G	transfer function
g	scalar transfer function
i	$\sqrt{-1}$
p(s)	characteristic function for the closed-loop system
s	Laplace domain variable, s^{-1}
t	time, s
u_e	ethylene feedback gain
w	half-width of feedback function, sccm
x	gas-phase ethylene mole fraction
α	amplitude of sinusoidal mass flow controller forcing, sccm

τ	reactor mean residence time, s
τ_D	time delay, s
$\Phi(\omega)$	phase shift for mass flow contoller frequency response
ω	bifurcation frequency parameter; sinusoidal forcing frequency, rad/s

subscripts

c	controller
e	ethylene
He	helium
mfc	mass flow controller
p	process
T	total

superscripts

i	inlet
ref	reference condition

REFERENCES

Lyberatos, G. (1985). The effect of delay on the feedback identification of chemical reaction systems. *Chem. Engng. Sci.* **40,** 2160-2162.

Lyberatos, G., B. Kuszta, and J.E. Bailey (1984). Discrimination and identification of dynamic catalytic models via introduction of feedback. *Chem. Engng. Sci.* **39,** 739-750.

McDermott, P.E., H.-C. Chang, and R.G. Rinker (1985). Experimental Investigation of controller-induced bifurcation in a fixed-bed autothermal reactor. *Chem. Engng. Sci.* **40,** 1355-1366.

Prairie, M.R., and J.E. Bailey (1986a). Application of feedback-induced bifurcation for evaluating steady-state and transient heterogeneous catalysis kinetic models. *Chem. Engng. Sci.* **41,** 937-944.

Prairie, M.R, and J.E. Bailey (1986b). Experimental and modeling investigations of steady-state and dynamic characteristics of ethylene hydrogenation on Pt/Al_2O_3. *Chem. Engng. Sci.,* in press.

Smith, C.B. (1983). Dynanic modelling and optimization of lumped chemical processes. Doctoral disertation, University of Houston.

FIGURE CAPTIONS

Fig. 1 Schematic diagram of the experimental apparatus. All gas inlets to the mass flow controllers (MFC1-8) are at 30 psig. Solid lines indicate gas flow paths and dashed lines indicate electronic signals.

Fig. 2 Approximate cross-section of experimental reactor. Dimensions: $d_1 = 0.41$ cm, $d_2 = 0.30$ cm, and $d_3 = 0.75$ cm.

Fig. 3 Block diagram for experimental apparatus.

Fig. 4 Frequency response of the ethylene mass flow controller (MFC 6) for set point forcing at a period of 4.4 s, centered around 10 sccm, with amplitude of 1 sccm in 100 sccm total flow. Solid curve - indicated flow rate. Broken curve - set point forcing function.

Fig. 5 Phase shift for sinusoidal forcing of the ethylene mass flow controller. Solid line : $\Phi(\omega) = - 0.39\omega$.

Fig. 6 Step response of the reactor and IR analyzer for a switch from pure He to 10% C_2H_4 in He. Model calculations (smooth curves) from $\frac{x}{x_\infty} = 1 - e^{-t/\tau}$.

Fig. 7 Experimental (a,b) and model simulation (c,d) data for typical Hopf bifurcation experiments. (a,c) $F_T = 50$ sccm, $\tau_D = 8$ s. (b,d) $F_T = 100$ sccm, $\tau_D = 16$ s. $x^{ref} = 0.10$. Each frame presents data for the last 180 s of 10 min run at the indicated u_e.

Fig. 8 Experimental and calulated bifurcation diagrams for $F_T = 50$ sccm (broken, filled) and $F_T = 100$ sccm (solid, open). The shaded regions indicate those (τ_D , u_e) pairs for which the reference steady state is stable.

Fig. 9 Hopf bifurcation frequencies for $F_T = 50$ sccm (broken, filled) and $F_T = 100$ sccm (solid, open).

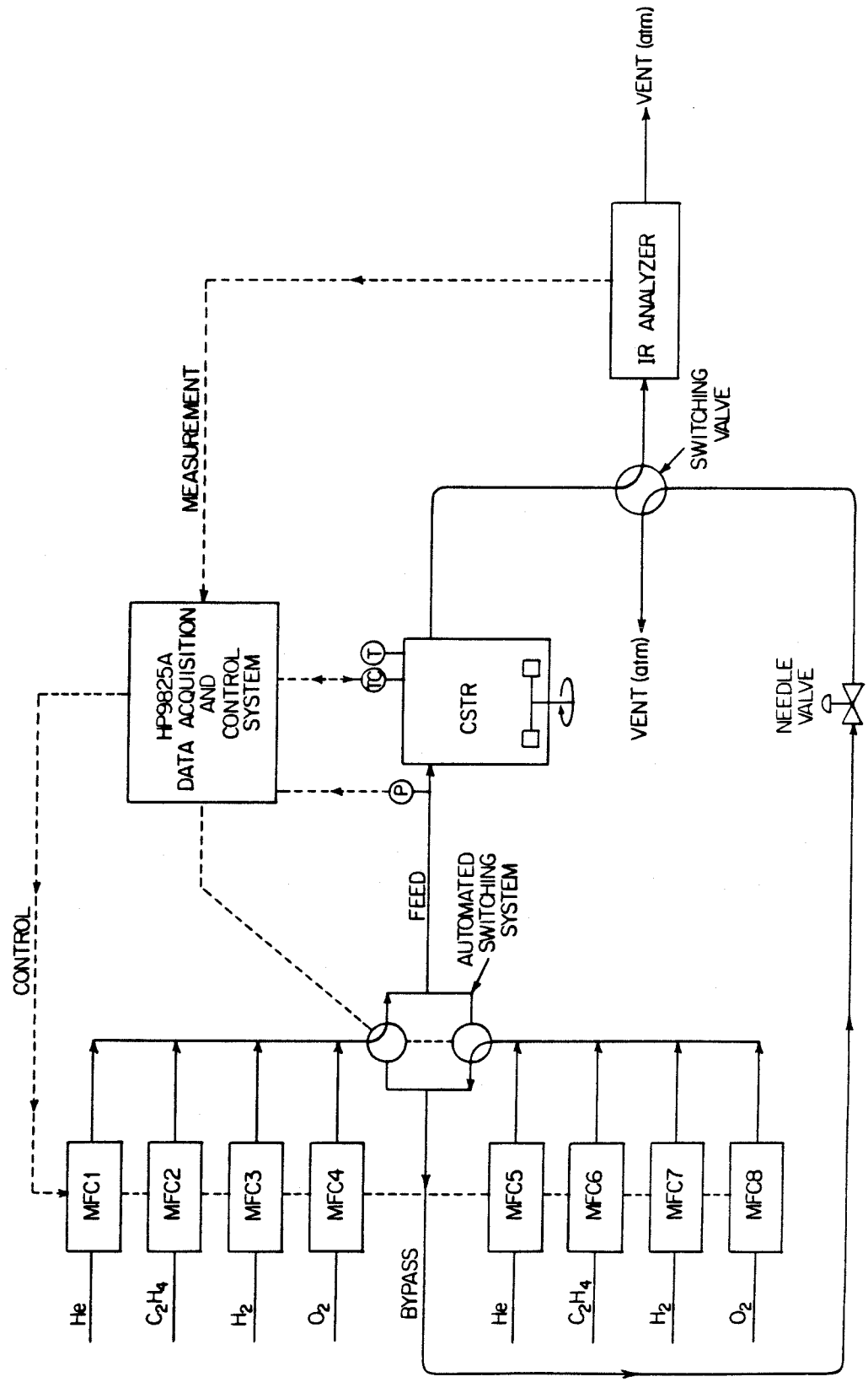
VENT (atm)
IR ANALYZER
SWITCHING VALVE
MEASUREMENT
HP9825A DATA ACQUISITION AND CONTROL SYSTEM
CSTR
VENT (atm)
NEEDLE VALVE
CONTROL
FEED
AUTOMATED SWITCHING SYSTEM
MFC1
MFC2
MFC3
MFC4
MFC5
MFC6
MFC7
MFC8
He
C_2H_4
H_2
O_2
BYPASS
He
C_2H_4
H_2
O_2

Figure 1

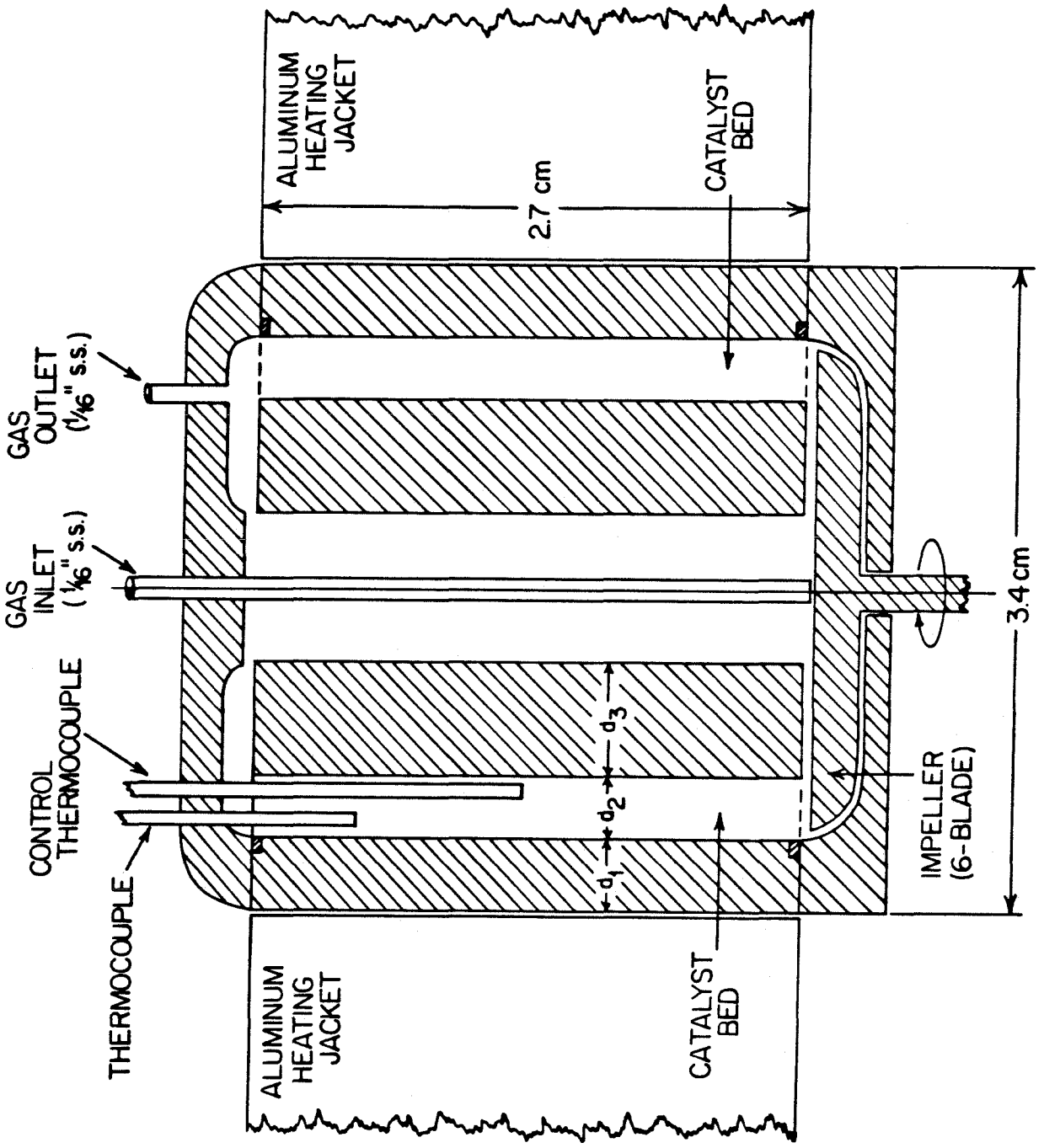
ALUMINUM HEATING JACKET
2.7 cm
CATALYST BED
GAS OUTLET (1/16" s.s.)
GAS INLET (1/16" s.s.)
CONTROL THERMOCOUPLE
THERMOCOUPLE
d_3
d_2
d_1
IMPELLER (6-BLADE)
3.4 cm
ALUMINUM HEATING JACKET
CATALYST BED

Figure 2

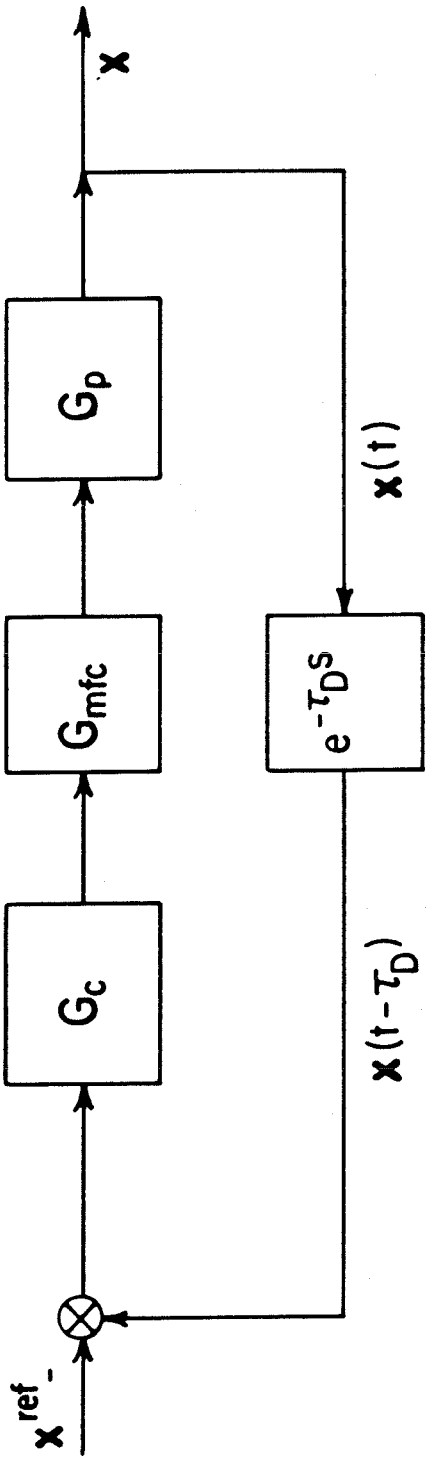

Figure 3

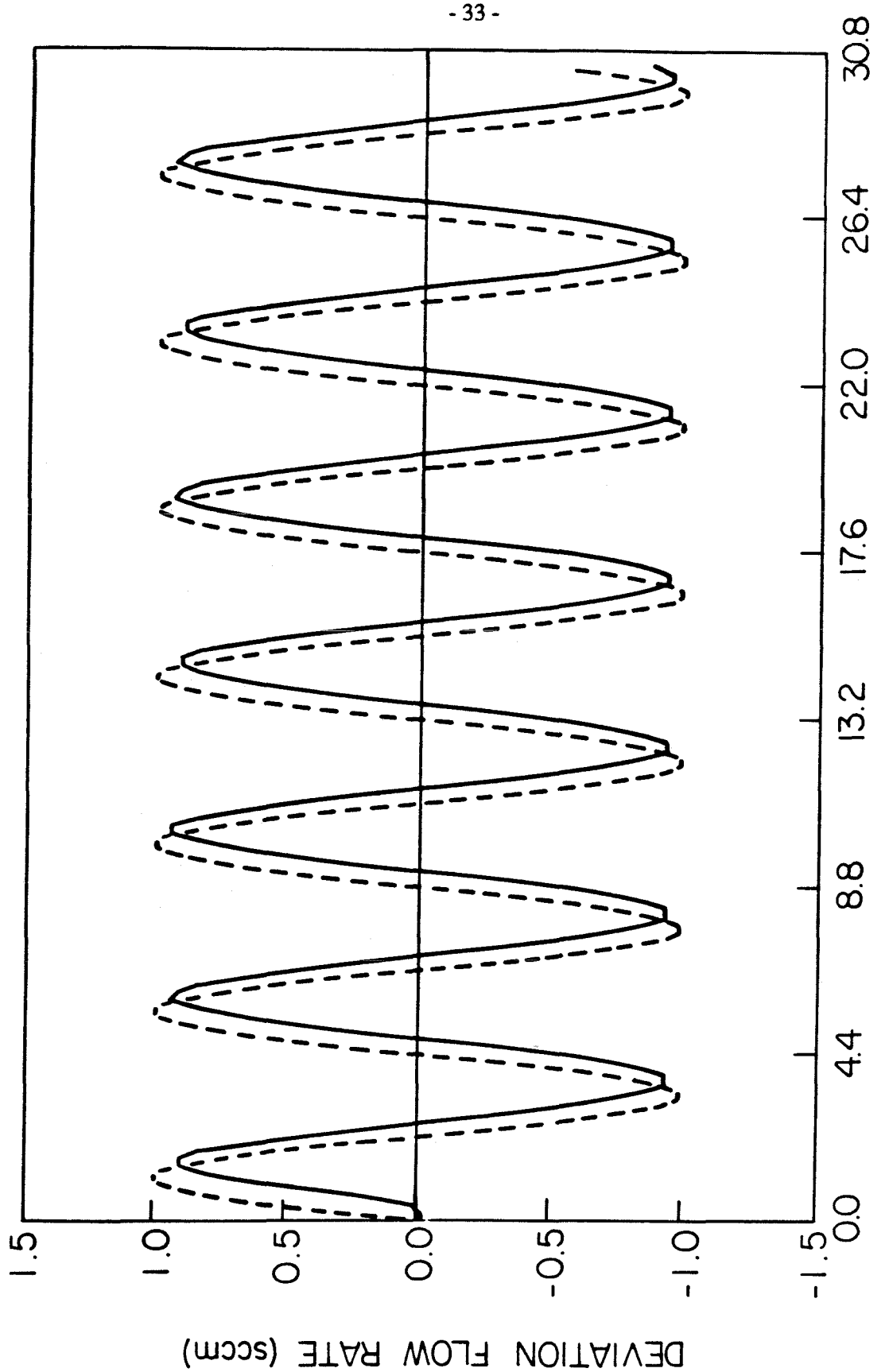
DEVIATION FLOW RATE (sccm)
1.5
1.0
0.5
0.0
-0.5
-1.0
-1.5
0.0
4.4
8.8
13.2
17.6
22.0
26.4
30.8
TIME (sec)

Figure 4

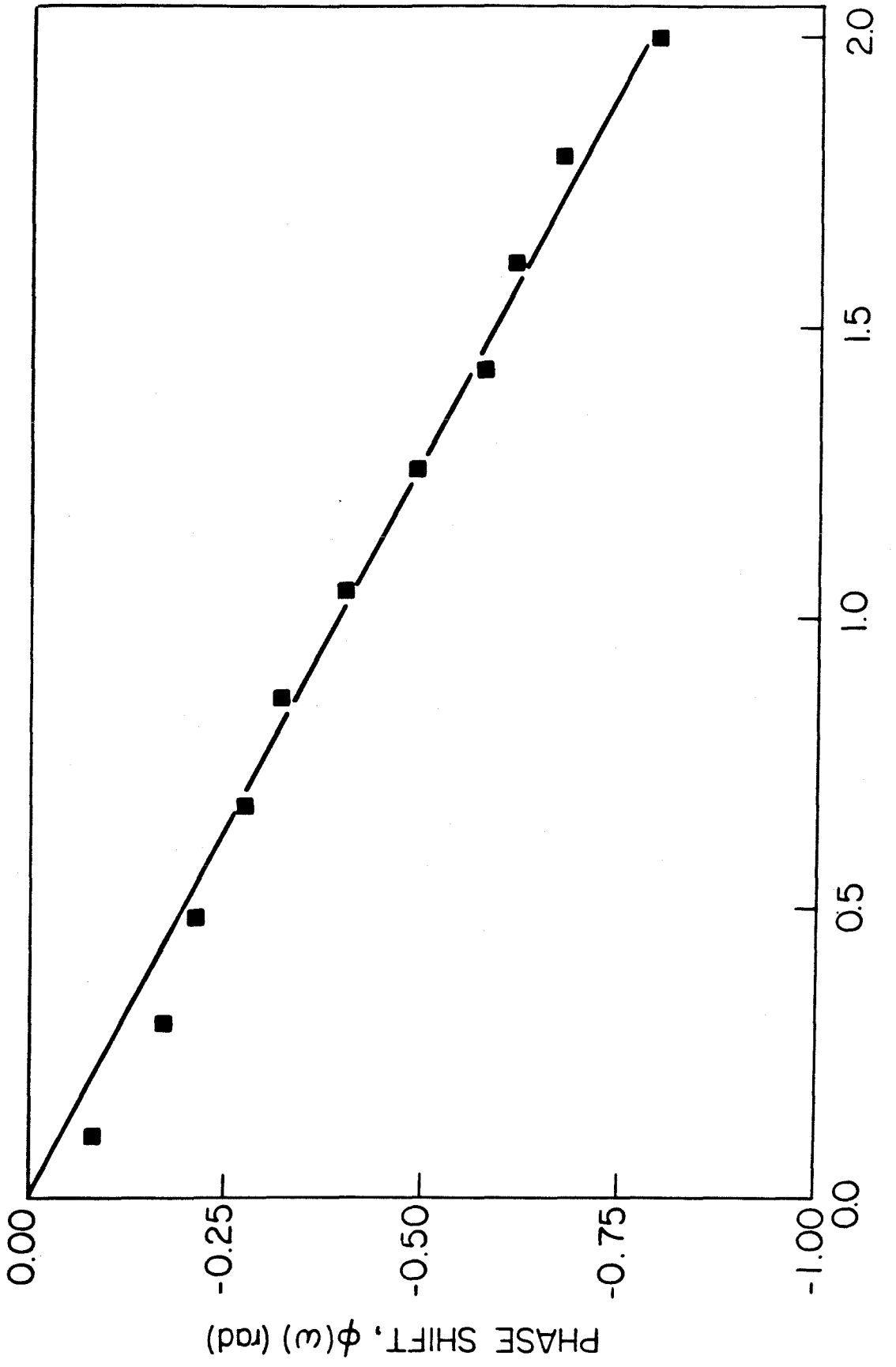
0.00
-0.25
-0.50
-0.75
-1.00
PHASE SHIFT, $\phi(\omega)$ (rad)
0.0
0.5
1.0
1.5
2.0
FREQUENCY, ω (rad/s)

Figure 5

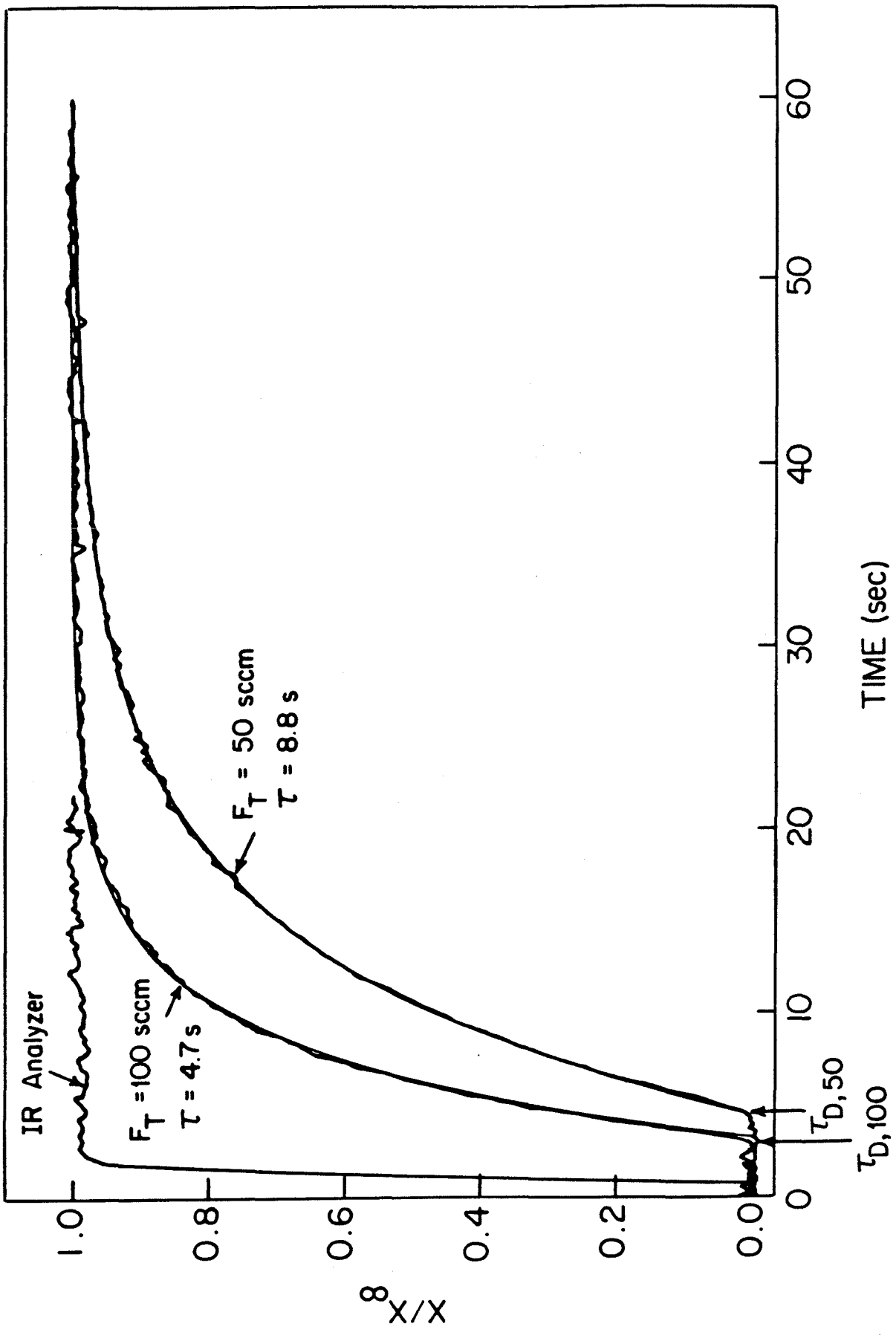
IR Analyzer
F_T = 100 sccm
τ = 4.7 s
F_T = 50 sccm
τ = 8.8 s
$\tau_{D,50}$
$\tau_{D,100}$
X/X_0
TIME (sec)
0.0
0.2
0.4
0.6
0.8
1.0
0
10
20
30
40
50
60

Figure 6

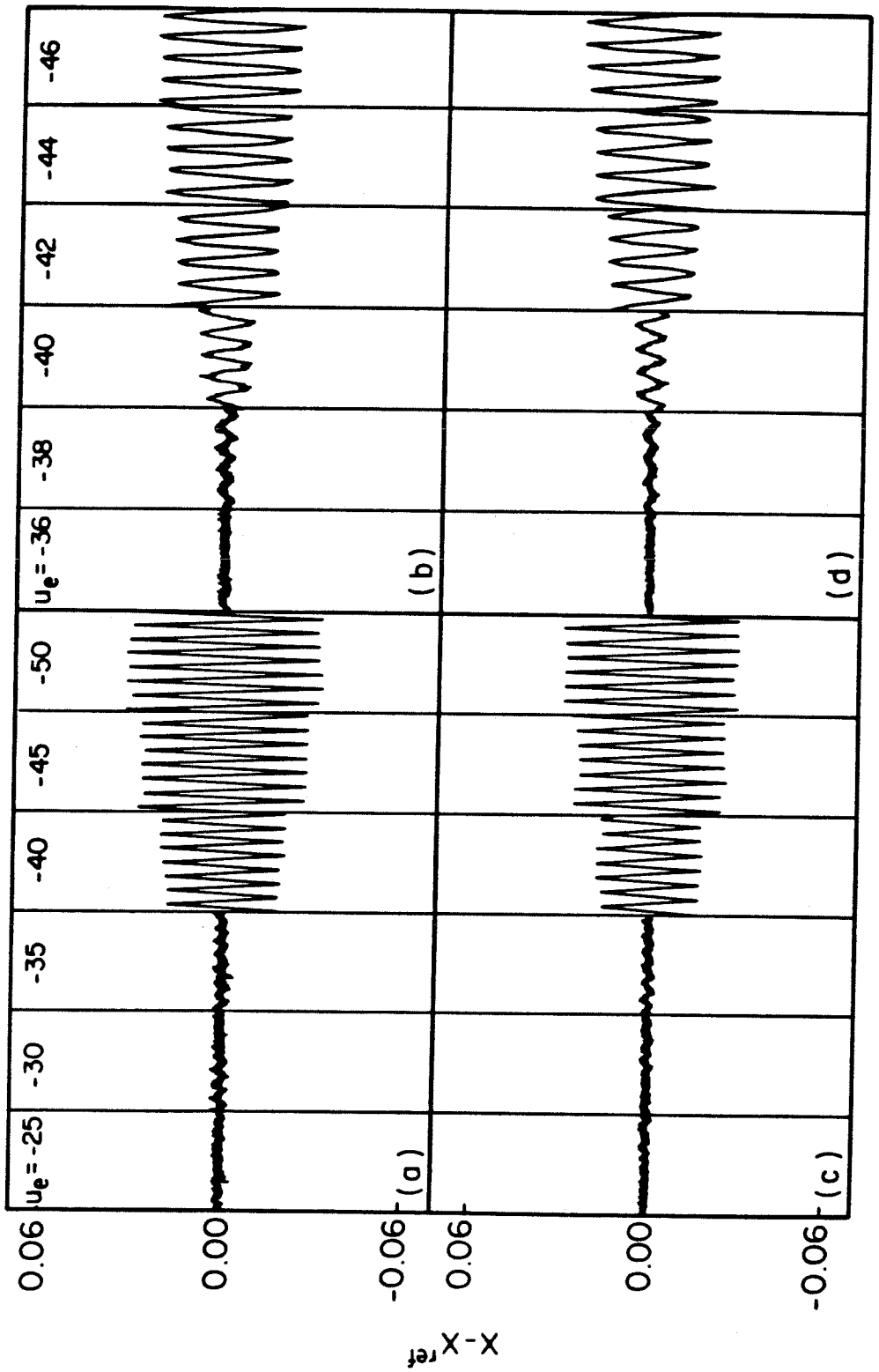
0.06
0.00
-0.06
$X - X_{ref}$
u_e= -25
-30
-35
-40
-45
-50
u_e= -36
-38
-40
-42
-44
-46
(a)
(b)
(c)
(d)
TIME (sec)

Figure 7

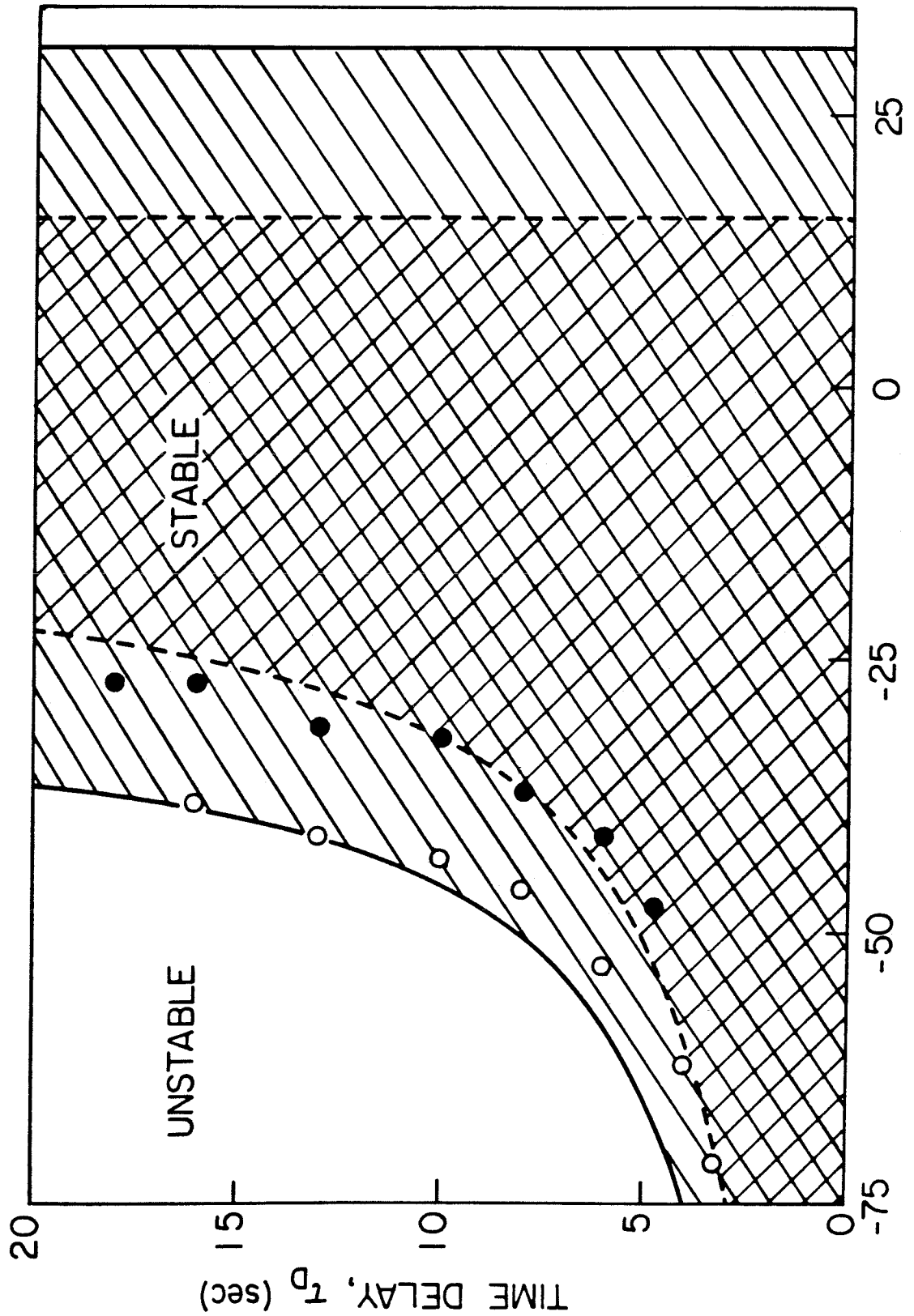
STABLE
UNSTABLE
TIME DELAY, τ_D (sec)
20
15
10
5
0
-75
-50
-25
0
25
ETHYLENE GAIN, U_e

Figure 8

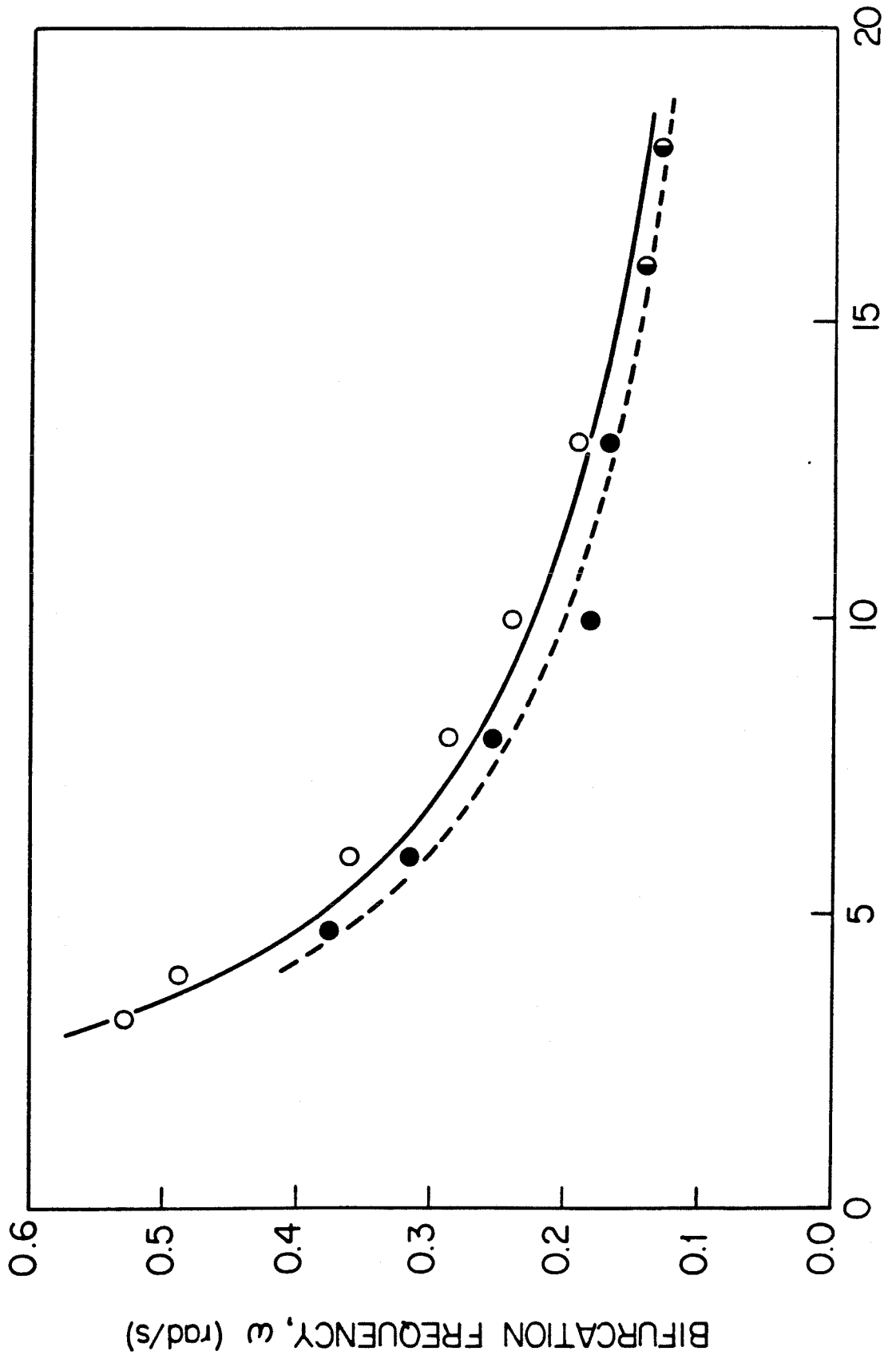
BIFURCATION FREQUENCY, ω (rad/s)
0.0
0.1
0.2
0.3
0.4
0.5
0.6
0
5
10
15
20
TIME DELAY, τ_D (sec)

Figure 9

CHAPTER 3

EXPERIMENTAL AND MODELING INVESTIGATIONS OF STEADY-STATE AND DYNAMIC CHARACTERISTICS OF ETHYLENE HYDROGENATION ON Pt/Al_2O_3

INTRODUCTION

Efforts to formulate kinetic descriptions for catalytic reactions based upon known or hypothesized elementary reaction sequences have progressed significantly since the work of Langmuir, Hinshelwood, Hougen, and Watson. Increasing emphasis on dynamic behavior has revealed deficiencies in classical kinetic treatments because of important contributions of surface species dynamics. As experimental data accumulates on more reaction systems, the equilibrium or quasi-steady state approximations routinely invoked in catalytic kinetics are often found unacceptable for description of transient characteristics of catalytic reactions.

Direct spectroscopic measurements of adsorbed intermediates and catalyst surface states have helped provide insights into fundamental phenomena which determine catalyst dynamic properties. For example, the ultra-high vacuum (UHV) studies of Ertl and coworkers (1982) have demonstrated adlayer phase transitions in connection with oscillatory CO oxidation on Pt single crystals. On the other hand, UHV data are often not directly applicable for describing even the steady-state kinetic properties of supported catalysts. Although some successes in extrapolating UHV data to high pressure have been documented [Herz and Marin, 1980; Oh *et al.*, 1986], metal-support interactions including spillover of metal-adsorbed atoms onto the support are likely important determinants of supported catalyst behavior for many systems. The support may also contribute to overall kinetics by serving as a site for direct adsorption [Williams and Hipps, 1982], and even catalytic reaction of fluid-phase components [Antonucci *et al.*, 1982].

IR spectroscopies have been successfully applied to observe steady-state and transient adsorbate concentrations for several supported catalyst systems [Barshad *et al.*, 1985; Cavanagh and Yates, 1981; Prairie *et al.*, in preparation; Solymosi and Sarkany, 1979; Soma,1979], especially CO oxidation on various supported noble metals [Hecker and Bell, 1983; Kaul and Wolf, 1984,1985; Oh and Hegedus, 1980]. When complex spectra and coverage effects on spectra do

not interfere too greatly with interpretation of the IR data, this approach provides useful insights. However, special reactor-spectrometer configurations, not always possible or convenient for the reaction system of interest, are required to utilize IR surface measurements.

When direct observation of adsorbed intermediates is not feasible, a kinetic description of the supported catalyst reaction must be formulated based on fluid-phase measurements. This is the focus of this work, which has specific and general aims. First, this research seeks to identify and describe the steady-state and transient kinetic properties of ethylene hydrogenation on a supported Pt catalyst. Second, this work explores multiple strategies for conducting and interpreting experiments with the intention of learning as much as possible about the kinetics of the catalytic reaction system. Attributes of each approach are explored using ethylene hydrogenation as an example. In addition, the value of synthesizing information from several different types of experiments will be illustrated for this system. Before turning to these points, it is useful to examine previous research in the domains of general experimental strategy and ethylene hydrogenation kinetics on supported Pt.

Any kinetic description for transient catalysis should, as a special case, apply to steady-state kinetics, Conversely, steady-state kinetic studies and models, such as those presented by Happel and Sellars (1982), delimit the set of candidate elementary reaction steps. Further, steady-state kinetic parameters have one-to-one correspondence with parameters or parameter groups in the transient kinetic description induced by the hypothesized catalytic reaction sequence. Therefore, systematic investigation of steady-state kinetics is an important and necessary component of any strategy for dynamic modeling of catalysis.

Based upon studies using a unique electrochemical cell reactor, Mullins (1982), and Saltsburg (with Mullins, 1982) have proposed the following reaction sequence for ethylene hydrogenation on alumina-supported platinum:

$$H_2 + 2* \underset{k_{-1}}{\overset{k_1}{\rightleftharpoons}} 2H* \quad \text{(I)}$$

$$C_2H_4 + 2* \underset{k_{-2}}{\overset{k_2}{\rightleftharpoons}} C_2H_3* + H* \quad \text{(II)}$$

$$C_2H_4 + H* \underset{K_{eq}}{\rightleftharpoons} C_2H_5* + H* \quad \text{(III)}$$

$$C_2H_5* + H* \underset{k_4}{\rightarrow} C_2H_6 + 2* \quad \text{(IV)}$$

Although reactions of the form of Eqs. (I-IV) commonly appear in hypothesized reaction sequences, they are all probably not elementary reactions since ternary interaction is implied. A more reasonable description of process (I) in terms of elementary steps is an elaborated sequence such as

$$H_2 + * \underset{k_{1b}}{\overset{k_{1a}}{\rightleftharpoons}} H_2* \quad \text{(Ia)}$$

$$H_2* + * \underset{k_{1c}}{\rightarrow} 2H* \quad \text{(Ib)}$$

[Oh, 1985]. Interestingly, if equilibrium is assumed for Step (Ia) above, the rate of formation of adsorbed atomic hydrogen is first order or second order with respect to vacant site fraction as the parameter $\frac{k_{1c}}{k_{1b}}$ ranges from values much larger than unity to values much less than unity, respectively. It is common in reaction engineering to model adsorption rates in terms of simple interger-order dependence on the fraction of vacant sites. Through the simple argument described above it can be shown that the apparent order for any dissociative adsorption process can be first, second, or lie anywhere in between those two asymptotic values. To date, consistency of reaction sequences (I-IV) with transient kinetic data for ethylene hydrogenation on Pt has not been tested. This is a central objective of this study.

In the past, experimental studies of transient catalytic kinetics have fallen into two broad categories: (*i*) stimulus-response measurements and (*ii*) observation of autonomous dynamics, primarily periodic oscillations. Called the "transient response technique" by Kobayashi and

Kobayashi (1974), study of dynamics caused by a step change in reaction conditions has been used to infer qualitative features and/or kinetic parameters of the catalytic reaction network in research by Bennett (1976), Kobayashi (1982), Dettmer and Renken (1983), and many others. For small perturbations which result in approximately linear dynamics following the perturbation, kinetic information may be obtained by applying the relaxation methods introduced by Eigen and de Maeyer (1963). Larger step changes generating nonlinear responses are typically analyzed quantitatively using numerical simulation of a hypothesized catalytic reaction sequence. Use of periodic inputs to probe catalytic mechanisms and kinetic parameters is reviewed by Swartz and Madix (1974) for small-amplitude, linear behavior. Cycling the feed concentration to a catalytic reactor can be used as a powerful test of the dynamic model for the system as well as a method for increasing time-average reaction rate or product selectivity. Bailey and Horn (1970) proposed study of nonlinear effects resulting from large amplitude cycling in order to discriminate among alternative catalytic mechanisms. Several experimental investigations have applied forced-cycling to study catalytic dynamics [Barshad *et al.*, 1985; Bilimoria and Bailey, 1978; Feimer *et al.*, 1982; Graham and Lynch, 1984]. In one study, Cutlip *et al.* (1983) used forced concentration cycling as a method for discriminating among four rival models for CO oxidation on a supported platinum catalyst.

Observations of autonomous oscillations and more complicated transient phenomena in isothermal catalytic reactions have been applied to characterize elementary steps and surface interactions. For example, Pikios and Luss (1977), and Slin'ko and Slin'ko (1978) used activation energy dependence on CO coverage to explain autonomous oscillations for CO oxidation on platinum. In another CO oxidation study, Ertl, Norton and Rustig (1982) attributed oscillations on UHV single crystals to surface phase transitions of the CO adlayer. Lynch *et al.* (1986) presented a mathematical model that correctly predicts the shapes and frequencies of CO oscilla-

tions over a wide range of operating parameters for CO oxidation on supported Pt. The model mathematically accounts for phase transitions of the CO adlayer and their effect on the oxygen sticking coefficient.

The underlying causes for oscillatory behavior must, in mathematical terms, give rise to nonlinear features which can be analyzed using bifurcation theory and computer simulation. In a sophisticated iterative procedure, Aluko (1983) used published bifurcation data for CO oxidation on a Pt wire to estimate 18 parameters in a mathematical model describing the reaction. The data were in the form of stability boundaries in gas temperature versus $\frac{P_{CO}}{P_{O_2}}$ space that mark transitions from stable steady-state operation to regimes of autonomous oscillations as seen from measurements of the catalyst surface temperature. Although potentially quite powerful for dynamic modeling of catalytic systems, the method of Aluko and other methods using bifurcation data require that the system bifurcate naturally. Unfortunately, this requirement is not satisfied for most catalytic reaction systems.

The feedback-induced bifurcation method recently proposed for discrimination and identification of catalytic reaction models [Kuszta and Bailey, 1982; Lyberatos *et al.* 1984,1985] is in some respects a synthesis of stimulus-response and autonomous dynamics approaches. Nonlinear systems theory indicates that local dynamic behavior is intrinsically nonlinear at bifurcation, suggesting special significance of studies at or near bifurcation for sensitive model discrimination. Since most catalytic reaction systems of interest do not exhibit bifurcations to multiple steady states or oscillations, these features must be induced by adding an external feedback loop to the experimental system. In a computational example, Lyberatos *et al.* (1984) have shown that the loci of different bifurcation conditions in the space of feedback control parameters are distinctly different for two alternative models for NO_2 decomposition on Ni which are difficult to distinguish based on steady-state and step-response data.

In an experimental example, McDermott *et al.* (1985) used a proportional controller to destabilize a fixed-bed, autothermal reactor supporting the water-gas shift reaction. These workers used open-loop steady-state data, a single Hopf bifurcation point (feedback gain), a turning point, and time trajectories of stable periodic branches to estimate heat transfer properties of the nonisothermal experimental system. The work emphasizes the rich nonlinear content of bifurcation data and produced a very accurate model for the experimental system.

Potentially, each of these classes of experiments for probing catalyst dynamics provides different kinds of information on the catalytic reaction system. In this study, step-response measurements, forced-cycling studies, and feedback-induced bifurcation experiments are employed in parallel to study the steady-state and transient characteristics of ethylene hydrogenation on supported Pt. In addition to providing new information on this specific reaction, this research offers insights on the advantages and limitations of these different approaches for investigation of catalytic kinetics.

MATERIALS AND METHODS

Many details of the experimental apparatus are presented elsewhere [Smith, 1983] so only a brief description is presented here. Helium (99.9999%), hydrogen (99.9995%), and ethylene (C.P. grade) are the reactants supplied to two parallel banks of mass flow controllers which regulate flow rates up to 200 sccm, 20 sccm, and 20 sccm, respectively. Two low dead-volume solenoid valves direct flow to the reactor and simultaneously through a bypass to a vent line that joins the reactor effluent before disposal in a fume hood. A needle valve regulates downstream pressure on the vent line to duplicate reactor pressure drop and thus avoid pressure surges during bank-to-bank switching.

Switching is achieved either manually or automatically with an HP9825B microcomputer

based data acquisition and control (DAC) system. Mass flow controller set-points can be set manually or automatically with the DAC system. Closed-loop feedback control of the reactor feed composition and molar flow rate is implemented by manipulating mass flow controller set-points quasi-continuously with the DAC system which uses control algorithms based on effluent composition measurements.

Ethylene concentration in the reactor effluent, or bypass line, is continuously monitored with a Wilkes Miran I variable filter infrared analyzer operating at 10.4 μm and equipped with a 0.35 cm^3 flow-through cell. The IR analyzer is interfaced with a strip-chart recorder and the DAC system for continuous analog and digital records of ethylene in the reactor effluent or bypass lines. An on-line gas chromatograph is used to check on the number of species in the system and verify the absence of undesirable side reactions.

The reactor is an approximately 10 cm^3 stainless steel, annular, fixed-bed, internal recycle reactor that is stirred from below at up to 3000 rpm with a magnetically driven impeller. One-sixteenth inch stainless steel lines provide the reactor with feed and effluent removal . Two sheathed, T-type thermocouples are used to monitor the catalyst bed temperature. The reactor temperature can be controlled up to 400 °C with a PI controller which provides power to eight heating cartridges located within a large aluminum heat sink that surrounds the reactor vessel. All hardware in contact with the reactor gas is stainless steel except for two aluminum gaskets at either end of the reactor volume. All tubing in the reactor system is $\frac{1}{16}$ inch stainless steel to minimize transport lag. A detailed description of the reactor can be found elsewhere [Smith, 1983; Prairie *et al.*, 1987].

The catalyst used for these experiments was 0.05% Pt on one-eighth inch cylindrical alumina pellets. It was supplied by Engelhard (Lot # 118-7-00-196). Each pellet has a very thin external shell (approximately 70 μm thick) where metal is dispersed, surrounding an alumina

core. Engelhard reports the support to be a mixture of δ- and γ-alumina. Hydrogen chemisorption experiments corrected for support uptake indicate 17% metal dispersion. Forty half-cylinders (0.93 g) of catalyst were mixed with 2 mm dia. glass beads and the mixture was then loaded into the reactor.

Residence time distribution experiments similar to those described elsewhere for the reactor without reaction [Prairie *et al.*, 1987] were performed in order to obtain estimates for the reactor time constant and system transport lag. The experiments indicate that the reactor can be modeled as an ideal CSTR with a residence time of 3.94 s at 80 °C and 100 sccm total flow with a 3.21 s transport lag between the switching valves and the IR analyzer.

The operating temperature of 80 °C was chosen for these experiments since it results in convenient steady-state conversion levels (approximately 30% of the limiting reactant) for the feed composition range allowed by the mass flow controllers. The fresh catalyst was pretreated at 400 °C for one hour in a flowing stream of 10% O_2 in He followed by reduction at 400 °C in 10% H_2 in He. The reactor was then cooled to 80 °C in flowing He when flow of a reactive C_2H_4/H_2 mixture was introduced into the system. After approximately 24 hours, the catalyst reached a steady, reproducible level of activity that did not change appreciably over the entire course of experiments. The reactor was maintained at 80 °C in flowing He during periods of inactivity and repretreatment was unnecessary between experiments. Also, no ethylene conversion occurs in the reactor system when the catalyst is not present. Thus, all steady-state and dynamic features that are described later can be attributed to the Pt/Al_2O_3 catalyst.

This paper describes results from four types of experiments, namely, steady-state kinetic, step-response, feedback-induced bifurcation, and cycled-feedstream. The remainder of this section describes the experimental methods for each type of experiment.

Steady-state rate measurements were obtained for 80 °C by manipulating the ethylene and hydrogen feed rates between 0 and 20 sccm while maintaining 100 sccm total feed to the reactor. In this way, effluent ethylene concentration data were obtained for 70 feeds ranging over a square area in feed composition space having vertices (0,0), (0,20%), (20%,0), and (20%,20%) (coordinates designate ethylene and hydrogen mole percents, respectively). The desired feed was admitted to the reactor, and the ethylene concentration in the effluent was monitored for each of the 70 feed compositions. Care was taken to assure that the reactor was at steady state before each point was collected.

Observed reaction rates were calculated with the total inlet feed rate, F_T^i, the feed compositions, the reaction stoichiometry, and the steady-state effluent ethylene concentrations, $x_{1,j}$, according to

$$r_{o,j} = \varepsilon_j = \frac{F_{e,j}^i - F_T^i x_{1,j}}{1 - x_{1,j}} \tag{1}$$

where $r_{o,j}$ is the observed reaction rate in mol/s, ε_j is the extent of reaction in mol/s, and $F_{e,j}^i$ is the ethylene feed rate in mol/s. The index j denotes the j^{th} experimental observation. Units for the molar flow rates will frequently be given as sccm throughout this manuscript. Although sccm is rigorously a measure of volumetric flow rate, the direct conversion to molar flow rates is possible with the factor $\frac{\text{sccm}}{134.4 \times 10^4} = \frac{\text{mol}}{\text{s}}$. Both flow units will be used interchangeably throughout this text.

Step-response and forced-cycling experiments were performed by first manually setting the mass flow controller set-points for the two feed streams and then implementing the desired switching schedule with the computer DAC system. Step-response experiments simply require a switch from one feedstream to the other while simultaneously monitoring ethylene in the reactor effluent. Cycled-feedstream experiments involve switching between the two streams at a

predetermined forcing period. Forcing periods ranging from 30 s to 10,000 s and only symmetric input square waves were used.

Feedback experiments were performed by using the DAC system to manipulate ethylene and hydrogen feed rates as functions of the effluent ethylene IR signal. The control program operates at 4 Hz which is approximately 16 times faster than the time scale of the CSTR. It is shown elsewhere (through computer simulation) that this data acquisition rate is sufficiently fast to allow the closed-loop system to be modeled as a continuous system, and that aliasing is not a problem [Prairie *et al.*, 1987].

MODELING EQUATIONS

The differential equations that describe the isothermal reactor behavior can be derived from mechanism (I-IV) assuming mass action kinetics, perfect CSTR behavior and the absence of limiting transport effects:

$$n\frac{dx_1}{dt} = F_e^i - F_T^o x_1 - k_2 x_1 \theta_v^2 + k_{-2}\theta_1\theta_2 - k_4\theta_1\theta_3 \tag{2}$$

$$n\frac{dx_2}{dt} = F_h^i - F_T^o x_2 - k_1 x_2 \theta_v^m + k_{-1}\theta_I^2 \tag{3}$$

$$N_T\frac{d\theta_1}{dt} = 2k_1 x_2 \theta_v^m - 2k_{-1}\theta_I^2 + k_2 x_1 \theta_v^2 - k_{-2}\theta_1\theta_2 - 2k_4\theta_1\theta_3 \tag{4}$$

$$N_T\frac{d\theta_2}{dt} = k_2 x_1 \theta_v^2 - k_{-2}\theta_1\theta_2 \tag{5}$$

with

$$\theta_3 = K_{eq} x_1 \theta_1. \tag{6}$$

Equation (6) results from assuming process (III) at dynamic equilibrium; the validity of this assumption is addressed later. The state variables x_1 and x_2 denote ethylene and hydrogen gas-

phase mole fractions in the reactor and in the reactor effluent. Fractional coverages, θ_1, θ_2, and θ_3, represent the fraction of active surface sites covered by the three adsorbates, H*, C_2H_3*, and C_2H_5*, respectively. The fraction of sites that are vacant, θ_v, is calculated with the site balance $\theta_v + \theta_1 + \theta_2 + \theta_3 = 1$. In Eqs. (2) and (3), F_T^o represents the total molar effluent rate in mol/s. In all cases, the rate coefficients, k_i already contain information about the total amount of catalyst in the reactor. They can be converted to intensive quantities by dividing out the mass of catalyst (0.93 g).

The order, m, in θ_v for hydrogen adsorption is 1 or 2 depending on whether the parameter $\frac{k_{1c}}{k_{1b}}$ is very large or very small with respect to unity. A goal of this research is to estimate values for the rate coefficients, k_i and K_{eq}, and to determine the appropriate value for m.

Inherent in the applicability of Eqs. (2) and (3) is the assumption that the total molar reactor capacity, n, a function of temperature and pressure, remains constant. This assumption is valid for the fixed bed, isothermal CSTR if it remains essentially isobaric, regardless of extent of reaction. Isobaric behavior was verified with a pressure gauge located slightly upstream from the reactor. Hence, the total outlet flow rate can be calculated from the overall material balance on the CSTR:

$$\frac{dn}{dt} = 0 = F_T^i - F_T^o - k_1 x_2 \theta_v^m + k_{-1}\theta_I^2 - k_2 x_1 \theta_v^2 + k_{-2}\theta_1\theta_2 \qquad (7)$$

and the result inserted into Eqs. (2) and (3).

STEADY-STATE KINETIC EXPERIMENTS AND MODELING

Steady-state rate data were recorded for 70 different feed compositions, 80 °C, ambient pressure, and 100 sccm total flow. The observed rate ranged from 0.49 μmol/s to 5.10 μmol/s and ethylene conversion from 3.4% to 96% with a mean of 36% and standard deviation of 32%.

Questions arise regarding the importance of mass transport with respect to the observed reaction rates. According to a criterion by Weisz and Prater (Aris,1975), the observable modulus, $\phi_o = \left[l^2 \frac{r_o}{D_e C_f} \right]^{\frac{1}{2}}$ can be used to estimate the importance of internal mass transport resistances on the overall reaction. Here r_o is the observed reaction rate on a per volume of catalyst basis. Also, l is the thickness of the dispersed Pt shell, D_e is the effective diffusivity for ethylene in He, and C_f is the appropriate bulk ethylene concentration. When ϕ_o is much less than 1, it can safely be assumed that internal transport resistances are negligible when the reaction kinetics are first-order. This criterion has been generalized to include typical Hougen-Watson kinetics, and for many catalytic reactions appears in a single figure in the interdisciplinary paper by Weisz (1973). There it is shown that the effectiveness factor lies between 0.8 and unity for observed Thiele moduli, ϕ_o, less than approximately 0.6. Although implicit, the reaction mechanism given in steps (I-IV) exhibits kinetics that are similar in form to Hougen-Watson kinetics with first-order inhibition by one of the reactants, and shows first- to negative first- order dependence on ethylene concentration.

The shells of the 0.05% Pt/Al_2O_3 pellets where the Pt is dispersed are approximately 70 μm thick, hence l = 70 μm. Mercury porosimitry experiments with the catalyst suggest that it contains a bidisperse pore structure which is typical of alumina catalysts [Smith, 1981]. The macropores have a mean radius of 2176 A and contribute ε_M = 0.193 to the overall porosity. Micropores are usually assumed to be those pores with radii less than 100 A; the micropores for the

Pt/Al_2O_3 catalyst have a mean radius of 43 A and contribute $\varepsilon_\mu = 0.244$ to the catalyst porosity. These porosimitry data were used in the random-pore model for bidisperse catalysts [Smith, 1981] to calculate a value of D_e equal to 0.015 cm^2/s for ethylene diffusing through helium at 80 °C and atmospheric pressure. The appropriate value of r_o to use in the observable modulus is the largest observable rate, which in this case is 77 $\mu mol/cm^3 \cdot s$ (this resulted for 10% ethylene and 20% hydrogen in the feed). With these values, an observable modulus based on ethylene equal to 0.65 was calculated. In a similar manner it was shown that the observable modulus based on hydrogen is 0.18 at the maximum rate. These values indicate that the observed reaction rates are probably not affected by ethylene diffusion and certainly are not influenced by hydrogen diffusion. Since these calculations were performed for the maximum observed rates, most of the steady-state data provide a true reflection of intrinsic kinetics.

External mass transfer rate limitation was eliminated by employing an agitation rate which is well into the region where impeller velocity no longer affects the overall reaction rate.

The experimental steady-state kinetic rate data were used to estimate coefficients in the nonlinear model. The steady-state intrinsic rate surface is described in terms of the two gas-phase state variables, x_1 and x_2, with the implicit system

$$r(x_1,x_2) = k_4 K_{eq} x_1 \theta_1^2 \tag{8}$$

$$k_1 x_2 \theta_v^m - k_{-1} \theta_1^2 - k_4 \theta_1 \theta_3 = 0 \tag{9}$$

$$K x_1 \theta_v^2 - \theta_1 \theta_2 = 0 \tag{10}$$

where K is the equilibrium coefficient that naturally results from setting the right hand side of Eq. (5) equal to zero; $K = \frac{k_2}{k_{-2}}$. The intrinsic rate, $r(x_1,x_2)$, is an implicit function of $x_1$and x_2 which can be calculated by inserting the solution of Eqs. (6),(9), and (10) into Eq. (8). In general, the intrinsic rate should be written $r(x_1,x_2,\theta_1,\theta_2,\theta_3)$. However, at steady state, θ_i values can be

uniquely evaluated in terms of x_1 and x_2. The notation $r(x_1,x_2)$ will henceforth be used to denote the intrinsic rate surface at steady-state conditions.

A nonlinear Marquardt-Levenberg routine (IMSL program ZXSSQ) was used with the experimental data to find the parameters k_1, k_{-1}, K, K_{eq}, and k_4 for the two cases m = 1, and m = 2. The objective function used for the minimization was the sum of squares of the differences between the experimental rate measurements, $r_{o,j}$, and the calculated rates, $r(x_{1,j},x_{2,j})$.

The hydrogen desorption parameter, k_{-1}, was determined to be negligible for both values of m. Calculations including the full steady-state model with process (III) not at equilibrium yielded different values for k_3 and k_{-3} each time different initial estimates of the parameters were supplied to the computer program. However, convergence of the regression routine on a valid solution always resulted in the same number for the ratio of k_3 and k_{-3}; a value which provided the same quality of fit amongst all the runs. Accordingly, process (III) was assumed to be in dynamic equilibrium.

Global minima in the sum of squares surfaces were obtained for m = 1 and m = 2. Results are presented in Table 1. Representative rate data and model results are displayed in Fig. 1. Figure 1 and the SSQ and r^2 results in Table 1 show that both models describe the steady-state rate data equally well. The disagreement between the data in Fig. 1 and the models, and the scatter in the data, particularly for larger values of the ethylene feed fraction, is probably due to the reactor not being completely at steady state at the time of data acquisition. As will be shown later, there exists an extremely slow component to system dynamics that makes steady-state experiments difficult. This problem was worse for larger ethylene concentrations. Further investigation is needed in order to choose the superior model. Step-response experiments proved to be useful for this discrimination.

STEP-RESPONSE EXPERIMENTS AND DYNAMIC MODELING

Dimensionless dynamic equations based on the reaction mechanism with step (III) at dynamic equilibrium and irreversible hydrogen adsorption are given below.

$$\tau\frac{dx_1}{dt} = x_1^i - x_1 + \hat{k}_1 x_1 x_2 \theta_v^m - \hat{k}_2(1-x_1)x_1\theta_v^2 + \frac{\hat{k}_2}{K}(1-x_1)\theta_1\theta_2 - \hat{k}_4 K_{eq} x_1 \theta_1^2 = x_1^i + f_1 \tag{11}$$

$$\tau\frac{dx_2}{dt} = x_2^i - x_2 - \hat{k}_1(1-x_2)x_2\theta_v^m + \hat{k}_2 x_1 x_2 \theta_v^2 - \frac{\hat{k}_2}{K} x_2\theta_1\theta_2 = x_2^i + f_2 \tag{12}$$

$$\tau_{s1}\frac{d\theta_1}{dt} = 2\hat{k}_1 x_2 \theta_v^m + \hat{k}_2 x_1 \theta_v^2 - \frac{\hat{k}_2}{K}\theta_1\theta_2 - 2\hat{k}_4 K_{eq} x_1 \theta_1^2 = f_3 \tag{13}$$

$$\tau_{s2}\frac{d\theta_2}{dt} = x_1\theta_v^2 - \frac{\theta_1\theta_2}{K} = f_4 \tag{14}$$

with dimensionless rate coefficients and the time constants defined by

$$\tau = \frac{n}{F_T^i} \qquad \tau_{s1} = \frac{N_T}{F_T^i} \qquad \tau_{s2} = \frac{N_T}{k_2}$$

$$K = \frac{k_2}{k_{-2}} \qquad \hat{k}_j = \frac{k_j}{F_T^i};\ j=1,2,4 \qquad \hat{k}_2 = \frac{\tau_{s1}}{\tau_{s2}}.$$

This dynamic model contains three undetermined parameters, τ_{s1}, τ_{s2}, and m. Theoretically, τ_{s1} can be estimated by applying chemisorption experiments to the catalyst. The surface time constant for the site-poisoning step (II), τ_{s2}, is completely unknown. The objective of the step-response experiments is to estimate τ_{s1}, τ_{s2}, and to determine the best value for m while also testing the validity of the proposed kinetic model.

Two step experiments were performed using He as the carrier (80 °C, 100 sccm total feed). Step experiment A produced the ethylene response for a switch from 18% H_2 and no C_2H_4 to a feed containing 18% H_2 and 18% C_2H_4. Step experiment B involved a switch from 18% H_2 and no C_2H_4 to 20% H_2 and 14% C_2H_4. These two experiments differ in that for case A, the

second feedstream contains a stoichiometric mixture of reactants whereas the second feedstream in experiment B contains a net-reducing mixture of reactants. For each experiment, the catalyst was given sufficient time prior to the switch for equilibration with the H_2 containing feed stream.

Figure 2 demonstrates that excellent agreement can be achieved between the model and the data for both step experiments A and B if m = 1 and the surface time constants are chosen such that τ_{s1} = 5000 s and τ_{s2} = 5000 s. No combination of τ_{s1} and τ_{s2} allows reasonable agreement between the model and the data for the case where m = 2. Second order hydrogen adsorption produces S-shaped profiles that in no way resemble the experimental step-response trajectories. It is concluded that the hydrogen adsorption process is effectively first order in the fraction of vacant sites.

It is possible that intraparticle diffusion contributed to the observed step-response profiles. An estimate of the time scale for diffusion is $l^2/D_e = 0.007^2/0.015$ s = 0.003 s. Hence the very slow step dynamics are not affected by diffusion, although the large apparent reaction rates occurring initially could be influenced by quasi-steady-state diffusion effects. A similar argument holds for cycled feedstream profiles that are presented later.

Computer simulations show little sensitivity to τ_{s2}, provided it is larger than approximately 1000 s. In other words, the overall reactor response as viewed through ethylene effluent concentration measurements is not sensitive to the dynamics of the surface poisoning step (II), although that step is necessary to adequately describe the steady-state kinetic data presented earlier. The value of 5000 s for τ_{s2} was chosen for the purpose of calculating the profiles in Fig. 2.

FEEDBACK-INDUCED HOPF BIFURCATION EXPERIMENTS AND MODELING

It has been shown in this paper that the kinetic model of Saltsburg and Mullins (1982), with the appropriate parameters, time constants, and m = 1, is excellent for describing steady-state and step-response behavior of the experimental CSTR. Feedback-induced bifurcation experiments were designed and implemented to further test the model, its validity and robustness.

Feedback to both the ethylene and hydrogen mass flow controllers based on effluent ethylene concentration measurements was used to induce steady-state and Hopf bifurcations in the CSTR. The arctangent was chosen for the feedback function because it is self-saturating, has a continuous first derivative and is linearly equivalent to proportional control. During closed-loop operation, the set-points to the ethylene and hydrogen mass flow controllers are calculated with the algorithms

$$F_{e,h}^{i} = F_{e,h}^{ref} + \frac{2w}{\pi}\mathrm{Tan}^{-1}\left[u_{e,h}(x_1 - x_{1,ref})\right] \tag{16}$$

where e and h denote the ethylene or hydrogen mass flow controller, respectively. The ref subscript and superscript denotes a reference condition that is a stable stationary point of the reactor system given the feeds F_e^{ref} and F_h^{ref} in a fixed total feed rate. Ideally, $x_{1,ref}$ is a true stationary point for the model and the reactor; realistically this is never the case. Discrepancies between the experimental, user-chosen value for $x_{1,ref}$ and the real steady state give rise to very interesting imperfect steady-state bifurcation behavior [Prairie and Bailey, 1986]. With respect to Eq. (16), w is the half-width of the feedback function in sccm (equivalently in mol/s) and u_e and u_h are the feedback gains which will be manipulated to produce the desired bifurcations. Total molar feed rate, F_T^i, is maintained approximately constant during closed-loop operation by manipulating the helium feed flow rate according to

$$F_{He}^{i} = F_{T}^{i} - F_{e}^{i} - F_{h}^{i}. \tag{17}$$

Sinusoidal forcing of the mass flow controller set points verified that the total feed rate does not stray significantly from the prescribed value F_T^i for the frequency range that is encountered for the Hopf bifurcation experiments.

The nonlinear system of ODE's that describes the catalytic CSTR must be linearized about the reference steady state for application of stability theory. In general, deviation variables can be defined as $\hat{\mathbf{x}} = \mathbf{x} - \mathbf{x}_{ref}$, where $\mathbf{x}$ is an n-dimensional vector of states of the system. For the experimental system, n = 4, and $\mathbf{x} = (x_1, x_2, \theta_1, \theta_2)^T$. In vector notation, the linearized system is

$$\frac{d\hat{\mathbf{x}}}{dt} = \mathbf{A}\hat{\mathbf{x}} + \frac{1}{\tau}\mathbf{B}\mathbf{u}$$

$$\mathbf{y} = \mathbf{C}\hat{\mathbf{x}} \tag{18}$$

where

$$a_{ij} = \frac{1}{\tau_i}\frac{\partial f_i}{\partial x_j}\bigg|_{\hat{\mathbf{x}}=\mathbf{0}} \tag{19}$$

and $\tau_1 = \tau_2 = \tau$, $\tau_3 = \tau_{s1}$, and $\tau_4 = \tau_{s2}$. In Eq. (18), $\mathbf{A} = [a_{ij}]$ where a_{ij} are the coefficients for the linearized forms of the functions f_i which are defined in Eqs. (11-14). The vector $\mathbf{y}$ contains the measured variables. The vector $\mathbf{u}$ contains the manipulated variables which are the dimensionless ethylene and hydrogen feed rates, respectively ($\mathbf{u} = (\hat{x}_1^i, \hat{x}_2^i, 0, 0)^T$).

During closed-loop operation, $\mathbf{u}$ is manipulated according to the feedback algorithm given in Eq. (16) which contains the two feedback gain parameters u_e and u_h. With linear stability theory, these two gains can be used to describe a plane that contains stability and instability regions for the reference steady state of the closed-loop system. Curves that separate regions of stability from regions of instability are bifurcation curves and correspond to various types of

well-defined eigenvalue configurations [Lyberatos, Kuszta and Bailey, 1985b]. It should be noted that within the context of this linearized analysis, the arctangent feedback algorithms are equivalent to proportional controllers.

Two types of eigenvalue situations are sufficient to characterize the stability diagram in the feedback gain plane for the experimental reactor system. First, the reference steady state loses stability when a simple leading eigenvalue of the linearized, closed-loop system crosses the imaginary axis at the origin in the complex plane. This type of loss of stability is termed steady-state, or static, bifurcation since the stable reference steady state becomes unstable while two new and stable steady states come into existence [Iooss and Joseph, 1980; Prairie and Bailey, 1986]. The second type of bifurcation which is important here is called Hopf bifurcation and occurs when a complex pair of leading eigenvalues crosses the imaginary axis. At Hopf bifurcation, the reference steady state loses stability and a limit cycle is born. Experience indicates that this limit cycle is stable; however, the possibility for it to be unstable exists [e.g. Heinemann and Poore, 1981; McDermott *et al.*, 1985]. It should be emphasized that bifurcation (i.e. loss of stability) occurs only if the eigenvalue(s) which crosses the imaginary axis has the largest real part (zero in the case of bifurcation) of all of the eigenvalues in the spectrum, hence the term *leading* eigenvalue. If there are eigenvalues with real parts greater than zero, bifurcation has already occurred and the reference steady state is unstable.

Two other eigenvalue situations are relevant to this discussion. An F_1 situation exists when the two leading eigenvalues form a repeated eigenvalue at the origin. F_1 bifurcations may result in the stable steady state giving way to relaxation-type oscillations [Lyberatos, Kuszta, and Bailey, 1985b]. The more complex F_2 structure exists when the three leading eigenvalues have zero real parts with one eigenvalue at the origin and the complex pair on the imaginary axis. One of these situations is present at intersections of the steady-state and Hopf bifurcation loci.

It is convenient to cast the linear problem into the framework of transfer functions where results of multivariate control theory can be applied. The block diagram for the closed-loop experimental system has been presented elsewhere [Prairie *et al.*, 1987]. Briefly, the system contains four dynamic components, a control block with transfer function $\mathbf{G_C}$, a mass flow controller block with transfer function $\mathbf{G_{mfc}}$, a block for the reactor with transfer function $\mathbf{G_R}$, and a block in the feedback loop containing the time delay transfer function, **D**. It was shown in other work that the transfer function for the IR analyzer can be well approximated by an identity matrix [Prairie *et al.*, 1987].

The transfer function for the linearized arctangent controllers based on ethylene measurements is

$$\mathbf{G_C} = \begin{bmatrix} -c_1 u_e & 0 & 0 & 0 \\ -c_1 u_h & 0 & 0 & 0 \\ 0 & 0 & 0 & 0 \\ 0 & 0 & 0 & 0 \end{bmatrix} \tag{20}$$

with $c_1 = \dfrac{2w}{\pi F_T^i}$. Transfer functions for the mass flow controllers were determined experimentally based on frequency response data [Prairie and Bailey, 1986]. They may be written

$$\mathbf{G_{mfc}} = \begin{bmatrix} g_e & 0 & 0 & 0 \\ 0 & g_h & 0 & 0 \\ 0 & 0 & 0 & 0 \\ 0 & 0 & 0 & 0 \end{bmatrix} = \begin{bmatrix} g_e(s)e^{\eta_e(s)i} & 0 & 0 & 0 \\ 0 & g_h(s)e^{\eta_h(s)i} & 0 & 0 \\ 0 & 0 & 0 & 0 \\ 0 & 0 & 0 & 0 \end{bmatrix} \tag{21}$$

where g(s) and $\eta(s)$ are functions that correspond to the amplitude ratio and phase shift response of the mass flow controllers to sinusoidal forcing of their set-points. The delay transfer function, **D**, is made up of the scalar function $e^{-\tau_D s}$ multiplied by an identity matrix which only contains entries at the first two diagonal locations. The experimental transport lag, τ_D was observed to be 3.21 s.

The transfer function for the (open-loop) reactor

$$\mathbf{G_R} = \frac{1}{\tau}\mathbf{C}[s\mathbf{I} - \mathbf{A}]^{-1}\mathbf{B}. \tag{22}$$

can be inserted into the overall transfer function for the closed-loop, linearized process,

$$\mathbf{T_R} = [\mathbf{I} + \mathbf{G_R G_{mfc} G_C D}]^{-1}\mathbf{G_R G_{mfc} G_C} \tag{23}$$

to obtain an expression for the characteristic function

$$p(s) = \det[\mathbf{I} + \mathbf{G_R G_{mfc} G_C D}]. \tag{24}$$

The characteristic equation, p(s) = 0, can be solved for the eigenvalues of the closed-loop process in terms of all system parameters, feedback gains, and time constants.

Equation (24) reduces to

$$p(s) = \tau\Delta(s) + c_1 u_e g_e(s) e^{-\tau_D s} C_{11}(s) + c_1 u_h g_h(s) e^{-\tau_D s} C_{12}(s) \tag{25}$$

where

$$\Delta(s) \equiv \det[\mathbf{A} - \mathbf{I}s] = s^4 + \phi_1 s^3 + \phi_2 s^2 + \phi_3 s + \phi_4 \tag{26}$$

and C_{ij} are the cofactors from the first column of $[\mathbf{A} - \mathbf{I}s]$,

$$C_{11}(s) = s^3 + \psi_{11} s^2 + \psi_{12} s + \psi_{13} \tag{27}$$

$$C_{12}(s) = \psi_{21} s^2 + \psi_{22} s + \psi_{23}. \tag{28}$$

In these equations, the terms ϕ_i and ψ_{ij} are scalars that contain the parameters and time constants of the **A** matrix.

The condition on p(s) which locates an eigenvalue at the origin in the complex plane is p(0) = 0; which becomes

$$u_h^{ss} = -\frac{\psi_{13}}{\psi_{23}} u_e - \frac{\tau\phi_4}{c_1\psi_{23}}. \tag{29}$$

This is an equation for a line in the feedback gain plane; (u_e,u_h) pairs on the line imply at least one zero eigenvalue. Steady-state bifurcation occurs for those pairs corresponding to leading eigenvalues. The line given by Eq. (29) will henceforth be called the steady-state bifurcation line. The intuitive result that neither the slope nor the intercept are functions of the surface time constants τ_{s1} and τ_{s2} can be verified through the definitions of ψ_{ij} and ϕ_4.

The condition which locates a pair of eigenvalues on the imaginary axis is $p(i\omega) = 0$. This condition gives rise to two transcendental equations that are parametric in ω. One equation results from setting $\mathrm{Re}(p(i\omega)) = 0$ and the other from $\mathrm{Im}(p(i\omega)) = 0$. In terms of the model parameters, these equations are

$$\begin{aligned} 0 = \omega^4 - \phi_2\omega^2 + \phi_4 + \frac{c_1 u_e}{\tau} g_e(\omega)\Big[(\psi_{13} - \psi_{11}\omega^2)\cos(\tau_D\omega + \eta_e) + (\psi_{12}\omega - \omega^3)\sin(\tau_D\omega + \eta_e)\Big] \\ + \frac{c_1 u_h}{\tau} g_h(\omega)\Big[(\psi_{23} - \psi_{21}\omega^2)\cos(\tau_D\omega + \eta_h) + \psi_{22}\omega\sin(\tau_D\omega + \eta_h)\Big] \end{aligned} \tag{30}$$

$$\begin{aligned} 0 = -\phi_1\omega^3 + \phi_3\omega + \frac{c_1 u_e}{\tau} g_e(\omega)\Big[(\psi_{12}\omega - \omega^3)\cos(\tau_D\omega + \eta_e) - (\psi_{13} - \psi_{11}\omega^2)\sin(\tau_D\omega + \eta_e)\Big] \\ + \frac{c_1 u_h}{\tau} g_h(\omega)\Big[\psi_{22}\omega\cos(\tau_D\omega + \eta_h) + (\psi_{23}\omega - \psi_{21}\omega^2)\sin(\tau_D\omega + \eta_h)\Big] \end{aligned} \tag{31}$$

Equations (30 and 31) are two linear equations for the two unknowns u_e and u_h and are parametric in ω, the Hopf bifurcation frequency. When $\omega = 0$, they degenerate into Eq. (29). As before, loss of stability, and hence Hopf bifurcation, only occurs when the feedback gain pair (u_e^H,u_h^H), which is a solution to the two equations, corresponds to a leading pair of eigenvalues $(\pm i\omega)$ for the closed-loop system. When Hopf bifurcation does occur, the instability produces a limit cycle with frequency ω.

Model calculations and bifurcation experiments were performed with the variables and

functions listed in Table 2. The reference feed conditions and feedback width w were chosen so as to span an interesting region of the intrinsic rate surface. As chosen, the closed-loop system operates over a feed range of $7 < F_e^i < 17$ sccm and $1 < F_h^i < 11$ sccm.

Figure 3 contains a typical bifurcation diagram calculated with the model and the data in Table 2. The dashed line in Fig. 3a is the steady-state bifurcation line from Eq. (29). The position and slope of this line depend soley on steady state kinetics, and as was observed for a slightly different catalyst [Prairie and Bailey, 1986], are of little use for model validation. The solid curve in Fig. 3a is the Hopf bifurcation locus calculated from the simultaneous solution of Eqs. (30 and 31) with ω as a parameter. The surface time constants τ_{s1} and τ_{s2} were chosen to be 0.74 s and 5000 s, respectively, for the purpose of constructing the curve. The significance of these values is explained later. The Hopf curve originates on the steady-state line at an F_1 bifurcation point given by $p(0) = p'(0) = 0$. The frequency parameter increases continuously along the Hopf curve moving away from the F_1 point. This effect is clearly demonstrated in the ω versus u_e plot of Fig. 3b. As ω continues to increase, the Hopf curve winds around and intersects the steady-state bifurcation line at an F_2 bifurcation point. The spiraling of the Hopf curve is a manifestation of the transcendental nature of the characteristic equation due to the presence of time delay. Although not shown, it is possible for the Hopf curve to intersect itself, a phenomenon that could give rise to higher order bifurcations if the intersection occurs on a stability boundary [Lyberatos, 1985].

Calculations were performed to determine the leading eigenvalues for various locations in the u_e,u_h stability plane. For gains in the lower right-hand side of Fig. 3, where the reference steady state is unstable, the leading eigenvalue lies to the right of the imaginary axis and is real. In the upper left-hand side, above the Hopf curve, the leading eigenvalues make up a complex conjugate pair with positive real parts. When the feedback gains lie in that region below the

steady-state line and above the Hopf curve, either unstable leading eigenvalue configuration can exist. In any case, eigenvalue calculations showed that the curves in Fig. 3 correspond to the crossing of leading eigenvalues into the right-half plane, and hence describe stability boundaries.

Experiments were performed to determine the Hopf bifurcation curve for the closed-loop reactor system. Hopf bifurcation points were located for different values of the hydrogen gain, u_h, by incrementing u_e away from points of stability until stable oscillations appeared for ethylene in the reactor effluent. Figure 4 shows the progress of a typical Hopf bifurcation experiment. In this figure, data for $u_h = -150$ are presented. Each frame of the figure contains data for the ethylene deviation variable, $\hat{x}_1$, during the last 90 seconds of a 60 minute run. It can be seen that the Hopf bifurcation point at $u_h = -150$ occurs in the interval $-65 < u_e^H < -70$.

A better estimate of the bifurcation point can be found using the asymptotic expansion

$$u_e - u_e^H = \varepsilon^2 \delta'(0) + O(\varepsilon^2) \tag{32}$$

where u_e^H is the bifurcation point, ε is the oscillation amplitude and $\delta'(0)$ is a constant [Halbe and Poore, 1981]. Thus, to first order, a plot of ε^2 versus u_e should yield a line which intersects the abscissa at the true Hopf bifurcation point, u_e^H. It cannot be assumed *a priori* that the gains in Fig. 4 are close enough to u_e^H to justify the use of Eq. (32). However, Figure 5 shows that when the data in Fig. 4 are plotted according to Eq. (32), a reasonable line results which can be extrapolated to the bifurcation gain, $u_e^H = -66.5$. Figure 5 also shows amplitude and frequency plotted against u_e. The amplitude data in Fig. 5 have been scaled with the largest amplitude that was observed experimentally, namely, that seen in the last frame of Fig. 4, which corresponds to $u_e = -85$. Frequency is essentially independent of the feedback gain near the bifurcation point.

Data for 23 hydrogen gains ranging from -650 to 650 were recorded. Equation (32) is less valid for hydrogen gains with large absolute values and eyeball estimates of some of the bifurca-

tion points were necessary. Uncertainty in the estimates never exceeded ±5 units in ethylene gain. Obtaining estimates for a bifurcation point at a large gain is troublesome because the large gain amplifies measurement noise in the closed-loop process. Near Hopf bifurcation, the perturbation induces periodic oscillations with a frequency characteristic of the bifurcation frequency. Hence, noise induced oscillations exist in the theoretically stable region of gain space. Mathematically, as the system approaches bifurcation, two eigenvalues of the linearized process have very small real parts, so perturbations result in only slightly damped oscillations. This problem of noise-induced oscillation was partially solved by performing several repetitions of the same experiment.

An objective of the Hopf bifurcation experiments was to use the data to test the mathematical model and to obtain estimates for τ_{s1} and τ_{s2}. Figure 6 presents Hopf bifurcation points and frequencies in comparison to model calculations. The surface time constants that were used in the calculation were obtained by applying the Marquardt-Levenberg minimization scheme to an objective function, $F_o(\tau_{s1},\tau_{s2})$, which includes bifurcation points and frequencies.

$$F_o(\tau_{s1},\tau_{s2}) = \sum_{j=1}^{23}\left[w(\omega_j - \omega(u_{h,j}))^2 + (u_{e,j}^H - u_e^H(u_{h,j}))^2\right] \tag{33}$$

where $u_{h,j}$ are the 23 independent hydrogen gains, and j denotes the experimental observations at each $u_{h,j}$. The term w is a weighting value to account for the difference in magnitude between the gains and the frequencies.

Solutions to two slightly different minimization problems are presented in Fig. 6. When w = 10000, τ_{s1} = 0.74 s corresponds to a minimum in the objective function that results in a frequency correlation coefficient, r_ω^2, of 0.96 and an ethylene gain correlation coefficient, $r_{u_e}^2$, of 0.90. The value τ_{s1} = 1.6 s results when w = 10. This solution corresponds to r_ω^2 = 0.96 and $r_{u_e}^2$ = 0.89. Figure 6 also presents the Hopf stability curve for the case of τ_{s1} = 0.025 s. As was true for the

step-response data, the Hopf bifurcation data are relatively insensitive to τ_{s2}, provided it is large. The value τ_{s2} = 5000 s was chosen for the purpose of the model-data comparisons shown in Fig. 6. Values for τ_{s1} as low as 0.025 s yield reasonably good agreement with the experimental data. The experimental and calculated curves diverge for τ_{s1} larger than 1.6 s. It is notable that the Hopf experiments identified a time scale which is smaller than the mean residence time of the reactor. This work provides an experimental demonstration of the theoretical suggestion of Kuszta and Sinha (1980) that small time constants not detectable from open-loop transient data can be estimated from closed-loop experiments.

CYCLED-FEEDSTREAM EXPERIMENTS

The slow transients that were observed for the step-response experiments suggest that the time-average reaction rate might be enhanced by periodically forcing the feedstream composition. To test this hypothesis, three cycled-feedstream experiments were performed in order to study the effects of forcing period, ethylene composition, and hydrogen composition for symmetric, square wave forcing of the reactor feed composition.

Operating parameters for each experiment are listed in Table 3. For each experiment, symmetric, square-wave switching (duty fraction equal to 0.5) between feeds A and feeds B was applied to the experimental CSTR, operating in the open-loop configuration at 80 °C, ambient pressure, and 100 sccm total feed. Experiment I was performed to determine the forcing period which produces the optimum time-average reaction rate, given the fixed value for the time-average ethylene feed concentration, $\bar{x}_1$, of 0.10. Experiments II and III were performed to investigate the effect of the time-average ethylene feed fraction on the time-average reaction rate for periodic operation at the optimum period (180 s) which was determined in Experiment I. Time-average ethylene feed fractions were manipulated by varying the ethylene amplitude of the square-wave forcing function (i.e. feed compositions B in Table 3). Experiments II and III differ

in the amount of hydrogen contained in the ethylene-deficient feedstream (feed streams A, Table 3).

Effluent ethylene mole fraction trajectories for four forcing periods from Experiment I are presented in Fig. 7. These data show periodic behavior of the reactor 6 hrs into each run. Initial transients are not shown. Since the data are plotted as mole percent ethylene in the reactor effluent, lower values suggest higher instantaneous reaction rates.

Estimates for time-average reaction rates can be calculated from the time-dependent ethylene profiles using two different methods. Method 1 is derived from the time- (integral-) average gas-phase ethylene and overall material balances by assuming that $\overline{F_T^o x_1}$ is equal to $\bar{F}_T^o \bar{x}_1$, where overbars denote time-average quantities. This assumption is valid when the total molar effluent flowrate, F_T^o, is approximately constant. Time-average reaction rates are calculated with Method 1 according to

$$\bar{r} = \frac{F_T^i(\bar{x}_1^i - \bar{x}_1)}{1 - \bar{x}_1}. \tag{34}$$

This equation is simply the steady-state CSTR equation with time-average quantities.

Method 2 provides an alternative approach for calculating the time-average reaction rate. It relies on the approximation that the difference between the instantaneous rate of disappearance of gas-phase hydrogen and the production rate of ethane is small compared to the time-average consumption rate of ethylene. The lack of any information concerning the gas-phase hydrogen concentration makes it difficult to assess the validity of this approximation. The time-average rate formula for Method 2 is

$$\bar{r} = F_T^i(\bar{x}_1^i - \bar{x}_1) + \frac{F_T^i}{T}\int_{t_o}^{t_o+T} \frac{x_1(x_1^i - x_1)}{1 - x_1} dt \tag{35}$$

where the integral on the right hand side accounts for the nonequimolar nature of the reaction

stoichiometry.

Figure 8 shows the time-average reaction rates for Experiment I calculated using both methods. The solid squares indicate rates calculated with Method 1 and the open squares indicate those calculated using Method 2. Although Method 1 values are consistently lower, they are all within 2.5% of the corresponding Method 2 calculations. It is expected that $\bar{r} \rightarrow$ r(average composition) = 5.1 μmol/s in the limit of small period and that $\bar{r} \rightarrow \frac{r(\text{comp. A}) + r(\text{comp. B})}{2} \approx 1.9$ μmol/s in the limit of very large period [Bailey, 1977]. It can be seen in Fig. 8 that an optimum forcing period exists between 100 and 1000 s. The value of 180 s was chosen for all subsequent experiments.

It is important that cycled-feedstream results be compared with steady-state data corresponding to feed compositions that are equal to the time-average counterparts for the cycling experiments. Figure 9 compares time-average reaction rates (Method 2) from Experiments II and III with steady-state behavior that was observed for 20% H_2 in the feed. Experiment II produced a 31% improvement in the time-average reaction rate at conditions that normally yield a local maximum in the steady-state reaction rate. Experiment III involved switching between a reaction stream containing 20% H_2 and a stream contiaining pure He, so the time-average hydrogen feed fraction was 10% (Table 3). Hence, reaction rates for Experiment III should be compared against steady-state data for 10% H_2 in the reactor feed. Unfortunately, this experiment was not performed. Examination of the 11% H_2 data in Fig. 1 suggests, however, that significant enhancement (> 25%) would be observed, had the 10% experiment been performed. The outstanding feature of Fig. 9 is that enhancement was observed for the entire range of ethylene feed levels, and is greatest at conditions which normally give rise to a maximum in the steady-state kinetics.

Forcing the reactor feed composition according to the parameters and compositions in Table 3 produces reaction rate enhancement by taking advantage of the difference in the rates of

catalyst deactivation and reactivation. In the presence of ethylene and hydrogen, the activity of the catalyst deteriorates very slowly in comparison to the rate at which it regains its activity during the ethylene-deficient half of the feed forcing schedule. This observation was confirmed in separate step-response experiments where the feed to the catalyst whose activity has been reduced in a reaction environment was suddenly switched to pure helium for approximately 10 s, and then switched back to the original reactant mixture. Although those data are not presented, they indicate that after 10 s in helium, the catalyst nearly returns to it's original high level of activity.

The observation that $\bar{r}$ for Experiment II are greater than $\bar{r}$ for Experiment III results from the difference in the time-average hydrogen feed fractions, $\overline{x_2}$, that were employed (0.2 versus 0.1, respectively). The lack of ethylene in the feed is sufficient, and hydrogen need not be present, for catalyst reactivation. It is possible that the reversible adsorption of a site-blocking ethylene species (possibly on sites other than Pt) is responsible for the asymmetric cycling trajectories.

Analysis of Fig. 7 shows that some aspect of regeneration requires longer than one hour. The effluent ethylene mole fraction at the end of the period on curve (b) lies above that at 90 s on curve (c). Similarly, the value at the end of the period in curve (c) lies above that for the 900 s point on curve (d). Since larger values for the ethylene effluent fraction indicate lower instantaneous reaction rates and hence a lesser extent of regeneration, the catalyst is not completely regenerated even after lean operation for up to one hour (the time spent without ethylene in curve (d)). A very fast component to catalyst regeneration is also indicated, so it is possible that two time scales contribute to the catalyst reactivation process.

Attempts to find τ_{s1} and τ_{s2} such that the dynamic model describes the ethylene time trajectories and the time-average rate results failed. A complicated mathematical description involving site-blocking ethylene species, hydrogen spillover, and interactions among the elementary surface

steps is probably necessary to explain all of the experimental observations. It is concluded that large-amplitude forced-cycling experiments in the proper frequency range impose the most rigorous test of the validity of dynamic models for this system, and probably for other catalytic reactions as well.

DISCUSSION

Steady-state kinetic, step-response, feedback-induced Hopf bifurcation, and cycled-feedstream studies span the spectrum of experiments that use fluid-phase measurements for developing mathematical models for heterogeneous catalytic reaction kinetics. A model that accurately describes reactor behavior for such a wide variety of transient stimuli would be reliable for design, control and dynamic optimization purposes, albeit more fundamental studies would still be necessary to verify the proposed chemistry. Before research begins, the basic question should be answered: For what is the model to be used? A detailed picture of the reaction chemistry requires direct observation of surface intermediates, for example, using the technique of transmission infrared spectroscopy [e.g. Barshad *et al.*, 1985; Cavanagh and Yates, 1981; Soma, 1979], whereas useful phenomenological models can be obtained through the techniques that are presented here.

The proposed model in steps (I-IV) with first order hydrogen adsorption provides an adequate description of steady-state kinetics. Step-response and Hopf bifurcation experiments can be described with the model but they yield very different estimates for the time constant τ_{s1}. This indicates that the proposed mechanism is inconsistent with these data, and probably requires at least one additional step, possibly to account for hydrogen adsorption and catalytic reaction on a different type of surface site. As the model is written, τ_{s1} must be viewed as a phenomenological model parameter and not as a fundamental physical constant. The step-response results indicate that τ_{s1} is 5000 s whereas the Hopf bifurcation data suggest $0.025\ \text{s} < \tau_{s1} < 1.6\ \text{s}$. Open-loop step

experiments which tend to focus on behavior that occurs on long time scales are complemented by feedback experiments which are useful for identifying contributions from faster processes in the system. Through the technique of feedback-induced bifurcation, small time constants which normally are ignored via open-loop identification, and are important for modeling and controller design, can be identified. The existence of two vastly different time constants suggests that two processes associated with adsorbed hydrogen and possibly two types of adsorption sites are operative for ethylene hydrogenation on 0.05% Pt/Al_2O_3.

The slow process is surprising in comparison to the hydrogen chemisorption prediction that $\tau_{s1} = \frac{N_T}{F_T^i} = 0.006$ s (17% disperse Pt at 0.05% loading). Clearly, the model must be improved to account for this discrepancy. A possible explanation is that hydrogen spillover occurred during catalyst pretreatment to activate sites on the alumina support for catalytic activity.

Research on hydrogen spillover from Pt to alumina has appeared frequently in the literature [e.g. Bianchi *et al.*, 1975; Bianchi *et al.*, 1981; Cavanagh and Yates, 1981; Kramer and Andre, 1979; Nakano and Kusunoki, 1985; Sinfelt and Lucchesi, 1963; Teichner *et al.*, 1977]. Bianchi *et al.* (1975) reported that spillover activated alumina adsorbs gas-phase hydrogen (in the absence of metal) and is active for ethylene hydrogenation. Alumina sites would compete with metal sites for ethylene hydrogenation. An Eley-Rideal type reaction with gaseous ethylene and alumina-adsorbed hydrogen might be the elementary step that describes this process. Other researchers have observed a significant contribution to the steady-state reaction rate due to hydrogen spillover [Carter *et al.*, 1965; Sinfelt and Lucchesi, 1963]. Transient work in this area has been limited to batch processes which suggest that spillover and subsequent reaction with ethylene are very slow and occur over time periods of several hours. Ongoing efforts in our laboratory are aimed at studying hydrogen spillover and its effect on the dynamics of ethylene hydrogenation.

While the step-response method probes slow details of the overall kinetics, feedback-induced Hopf bifurcation centers on processes that occur much more rapidly, on a time scale which is similar to that expected for chemisorbed hydrogen on the Pt sites within the catalyst pellet. Two question arise concerning the significance and sensitivity of the Hopf results: (1) Do the Hopf bifurcation data actually reflect something about the surface dynamics; or is it simply the reactor with delay that dominates the bifurcation behavior? and (2) How sensitive is the Hopf stability diagram to τ_{s1} in comparison to the value suggested by the step experiments?

The answer to question (1) is presented graphically in Fig. 10a which shows the stability diagram calculated for the two-dimensional case where the two surface species are assumed to be at quasi-steady state (solid curve; $\tau_{s1},\tau_{s2} \rightarrow 0$). Clearly, this model is in disagreement with the experimental data. Hence it is concluded that surface dynamics must be considered for acceptable agreement between the model and the data. Question (2) is also addressed in Fig. 10a (broken curve) which shows that the stability diagram for τ_{s1} equal to the step-response value of 5000 s also disagrees with the data. Both the step-response and the Hopf bifurcation experiments were necessary to discover the existence of *two* characteristic time scales associated with chemisorbed hydrogen.

Cycling the feedstream composition between a reactive mixture and a stream lacking ethylene takes advantage of the slow transient associated with adsorbed hydrogen to produce time-average rate improvement for the range of time-average ethylene feed compositions that was employed. This range includes conditions that produce a local maximum, and hence optimum, in the intrinsic steady-state reaction rate surface. The observed rate improvement is clearly due to surface dynamics and is not a result of the favorable averaging of a spectrum of steady states. The latter has been speculated to be the cause of rate enhancement by forced composition cycling [Nowobilski and Takoudis, 1986]. The maximum near T = 400 s in Fig. 8 suggests that the sys-

tem involves yet a fourth surface time constant, one that is near 400 s in magnitude.

Cycled-feedstream results are difficult to analyze in terms of a mathematical model because of the inherently complicated system of differential equations which must be solved numerically. While step-response simulators generally reproduce behavior dominated by a single long time scale, cycled-feedstream experiments stimulate interactions among all of the time scales in the model. Further, feedback-induced Hopf bifurcation calculations are more straightforward and less complicated than modeling cycled-feedstream responses. Although cycled-feedstream experiments provide a rigorous test of model validity, they are difficult to use for constructive model development.

A final comment concerns the ambiguity of the step-response and feedback- induced Hopf bifurcation techniques toward the second surface time constant, τ_{s2}. That τ_{s2} can be arbitrarily large for the dynamic experiments suggests that step (II) is at quasi-steady state, and hence that $\theta_{C_2H_3*}$ can be taken at its initial value. This assumption, however, is inconsistent with the steady-state kinetic data. Hopefully a more complete model will remove this ambiguity.

NOTATION

$\mathbf{A}$	Jacobian matrix evaluated at reference conditions
a_{ij}	elements of $\mathbf{A}$
c_1	scale factor for feedback gains
C_f	bulk concentration, mol/cm^3
C_{ij}	cofactors of [$\mathbf{A}$–$\mathbf{I}s$]
$\mathbf{D}$	delay transfer function
D_e	effective diffusivity, cm^2/s
F	molar flow rate, sccm or mol/s
F_o	objective function for nonlinear regression
f_i	nonlinear material balance on species i
$\mathbf{G}$	transfer function
g(s)	amplitude ratio in Laplace space for mass flow controller
K	equilibrium rate coefficient
k_i	rate coefficient, μmol/s (1 mol = 10^6μmol)
l	characteristic length for diffusion, cm
m	order for hydrogen adsorption
N_T	number of sites, mol
n	reactor capacity, mol
p(s)	characteristic function for the closed-loop system
r_o	observed reaction rate, mol/s
r(x,y)	steady-state intrinsic rate surface, mol/s
$\bar{r}$	time-average reaction rate, mol/s
r^2	multiple correlation coefficient
$\mathbf{T_R}$	overall closed-loop transfer function
T	forcing period, s
t	time, s
t_o	arbitrary time for lower limit of integration, s
$\mathbf{u}$	vector of manipulated variables
u	feedback gain
w	weighting factor
w	half-width of feedback function, sccm
$\mathbf{x}$	vector of states
x	gas-phase mole fraction
$\mathbf{y}$	vector of outputs
η(s)	phase shift in Laplace space for mass flow controller
θ_i	fractional coverage by species i
τ	reactor mean residence time, s
τ_D	time delay, s
τ_{s1}	surface time constant for chemisorbed hydrogen, s
τ_{s2}	surface time constant for poisoning step
ϕ_i	coefficients in det[$\mathbf{A}$-$\mathbf{I}s$]
ϕ_o	observable modulus
ψ_{ij}	coefficients in the cofactors C_{ij}
ω	bifurcation frequency parameter, rad/s

subscripts

c	controller
e	ethylene
He	helium
h	hydrogen
j	j^{th} observation
mfc	mass flow controller
R	reactor
ref	reference condition
T	total
v	vacancies
1	ethylene
2	hydrogen

superscripts

H	Hopf bifurcation
i	inlet
o	outlet
ref	reference condition
ss	steady-state bifurcation

REFERENCES

Aluko, M. (1983). Multiple-time-scale-analysis of heterogeneous catalytic reaction systems. Doctoral dissertation, University of California at Santa Barbara.

Antonucci, P., N. VanTruong, N. Giordano, and R. Maggiore (1982). Hydrogen spillover effects in the hydrogenation of benzene over Pt/γ–Al_2O_3 catalyst. *J. Catal.* **75,** 140-150.

Aris, R. (1975). *The Mathematical Theory of Diffusion and Reaction in Permeable Catalysts.* Oxford University Press, London.

Bailey, J. E., and F. Horn (1970). Catalyst selectivity under steady-state and dynamic operation: an investigation of several kinetic mechanisms. *Ber. Bunsenges. Phys. Chem.*, **74,** 611-617.

Bailey, J. E. (1977). Periodic phenomena. *Chemical Reactor Theory: A Review.* Lapidus, L. and N. R. Amundson, eds. Prentice-Hall, 758-813.

Barshad, Y., X. Zhou, and E. Gulari (1985). Carbon monoxide oxidation under transient conditions: a FTIR spectroscopy study. *J. Catal.* **94,** 128-141.

Bennett, C. O. (1976). The transient method and elementary steps in heterogeneous catalysis. *Catal. Rev.-Sci. Engng.* **13,** 121-148.

Bianchi, D., G. E. E. Gardes, G. M. Pajonk, and S. J. Teichner (1975). Hydrogenation of ethylene on alumina after hydrogen spillover. *J. Catal.* **38,** 135-146.

Bianchi, D., M. Lacroix, G. M. Pajonk, and S. J. Teichner (1981). Spilled-over hydrogen transport from platinum-on-alumina catalyst to methoxylated silica aerogel. *J. Catal.* **68,**

411-418.

Bilimoria, M. R., and J. E. Bailey (1978). Dynamic studies of acetylene hydrogenation on nickel catalysts. *ACS Symposium Series 65, Chemical Reaction Engineering,* 526.

Carter, J. L., P. J. Lucchesi, J. H. Sinfelt, and D. J. C. Yates (1965). 3rd *Int. Congr. Catal.* **1,** 644.

Cavanagh, R. R., and J. T. Yates, Jr. (1981). Hydrogen spillover on alumina: a study by infrared spectroscopy. *J. Catal.* **68,** 22-26.

Cutlip, M. B. (1979). Concentration forcing of catalytic surface rate processes. *AIChE J.* **25,** 502-508.

Cutlip, M. B., C. J. Hawkins, D. Mukesh, W. Morton and C. N. Kenney (1983). Modelling of forced periodic oscillations of carbon monoxide oxidation over platinum catalyst. *Chem. Engng. Commun.* **68,** 329-344.

Dettmer, M., and A. Renken (1983). Kinetic studies on the formation of ethylene acetate under stationary and non-stationary conditions. *Ger. Chem. Engng.* **6,** 356.

Eigen, M., and L. de Maeyer (1963). Relaxation methods. *Technique of Organic Chemistry Vol.* **8,** 895-1054.

Ertl, G., P. R. Norton, and J. Rustig (1982). Kinetic oscillations in platinum-catalyzed oxidation of CO. *Phys. Rev. Letters* **49,** 177-180.

Feimer, J. L., A. K. Jain, R. R. Hudgins, and P. L. Silveston (1982). Modelling forced periodic operation of catalytic reactors. *Chem. Engng. Sci.* **37,** 1797-1805.

Graham, W. R. C., and D. T. Lynch (1984). Model validation through an experimental investigation of resonant behavior for the catalytic oxidation of carbon monoxide on platinum. *Catalysis on the Energy Scene.* 197-204.

Halbe, D. C., and A. B. Poore (1981). Dynamics of the continuous stirred tank reactor with reaction A→B→C. *Chem. Engng. J.* **21,** 241-253.

Happel, J., and P. H. Sellers (1982). Multiple reaction mechanisms in catalysis. *Ind. Engng. Chem. Fundam.* **21,** 67-76.

Hecker, W. C., and A. T. Bell (1983). Reduction of NO by CO over silica-supported rhodium: infrared and kinetic studies. *J. Catal.* **84,** 200-215.

Heinemann, R. F., and A. B. Poore (1981). Multiplicity, stability, and oscillatory dynamics of the tubular reactor. *Chem. Engng. Sci.* **36,** 1411-1419.

Herz, R. K., and S. P. Marin (1980). Surface chemistry models of carbon monoxide oxidation on supported platinum catalysts. *J. Catal.* **65,** 281-296.

Iooss, G. and D. D. Joseph (1980). *Elementary Stability and Bifurcation Theory.* Springer-Verlag, New York.

Kaul, D. J., and E. E. Wolf (1984). FTIR studies of surface reaction dynamics I. *J. Catal.* **89,** 348-361.

Kaul, D. J., and E. E. Wolf (1985). FTIR studies of surface reaction dynamics II. *J. Catal.* **91,** 216-230.

Kobayashi, M. (1982). Characterization of transient response curves in heterogeneous catalysis I. *Chem. Engng. Sci.* **37,** 393-401.

Kobayashi, H., and Kobayashi, M. (1974). Transient response method in heterogeneous catalysis. *Catal. Rev.-Sci. Engng.* **10,** 139-176.

Kramer, R., and M. Andre (1979). Adsorption of atomic hydrogen on alumina by hydrogen spill-over. *J. Catal.* **58,** 287-295.

Kuszta, B., and J. E. Bailey (1982). Nonlinear model identification by analysis of feedback-stimulated bifurcation. *IEEE Trans. Autom. Control* **AC-27,** 227-228.

Kuszta, B., and N. K. Sinha (1980). On identification of linear systems with feedback: high gain feedback case. *Int. J. Systems Sci.* **11,** 403-409.

Lyberatos, G. (1985). The effect of time delay on the feedback identification of chemical reaction systems. *Chem. Engng. Sci.* **40,** 2160-2162.

Lyberatos, G., B. Kuszta, and J. E. Bailey (1984). Discrimination and identification of dynamic catalytic models via introduction of feedback. *Chem. Engng. Sci.* **39,** 739-750.

Lyberatos, G., B. Kuszta, and J. E. Bailey (1985a). Normal forms for chemical reaction systems via the Affine transformation. *Chem. Engng. Sci.* **40,** 199-208.

Lyberatos, G., B. Kuszta, and J. E. Bailey (1985b). Versal families, normal forms, and higher order bifurcations in dynamic chemical systems. *Chem. Engng. Sci.* **40,** 1177-1189.

Lynch, D.T., G. Emig, and S. E. Wanke (1986). Oscillations during CO oxidation over supported metal catalysts. III. Mathematical modeling of the observed phenomena. *J. Catal.* **97,** 456-468.

McDermott, P. E., H. -C. Chang, and R. G. Rinker (1985). Experimental investigation of controller-induced bifurcation in a fixed-bed autothermal reactor. *Chem. Engng. Sci.* **40,** 1355-1366.

Mullins, M. E. (1982). Hydrocarbon reactions over transition metals: observation of surface hydrogen. Doctoral dissertation, University of Rochester.

Nakano, K, and K. Kusunoki (1985). Role of hydrogen spillover in a hydrogenation reaction on monometallic (Ru, Rh, Pd, or Pt) and bimetallic (Ru-Pd) catalyst. *Chem. Engng. Commun.* **34,** 99-109.

Nowobilski, P. J, and C. G. Takoudis (1986). Periodic operation of chemical reactor systems: are global improvements attainable? *Chem. Engng. Commun.* **40,** 249-264.

Oh, S. H. (1985). Personal communication.

Oh, S.H., G.B. Fisher, J.E. Carpenter, and D.W. Goodman (1986). Comparative kinetic studies of CO-O_2 and CO-NO reactions over single crystal and supported rhodium catalysts. *J. Catal.* **100,** 360-376.

Oh, S. H., and L. L. Hegedus (1980). Dynamics of high-temperature carbon monoxide chem-isorption on platinum- alumina by fast-response IR spectroscopy. *Catalysis Under Transient Conditions, ACS Symposium Series 178,* 79-103.

Pikios, C. A., and D. Luss (1977). Isothermal concentration oscillations on catalytic surfaces. *Chem. Engng. Sci.* **32,** 2191-2194.

Prairie, M. R, and J. E. Bailey (1986). Application of feedback-induced bifurcation for evaluating steady-state and transient heterogeneous catalysis kinetic models. *Chem. Engng. Sci.* **41,** 937-944.

Prairie, M. R., S. H. Oh, B. K. Cho, and E. J. Shinouskis and J.E. Bailey. Steady-state and transient studies of CO oxidation on alumina supported rhodium via transmission IR spectroscopy. In preparation.

Prairie, M. R., Shanks, B. H. and J. E. Bailey. (1987). Intentional manipulation of closed-loop time delay for model validation using feedback-induced bifurcation. Submitted to *Chem. Engng. Sci.*

Saltsburg, H., and M. E. Mullins (1982). Surface hydrogen in heterogeneous catalysis. *Ann. New York Acad. Sci.* 82-96.

Sinfelt, J. H., and P. J. Lucchesi (1963). Kinetic evidence for the migration of reactive intermediates in surface catalysis. *J. Amer. Chem. Soc.* **85,** 3365-3367.

Slin'ko, M. G., and M. M. Slin'ko (1978). Self-oscillations of heterogeneous catalytic reaction rates. *Catal. Rev.-Sci. Engng.* **17,** 119-153.

Smith, C. B. (1983). Dynamic modelling and optimization of lumped chemical processes. Doctoral dissertation, University of Houston.

Smith, J. M. (1981). *Chemical Engineering Kinetics.* McGraw-Hill, Inc., New York.

Solymosi, F., and J. Sarkany (1979). An infrared study of the surface interaction between NO and CO on Rh/Al_2O_3 catalyst. *App. Surface Sci.* **3,** 68-82.

Soma, Y. (1979). Infrared spectra of ethylene adsorbed on transition metals at low temperature and hydrogenation of adsorbed species. *J. Catal.* **59,** 239-247.

Swartz, J. A., and R. J. Madix (1974). Modulated beam relaxation spectroscopy: its application to the study of heterogeneous kinetics. *Surface Sci.* **25,** 2317-2341.

Teichner, S. J., A. R. Mazabard, G. M. Pajonk, G. E. E. Gardes, and C. H. Van (1977). Hydrogen spillover in catalytic reactions I: activation of alumina. *J. Coll. and Interface Sci.* **58,** 88-99.

Weisz, P. B. (1973). Diffusion and chemical transformation. *Science* **179,** 433-440.

Williams, S. D., and K. W. Hipps (1982). The adsorption of 1-propanol, 1-propylamine, and 3-amino-1-propanol on plasma-grown aluminum oxides; comparison with propanoic acid and β-alanine. *J. Catal.* **78,** 96-110.

Table 1. Nonlinear regression results for steady-state kinetic data.

Parameter	m = 1	m = 2
k_1 (μmol/s)	353	371
K	48.7	2.42
K_{eq}	29.2	29.1
k_4 (μmol/s)	26.0	42.4
SSQ $(\mu mol/s)^2$	9.19	9.08
r^2	0.93	0.93

Table 2. Data for the Hopf bifurcation experiments and simulations.

F_T^i	100 sccm
F_e^{ref}	012 sccm
F_h^{ref}	006 sccm
w	005 sccm
Experimental value for $x_{1,ref}$	0.1053
Calculated values based on F_e^{ref} and F_h^{ref}	
$x_{1,ref}$	0.1026
$x_{2,ref}$	0.0414
$\theta_{1,ref}$	0.1362
$\theta_{2,ref}$	0.3576
$g_e(\omega)$	$\left[(0.22\omega)^2 + 1\right]^{-\frac{1}{2}}$
$g_h(\omega)$	$\left[(1.07\omega)^2 + 1\right]^{-\frac{1}{2}}$
$\eta_e(\omega)$	-0.43ω
$\eta_h(\omega)$	$\mathrm{Tan}^{-1}(-1.07\omega)$ $- 0.14\omega$

Table 3: Operating conditions for the three cycled-feedstream experiments.

Experiment	Feed Compositions	Forcing Period, T (s)	$\bar{x}_1$	$\bar{x}_2$
I	A: 20% H_2, no C_2H_4 B: 20% H_2, 20% C_2H_4	$10 < T < 10^4$	10%	20%
II	A: 20% H_2, no C_2H_4 B: 20% H_2, 0 - 20% C_2H_4	180	0 - 10%	20%
III	A: Pure He B: 20% H_2, 0 - 20% C_2H_4	180	0 - 10%	10%

FIGURE CAPTIONS

Fig. 1 Steady-state kinetic data and model calculations for m=1 (solid) and m=2 (dashed). F_T^i=100 sccm, 80 °C, ambient pressure. (a)-circles 20% H_2 in feed, (b)-triangles 11% H_2, (c)-squares 8% H_2, (d)-diamonds 5% H_2.

Fig. 2 Step-response data (dots) and model calculations (solid curves) for m=1, τ_{s1} = 5000 s and τ_{s2} = 5000 s. (a) Step experiment A (18% H_2 switched to 18% H_2 and 18% C_2H_4.) (b) Step experiment B (18% H_2 switched to 20% H_2 and 14% C_2H_4.)

Fig. 3 (a) Stability diagram in feedback gain space. τ_{s1}=0.74s and τ_{s2} = 5000 s. (b) Development of the Hopf bifurcation frequency parameter with respect to ethylene gain. Dashed line is the steady-state bifurcation line. Solid curves correspond to the Hopf eigenvalue criterion ($p(i\omega) = 0$).

Fig. 4 Hopf bifurcation data for u_h = -150, $x_{1,ref}$ = 0.1053.

Fig. 5 Normalized oscillation amplitude, ε, amplitude squared, ε^2, and bifurcation frequency, ω as functions of the bifurcation gain, u_e, for u_h = -150. Triangles-ε, circles-ε^2, squares-ω.

Fig. 6 Experimental and calculated Hopf stability curve and bifurcation frequency. —···—τ_{s1}=0.025 s; ————τ_{s1}=0.74 s; – – – –τ_{s1}=1.6 s; — —steady-state bifurcation line. τ_{s2}=5000 s for all Hopf curves.

Fig. 7 Raw data for several periods from cycled-feedstream Experiment I. (a) Forcing period, T, = 30 s; (b) T = 180 s; (c) T = 1800 (s); (d) T = 7200 s.

Fig. 8 Time-average reaction rate dependence on forcing period: Cycled-feedstream Experiment I. Solid squares - Method 1, Open squares - Method 2.

Fig. 9 Time-average reaction rate dependence on time-average ethylene feed fraction for cyclic forcing at T = 180 s. Squares: Experiment II. Triangles: Experiment III. Diamonds: steady-state intrinsic rates for 20% H_2 in the reactor feedstream.

Fig. 10 Stability diagrams for the cases: solid- $\tau_{s1} = \tau_{s2} = 0$ (quasi-steady state approximation applied to surface species). broken- $\tau_{s1} = \tau_{s2}$ = 5000 s (step-response values). (a) Stability diagram in gain space. (b) Hopf bifurcation frequency behavior.

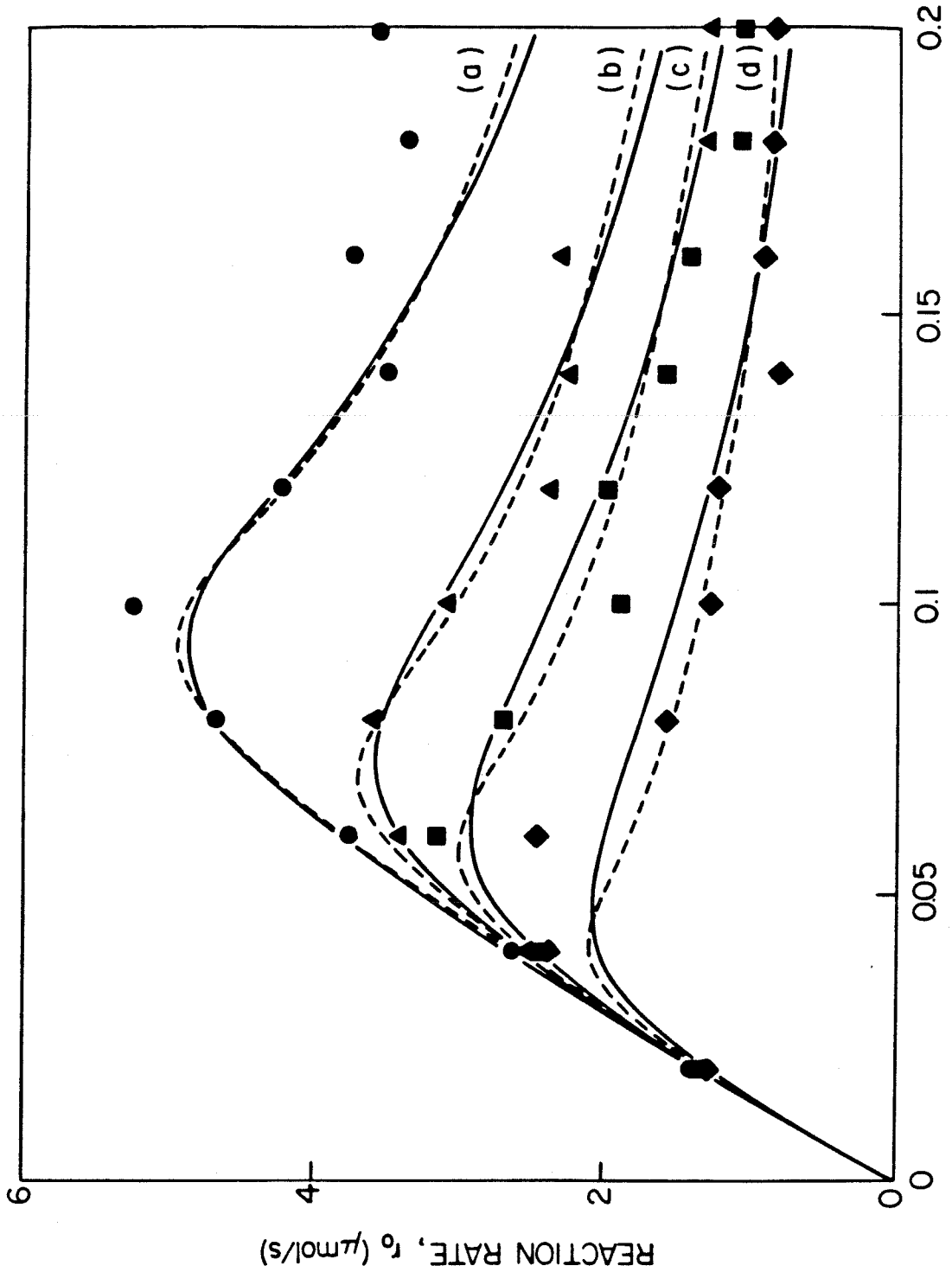
REACTION RATE, r_o (μmol/s)
0
2
4
6
0
0.05
0.1
0.15
0.2
ETHYLENE MOLE FRACTION IN REACTOR FEED, X_1^i
(a)
(b)
(c)
(d)

Figure 1

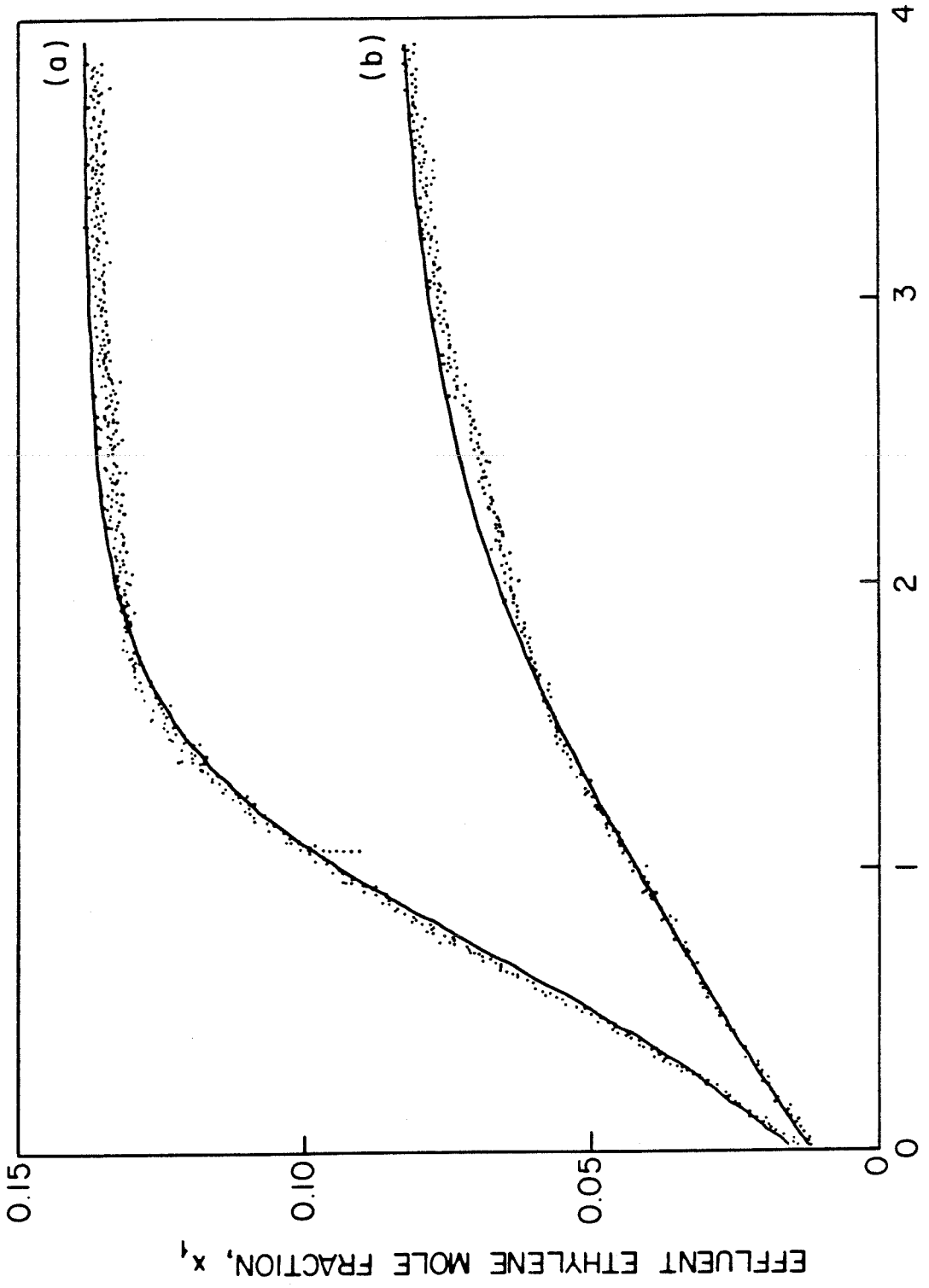
EFFLUENT ETHYLENE MOLE FRACTION, x_1
0.15
0.10
0.05
0
(a)
(b)
0
1
2
3
4
TIME (hrs)

Figure 2

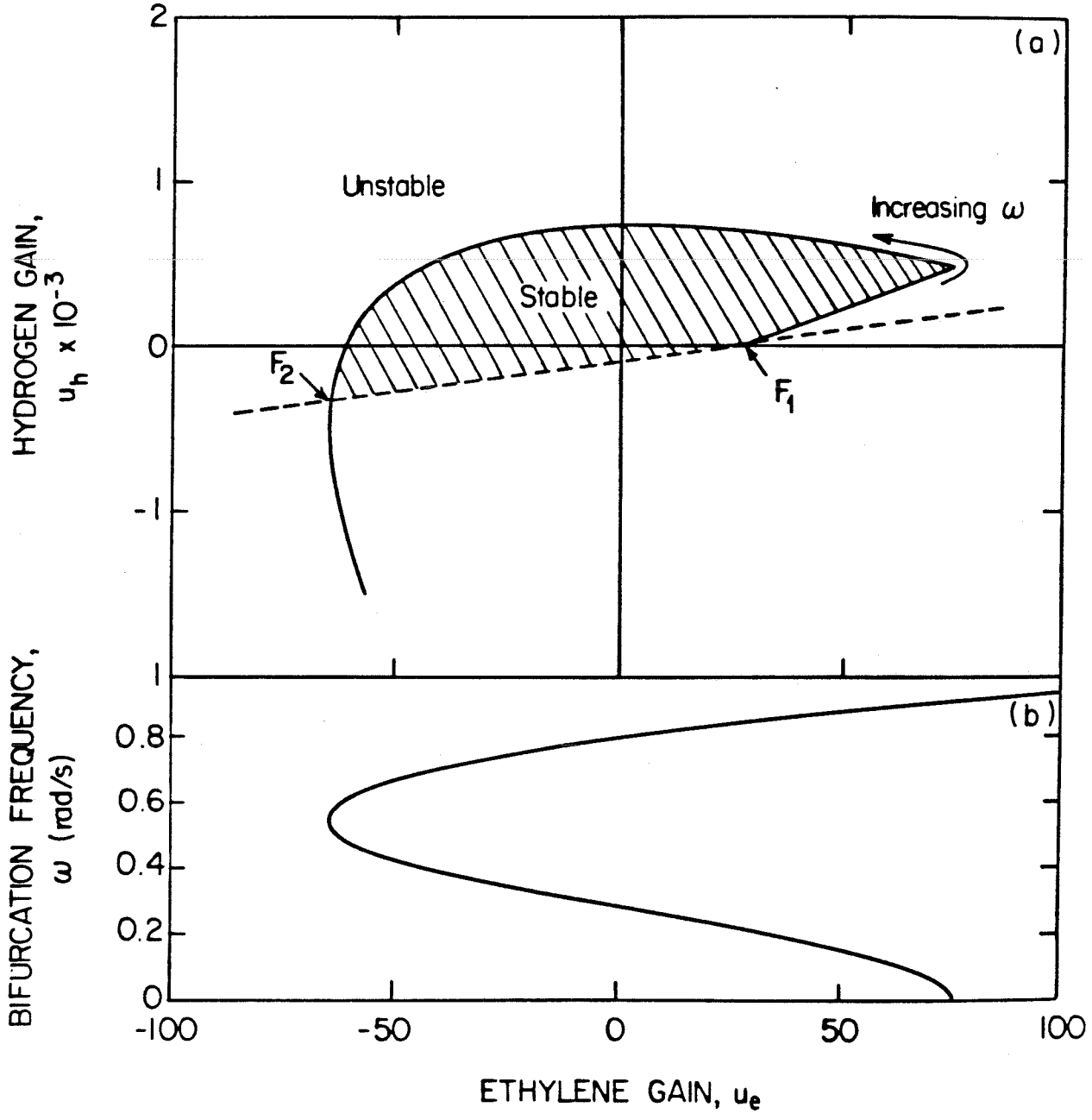
(a)
Unstable
Increasing ω
Stable
F2
F1
HYDROGEN GAIN, uh x 10-3
2
1
0
-1
(b)
BIFURCATION FREQUENCY, ω (rad/s)
0.8
0.6
0.4
0.2
0
-100
-50
0
50
100
ETHYLENE GAIN, ue

Figure 3

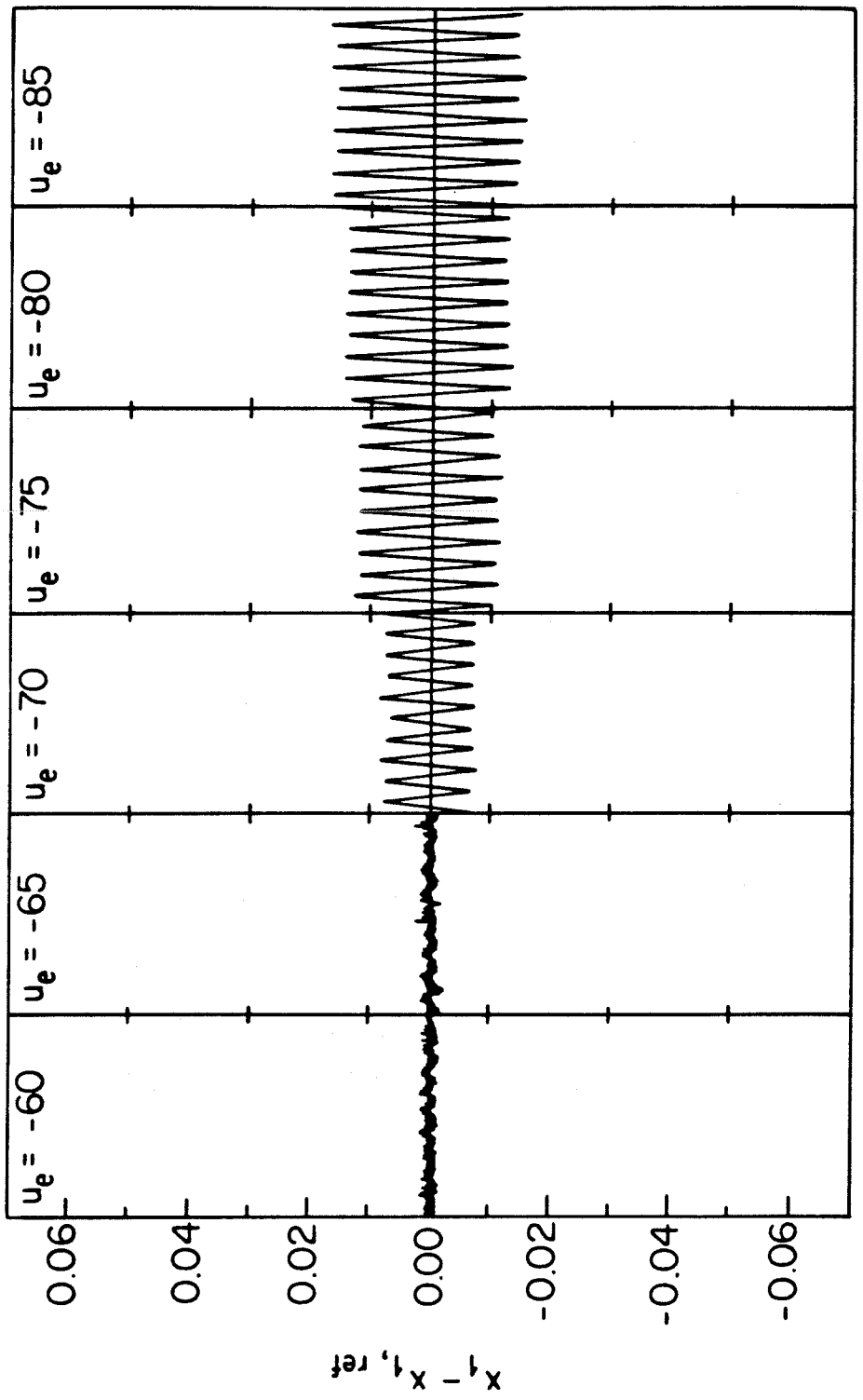
u_e = -60
u_e = -65
u_e = -70
u_e = -75
u_e = -80
u_e = -85
0.06
0.04
0.02
0.00
-0.02
-0.04
-0.06
$x_1 - x_{1,ref}$
90 s
TIME (sec)

Figure 4

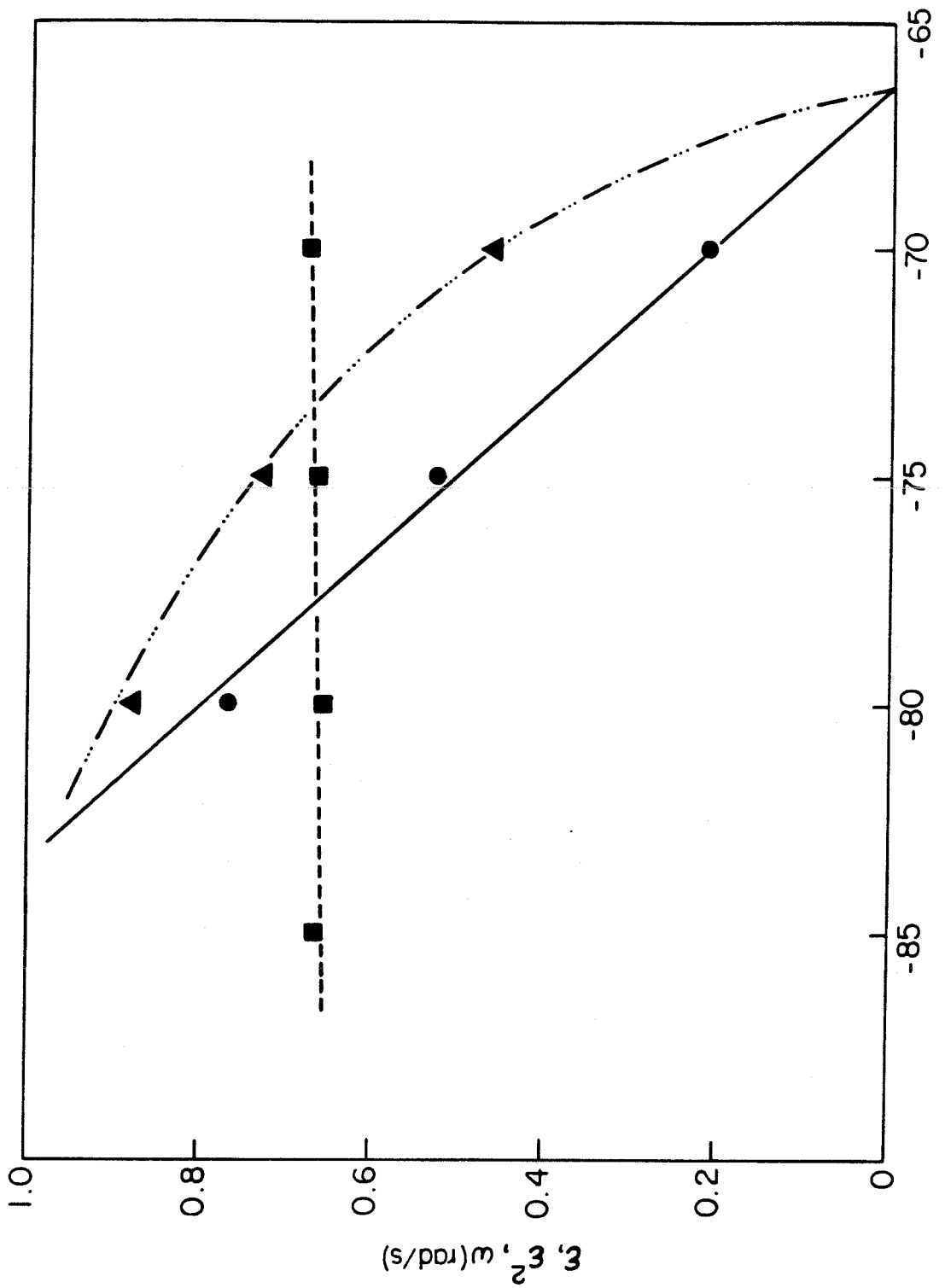

Figure 5

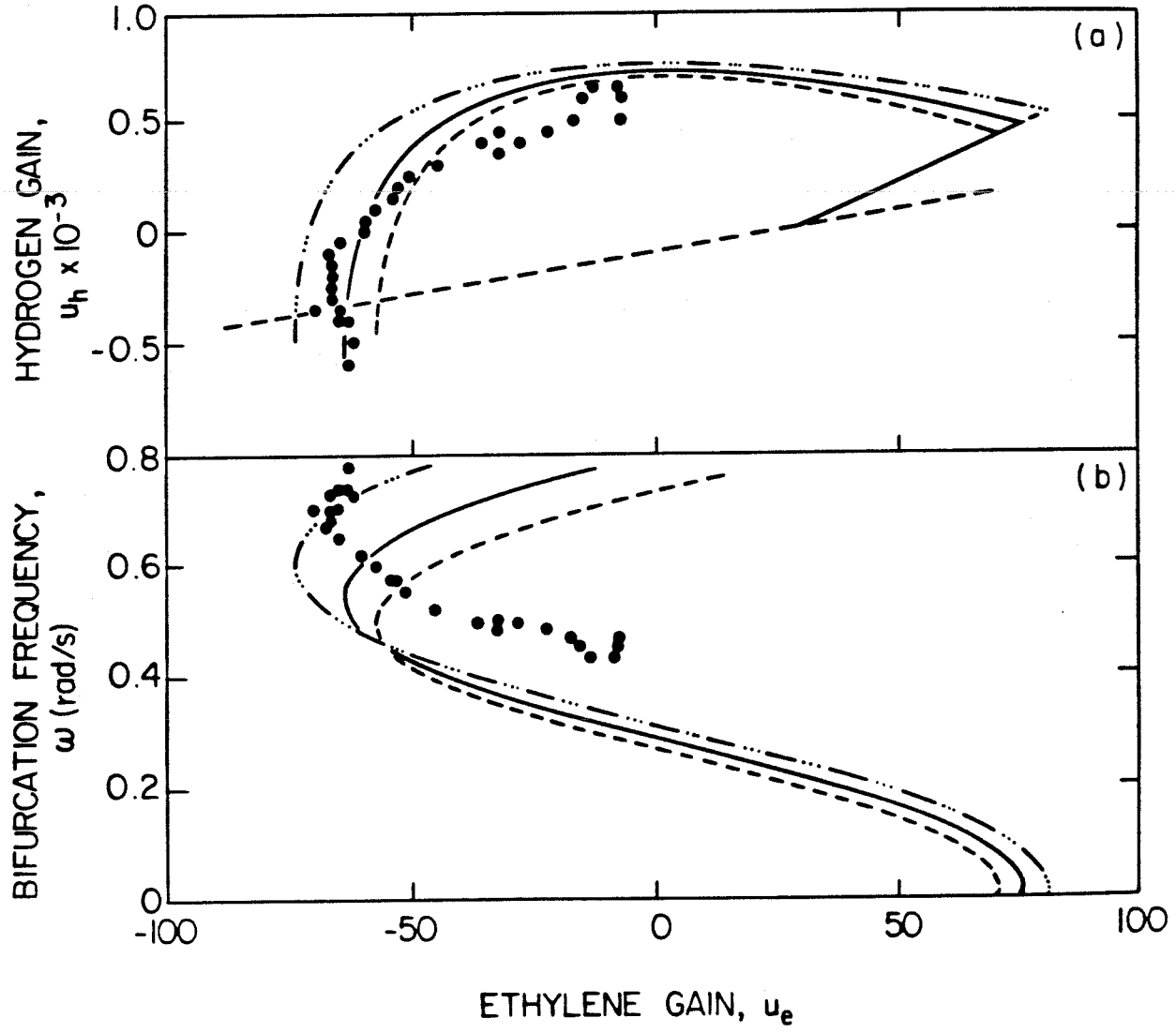
(a)
(b)
HYDROGEN GAIN, $u_h \times 10^{-3}$
BIFURCATION FREQUENCY, ω (rad/s)
ETHYLENE GAIN, u_e
1.0
0.5
0
-0.5
0.8
0.6
0.4
0.2
0
-100
-50
0
50
100

Figure 6

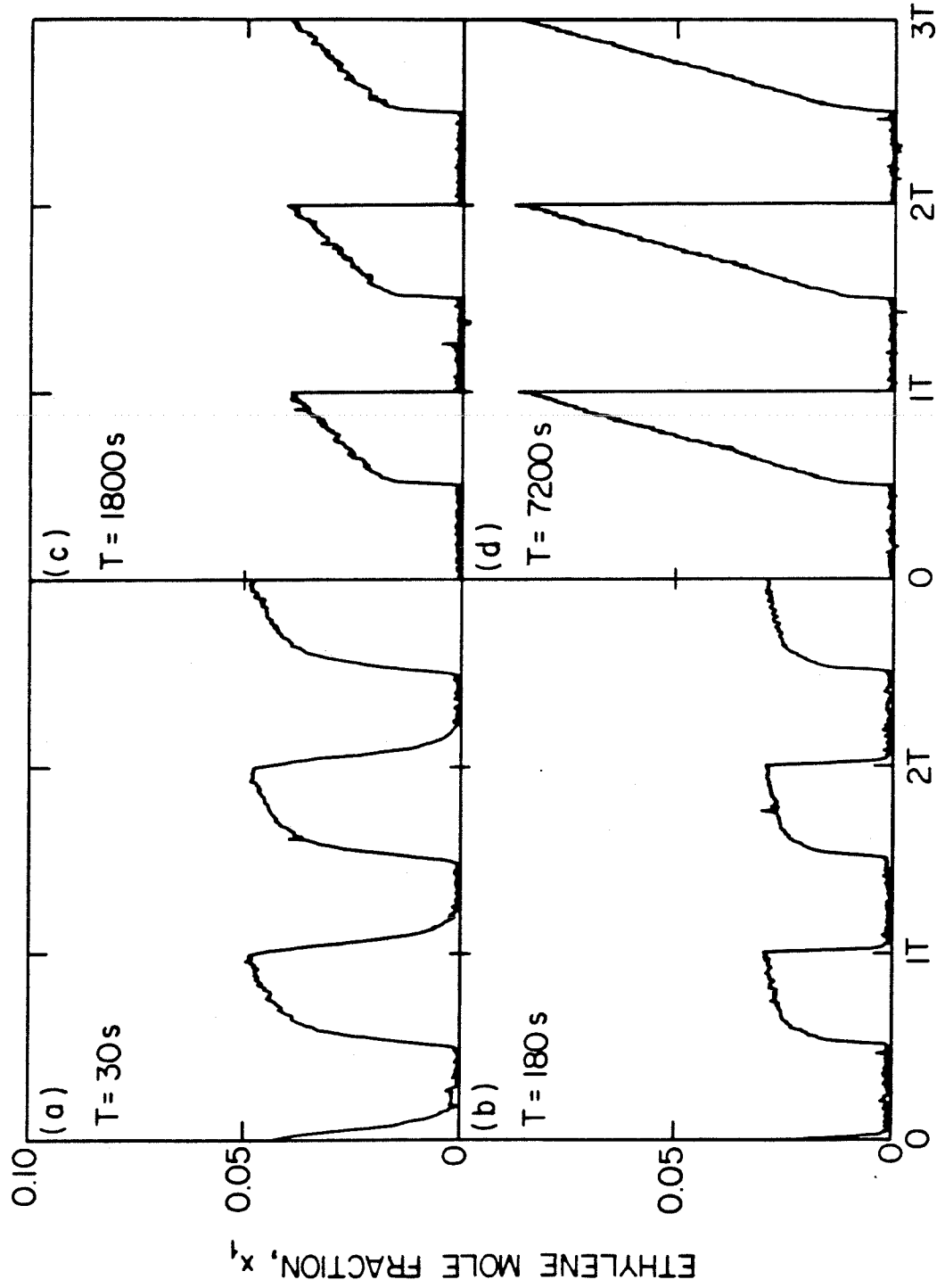
(a)
T = 30 s
(b)
T = 180 s
(c)
T = 1800 s
(d)
T = 7200 s
0.10
0.05
0
0.05
0
1T
2T
0
1T
2T
3T
ETHYLENE MOLE FRACTION, x_1
TIME (sec)

Figure 7

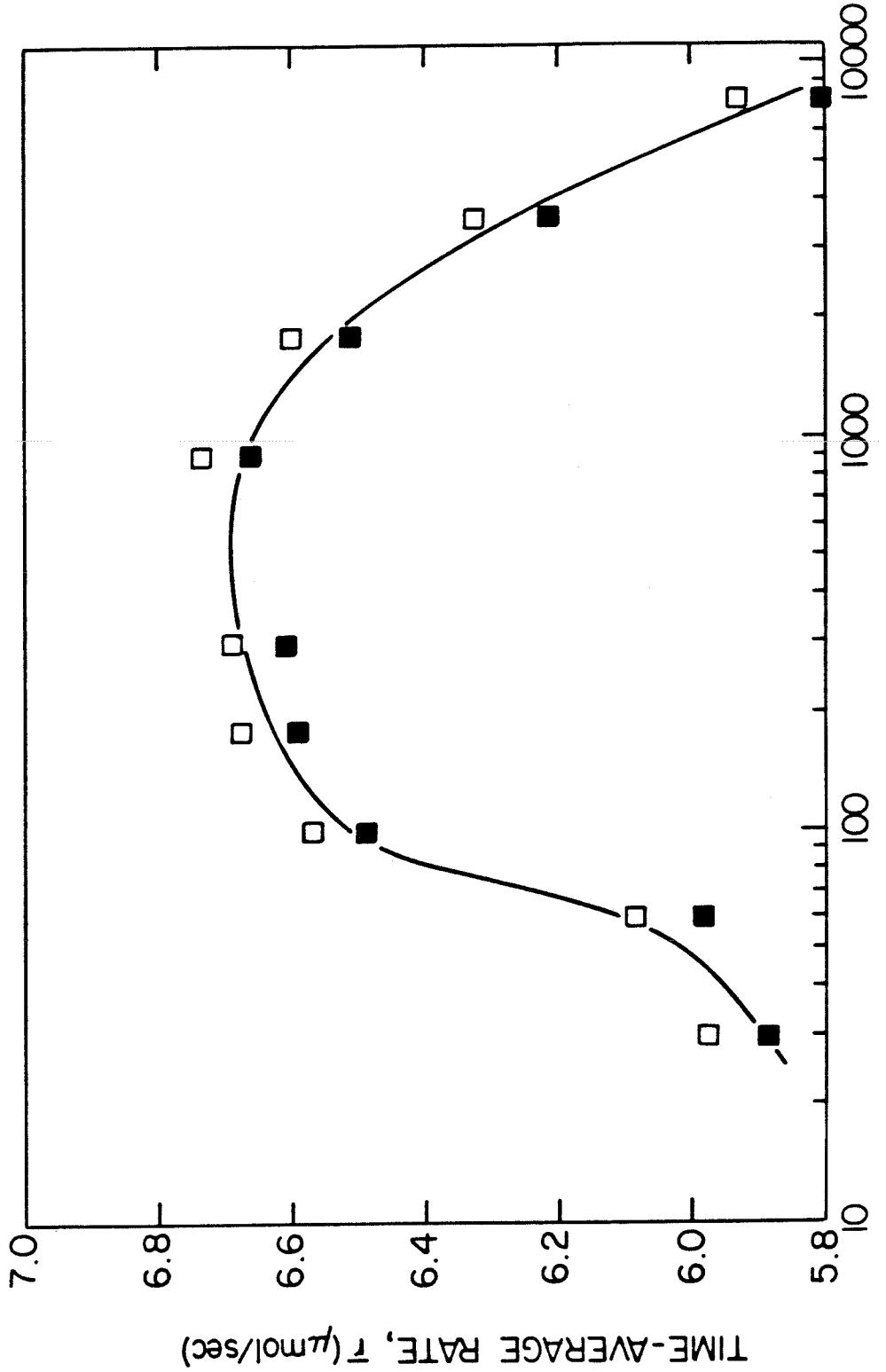
TIME-AVERAGE RATE, $\bar{r}$ (μmol/sec)
7.0
6.8
6.6
6.4
6.2
6.0
5.8
10
100
1000
10000
PERIOD (sec)

Figure 8

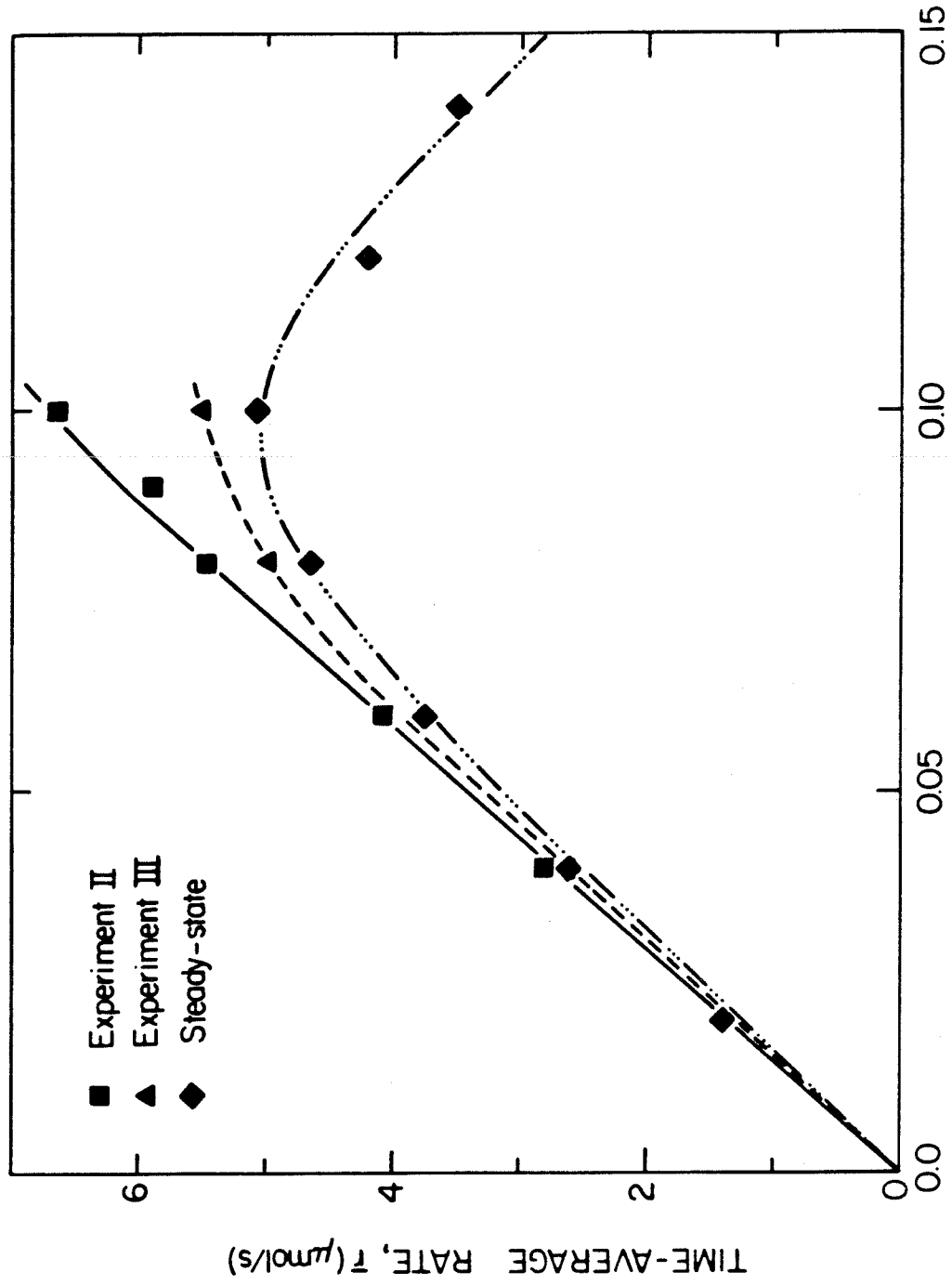
Experiment II
Experiment III
Steady-state
TIME-AVERAGE RATE, r (μmol/s)
AVERAGE ETHYLENE FEED FRACTION, $\bar{x}_1$
0
2
4
6
0.0
0.05
0.10
0.15

Figure 9

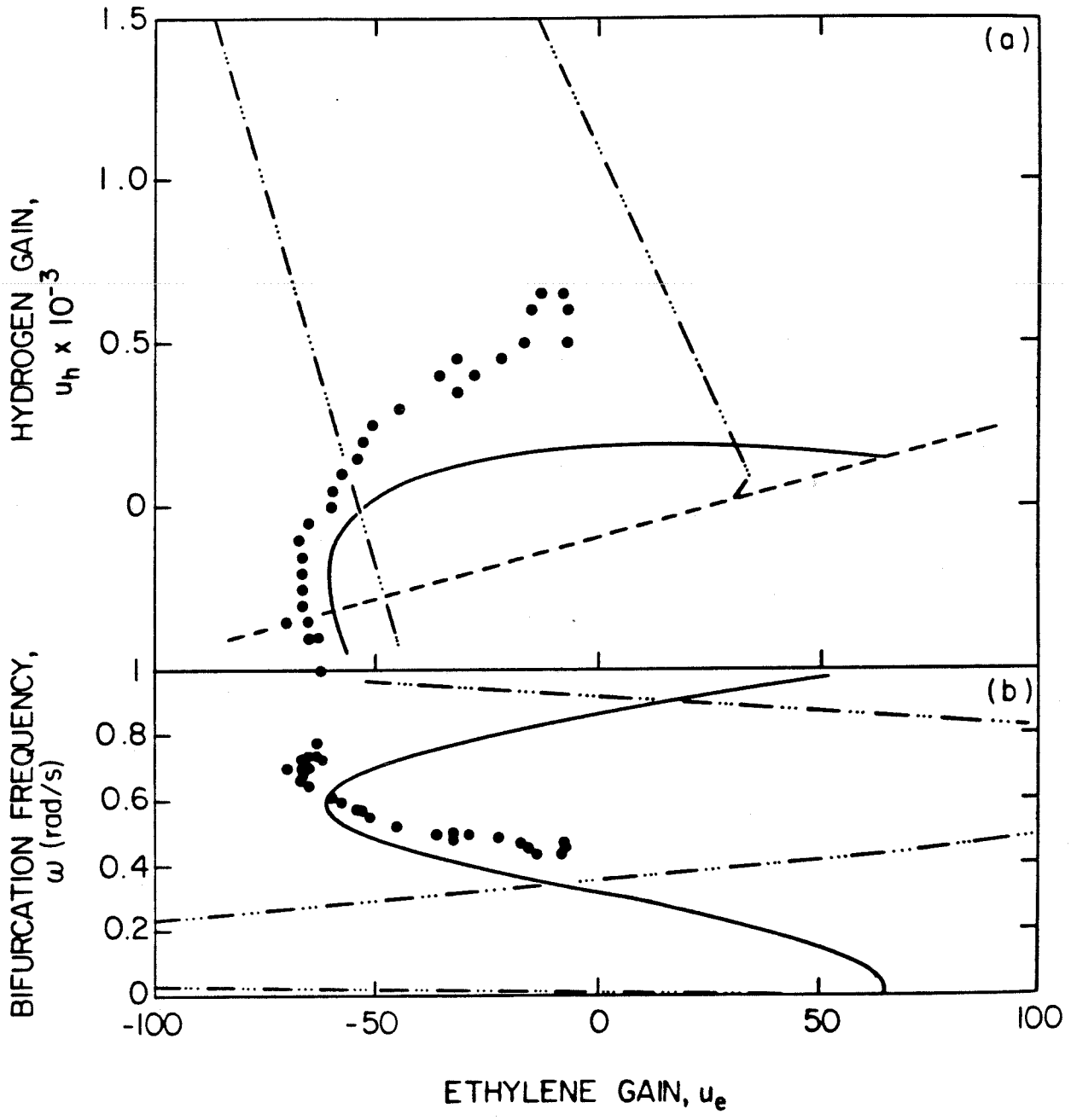
(a)
(b)
HYDROGEN GAIN, $u_h \times 10^{-3}$
BIFURCATION FREQUENCY, ω (rad/s)
ETHYLENE GAIN, u_e
1.5
1.0
0.5
0
1
0.8
0.6
0.4
0.2
0
-100
-50
0
50
100

Figure 10

CHAPTER 4

APPLICATION OF FEEDBACK-INDUCED BIFURCATION FOR EVALUATING STEADY-STATE AND TRANSIENT HETEROGENEOUS CATALYSIS KINETIC MODELS

INTRODUCTION

Feedback-induced bifurcation for nonlinear model identification was first proposed by Kuszta and Bailey (1982) and subsequently analyzed in mathematical detail and applied to catalytic kinetics by Lyberatos, Kuszta and Bailey (1984a, 1984b, 1985). The underlying premise for their work was the opportunity to obtain deeper insight into nonlinear model structure when the system is at, or near, bifurcation. Since many nonlinear catalytic systems are *tame* and do not exhibit bifurcation for any time-invariant inputs, feedback is used to modify the system so that bifurcation can occur.

This paper presents some preliminary experimental studies that are a logical continuation of the theoretical foundation that was established by Kuzsta, Lyberatos, and Bailey. They found through simulation that decrement diagrams which describe the local stability of a chosen stationary point as a function of bifurcation parameters are useful for model discrimination. A typical two-parameter decrement diagram would have two feedback gains as its axes with curves in the plane delimiting regions of steady-state multiplicity, Hopf, and higher-order bifurcations. A different decrement diagram is necessary for each reference steady state under consideration.

In this paper we describe construction of experimental decrement diagrams, the key being the location of boundaries in some parameter space that, when crossed, cause a stable steady state to give rise to multiple steady states or sustained oscillations. Experimental bifurcations to steady-state multiplicity and oscillatory behavior are presented for ethylene hydrogenation on 1 g of 0.5% Pt/Al_2O_3 in a catalytic CSTR to which feed ethylene and hydrogen flow rates were quasi-continuously manipulated as functions of the effluent ethylene concentration. Pitchfork bifurcations to steady-state multiplicity have been experimentally observed as functions of ethylene gain, given several fixed hydrogen gains. These data demonstrate the general result that small discrepencies between the actual and chosen values of the reference steady state can give

rise to imperfect, cusp-like bifurcations. Imperfect, asymmetric steady-state bifurcation branches are shown experimentally to contain discontinuities and hystereses in terms of the effluent ethylene concentration as a function of the ethylene gain parameter.

These bifurcation phenomena are well described by a kinetic model containing one of two sets of parameters; both sets provide adequate approximations to steady-state kinetic data. That is, steady-state bifurcation data were used to discriminate between two rival parameter sets. Examples of Hopf bifurcation to limit cycles are also presented and compared with results for the experimental reactor containing 0.94 g of a different catalyst made up of 0.05% Pt/Al_2O_3. These data, step-response data, and model simulations suggest that the two catalysts, namely 0.5% and 0.05% Pt on alumina, operate in regimes controlled by processes with very different time scales, an observation that lends credence to the hypothesis that ethylene hydrogenation dynamics on the low-loaded catalyst are dominated by the effects of hydrogen spillover. Finally, some general results concerning the usefulness of feedback- induced bifurcation are discussed.

ETHYLENE HYDROGENATION ON Pt/Al_2O_3

Ethylene hydrogenation on Pt/Al_2O_3 has been investigated for many years. There seems to be no general consensus on the overall reaction mechanism (Ibach *et al.*, 1977; Mullins, 1982); however, it is widely held that some ethylene dissociates upon adsorption to form an unreactive hydrogen-deficient adsorbate that does not participate in the formation of ethane. Adsorbed atomic hydrogen reacts with either gaseous ethylene (Eley-Rideal) or a different form of adsorbed ethylene to form a five-hydrogen intermediate that participates in a Langmuir- Hinshelwood reaction with adsorbed atomic hydrogen to produce product ethane (Briggs *et al.*, 1980; Soma, 1979; Thomas and Thomas, 1967). A complication particular to hydrogenation on supported Pt is hydrogen spillover which has been shown to affect static and dynamic properties of the overall reaction (Bianchi *et al.*, 1975; Pajonk *et al.*, 1983).

A reaction mechanism that was originally proposed by Mullins and Saltsburg (Mullins, 1982; Saltsburg and Mullins, 1982) was chosen to model steady-state kinetic data for ethylene hydrogenation on 0.5% Pt/Al_2O_3 at 30 °C and atmospheric pressure. Reaction rates were measured for ethylene and hydrogen feed rates ranging from 4 to 20 sccm in 100 sccm total feed. Ethylene conversion ranged from 15% at a feed of 20% C_2H_4 and 4% H_2 to 97% at a feed containing 10% C_2H_4 and 20% H_2. The data were obtained using the catalytic CSTR which is described in the next section of this paper. The reaction mechanism is:

$$H_2 + 2^* \rightarrow 2H^* \qquad \text{(first-order; } k_1\text{)} \qquad \text{(I)}$$

$$C_2H_4 + 2^* \rightleftharpoons C_2H_3^* + H^* \qquad \text{(K)} \qquad \text{(II)}$$

$$C_2H_4 + H^* \rightleftharpoons C_2H_5^* \qquad \text{(dynamic equilibrium; } K_{eq}\text{)} \qquad \text{(III)}$$

$$C_2H_5^* + H^* \rightarrow C_2H_6 + 2^* \qquad (k_2). \qquad \text{(IV)}$$

Steady-state balances on the adsorbed intermediates yield the equations:

$$k_1 x_{H_2} \theta_v - k_2 K_{eq} x_{C_2H_4} \theta_H^2 = 0 \qquad (1)$$

$$K x_{C_2H_4} \theta_v^2 - \theta_H \theta_{C_2H_3} = 0 \qquad (2)$$

with

$$\theta_v = 1 - \theta_H - \theta_{C_2H_3} - K_{eq} x_{C_2H_4} \theta_H \qquad (3)$$

Dependence on $\theta_{C_2H_5}$ has been eliminated based on the assumption of equilibrium for Reaction (III). This assumption and the irreversibility of the hydrogen adsorption Step (I) have been justified elsewhere (Prairie and Bailey, 1987). Steady-state concentrations of ethylene and hydrogen in the reactor effluent can be calculated as a function of the CSTR inlet concentrations with Eqs. (1-3) and the fluid phase material balances

$$F_T^i(x^i_{C_2H_4} - x_{C_2H_4}) - k_2(1 - x_{C_2H_4})K_{eq}x_{C_2H_4}\theta_H^2 = 0 \quad (4)$$

$$F_T^i(x^i_{H_2} - x_{H_2}) - k_2(1 - x_{H_2})K_{eq}x_{C_2H_4}\theta_H^2 = 0 \quad (5)$$

where superscript i denotes an inlet condition. The terms $(1 - x_{C_2H_4})$ and $(1 - x_{H_2})$ arise from the nonequimolar nature of the reaction stoichiometry. Rapid internal and external mass transport is assumed. The algebraic system of Eqs. (1-5) was solved using the IMSL computer program ZSPOW which utilizes a variation of Newton's method.

This model, with k_1 = 21.2 mmol/min, K = 48.7, K_{eq} = 29.2, and k_2 = 1.56 mmol/min, was used successfully to describe steady-state data for ethylene hydrogenation on 0.05% Pt/Al_2O_3 at 80 °C and atmospheric pressure (Prairie and Bailey, 1987). Theoretically, K and K_{eq} should be independent of catalyst loading; accordingly, the 0.5% Pt/Al_2O_3 data were fit via nonlinear regression to find the two catalyst-dependent rate parameters, k_1 and k_2, while holding the equilibrium coefficients, K and K_{eq}, fixed at the values determined for 0.05% Pt/Al_2O_3 (this comparison neglects temperature dependence of the equilibrium coefficients) (Prairie and Bailey, 1987). A minimum in the sum-of-residual-squares surface was obtained for k_1 = 1.36 mol/min and k_2 = 4.89 mmol/min, yielding a multiple correlation coefficient squared, r^2, of 0.85. These values with K = 48.7 and k_{eq} = 29.2 as above are denoted Parameter Set I. A superior fit (r^2 = 0.92) of the steady-state kinetic data for the 0.5% Pt/Al_2O_3 catalyst resulted when all four parameters were allowed to vary during the minimization procedure. In this case the parameters k_1 = 11.46 mol/min, K = 630.0, K_{eq} = 48.7 and k_2 = 3.43 mmol/min (Parameter Set II) produced a global minimum in the sum-of-squares surface. Discrimination between these two parameter sets, both of which give very good agreement with steady-state kinetic data, is accomplished with steady-state bifurcation data presented later. It is noted that the kinetic data and the model exhibit an intrinsic reaction rate that has a maximum in terms of ethylene pressure and increases monotonically with hydrogen pressure.

FEEDBACK ALGORITHMS

Feedback was implemented by manipulating the ethylene and hydrogen inlet feed fractions as functions of the effluent ethylene concentration, $x_{C_2H_4}$, while maintaining the total feed rate, F_T^i, constant at 100 sccm (1 sccm = 22.4×10^3 mol/min). Ethylene-based feedback algorithms were chosen such that

$$x^i_{C_2H_4} = x^{ref}_{C_2H_4} + \frac{2w}{\pi F_T^i} \mathrm{Tan}^{-1}[u_e(x_{C_2H_4} - x^{ref}_{C_2H_4})] \tag{6}$$

$$x^i_{H_2} = x^{ref}_{H_2} + \frac{2w}{\pi F_T^i} \mathrm{Tan}^{-1}[u_h(x_{C_2H_4} - x^{ref}_{C_2H_4})] \tag{7}$$

where the superscript ref denotes a reference stationary point of the open-loop reactor system; i.e., $(x_{C_2H_4}{}^{ref}, x^{ref}_{H_2})$ is a theoretical steady-state solution to Eqs. (1-5) given specific feed conditions $(x_{C_2H_4}{}^i, x^i_{H_2})$. The ethylene and hydrogen gain parameters are u_e and u_h. The arctangent function was used for the feedback algorithm because it is differentiable and resembles proportional control with saturation.

EXPERIMENTAL

Details of the reactor, data-acquisition and control system (DAC) are presented elsewhere (Smith, 1983). Briefly, the system consists of an ≈11 cm^3 annular, stirred, internal recirculation catalytic reactor that is fed from one of two switched feed lines that contain predetermined levels of helium, ethylene, hydrogen and oxygen(pretreatment only). Automatic or manual switching between the feedstreams is made possible with an HP9825B-based data-acquisition and control system and two low-volume solenoid valves. Feed rates of He, C_2H_4, H_2, and O_2 are regulated with eight Tylan mass flow controllers in the range 0-200 sccm for He and 0-20 sccm for the other feed gases. For most experiments, the total molar feed rate to the reactor was maintained at 100 sccm. Set-points to the mass flow controllers can be manipulated manually from 0-5 V (0

sccm - full scale) with potentiometers or with the DAC system operating with a 20mV output resolution which corresponds to 0.8 sccm for He and 0.08 sccm for C_2H_4, H_2, and O_2. Ethylene concentration in the reactor effluent is continuously monitored in a 0.35 cm^3 flow cell that is part of a Wilkes-Miran I variable filter infrared analyzer operating at 10.4 μm. Ethylene concentration is related to IR absorbance via the empirical relationship $x_{C_2H_4} = 1.3(e^{0.176A} - 1)$, $0 \leq x_{C_2H_4} < 20\%$, where A is a measure of absorbance ranging from 0 to 1 V. The IR analyzer is interfaced with a strip-chart recorder and the DAC system for continuous analog and digital records of the effluent ethylene concentration. The digital resolution of the D/A convertor is 500 μV, producing 0.238% uncertainty in $x_{C_2H_4}$ measurements at $x_{C_2H_4} = 0.05$ and 0.085% uncertainty at $x_{C_2H_4} = 0.15$.

Closed-loop operation is implemented by using the computer to calculate set-points (i.e., $x^{ref}_{C_2H_4}$ and $x^{ref}_{H_2}$) for the mass flow controllers per the control algorithms (6) and (7) based upon simultaneous IR absorbance measurements of $x_{C_2H_4}$. Data acquisition and control are performed at 4 Hz during closed-loop operation.

Proper modeling of the feedback-induced bifurcations requires that mass flow controller set-point manipulations be smooth functions of the measured variable. Preliminary experiments indicated a resolution problem caused by the 10-bit (20mV stepsize) D/A convertors that resulted in imperfect steady-state bifurcations (imperfect steady-state bifurcation is described in detail in the next section). The resolution problem was eliminated with a simple two-channel amplifier and four extra D/A convertors as follows:

1. The desired output voltage is truncated within the real-time DAC subroutine to its nearest multiple of 20mV, and the result is programmed into a D/A channel.

2. Meanwhile, the desired voltage less the truncated value is multiplied by 2000 and programmed into another D/A channel.

3. Then, in a separate amplifier circuit, the difference voltage is attenuated by 2000 and added to the truncated voltage.

In this way it is possible to use 8 D/A channels to program four mass flow controllers with a resolution of 10μV.

Step experiments were performed to evaluate the mixing and open-loop dynamic characteristics of the reactor- IR analyzer combination. At 100 sccm, room temperature and pressure, a step from pure He to 10% C_2H_4 in He produced an ethylene concentration trajectory that was well explained by a simple ideal CSTR equation with a time constant of 4 s. The step experiment also demonstrated a 3.2 s transport lag between the solenoid switching valves and the IR flow cell. It is very important to include time-delay in a closed-loop dynamic model for the system because it can have a profound affect on Hopf bifurcation behavior.

The open-loop dynamic response of the mass flow controllers to changes in set-points were characterized by a Bode analysis. Sinusoidal forcing of the ethylene and hydrogen set-points over the frequency range $0.0 \leq \omega \leq 2.0$ rad/s provided data for empirical transfer functions, written in the frequency domain

$$G(\omega) = AR(\omega)\exp(i\,\phi(\omega)) \tag{8}$$

where ω is the forcing frequency, $AR(\omega)$ is the amplitude ratio and $\phi(\omega)$ is the phase shift in radians. Experiments at typical operating and cylinder pressures yielded

$$G_{C_2H_4}(\omega) = \frac{1}{\sqrt{(0.221\omega)^2 + 1}}\, e^{-0.427\omega i} \tag{9}$$

$$G_{H_2}(\omega) = \frac{1}{\sqrt{(1.07\omega)^2 + 1}}\, e^{-(\mathrm{Tan}^{-1}(1.07\omega) + 0.135\omega)i} \tag{10}$$

These transfer functions are necessary for a complete description of the experimental system.

The catalyst used in these experiments was 0.5% Pt on Al_2O_3 supplied by Engelhard in the form of $\frac{1}{8}$ inch cylindrical pellets. A typical reactor loading is 1 g of ≈40 half-cylinders. After initial pretreatment in 10% O_2 at 300 °C for 1 hr followed by 1 hr in 10% H_2 at 300 °C, the catalyst retained constant activity and further retreatment was unnecessary. All experiments on the 0.5% Pt/Al_2O_3 catalyst were performed at 30 °C and atmospheric pressure unless otherwise noted.

STEADY-STATE BIFURCATION

Bifurcation to multiple steady states occurs when a real eigenvalue of the linear part of the system crosses the imaginary axis to become a positive real eigenvalue that is greater than the real parts of the rest of the eigenvalues in the spectrum. Notationally, a condition for steady-state bifurcation can be written

$$p(0) = 0; \quad \mathrm{Re}(\lambda) < 0, \forall \lambda \ni p(\lambda) = 0 \tag{11}$$

where $p(\lambda)$ denotes the characteristic equation for the linearized system ($p(\lambda) = \det(J - \lambda I)$ for the open-loop case and is the denominator of the overall transfer function for the closed-loop system; here J is the Jacobian matrix of the nonlinear system about a reference stationary point.)

Consider the case of a simple stirred tank (the experimental reactor without reaction) with one feedback on the ethylene flow rate that is based on the effluent ethylene concentration. Note that in contrast to the reactor supporting reaction, the stirred tank with ethylene-based feedback to the hydrogen controller would not affect the ethylene concentration in the tank if the total molar flow rate is always held constant. The differential equation for the ethylene concentration in the tank is

$$\tau\frac{d}{dt}\hat{x}_{C_2H_4} \equiv N(\hat{x}) = \frac{2w}{\pi F_T^i}\mathrm{Tan}^{-1}(u_e\hat{x}_{C_2H_4}) - \hat{x}_{C_2H_4} \tag{12}$$

where $\hat{x}_{C_2H_4}$ is the deviation variable $x_{C_2H_4} - x^{ref}_{C_2H_4}$. Then, the condition on $N(\hat{x})$ for steady-state bifurcation is

$$\left.\frac{\partial N(\hat{x})}{\partial \hat{x}}\right|_{\hat{x}=0} = 0 \tag{13}$$

which yields

$$u_e^{ss} = \frac{\pi F_T^i}{2w} \tag{14}$$

for the steady-state bifurcation gain (meaning there are three steady states if $u_e > u_e^{ss}$). Ideally, the bifurcation branches would fit the equation

$$u_e(\hat{x}) = \frac{1}{\hat{x}}\tan\left[\frac{\pi\hat{x}F_T^i}{2w}\right]. \tag{15}$$

However, it is not always possible to measure $x^{ref}_{C_2H_4}$ with sufficient accuracy and when the experimental reference steady state is not exactly equal to a real stationary point of the system, imperfect steady-state bifurcation results.

Imperfect bifurcation can be understood by imagining the chosen value of $x^{ref}_{C_2H_4}$ to be equal to the real value plus some small perturbation δ. When $\delta \neq 0$, the removable singularity at the origin in Eq. (15) becomes an isolated singularity which drastically alters the shape of the bifurcation diagram. Figure 1a presents data and simulations for the reactor without reaction operating at a theoretical steady state of $x_{C_2H_4} = 0.054$ for $F_T^i = 50$ sccm, and $w = 2.3$ sccm. The solid curve describes perfect steady-state bifurcation. The dashed curve in Fig. 1a results when the chosen value of $x^{ref}_{C_2H_4}$ is 0.050. The mirror image of the dashed curve results when $x^{ref}_{C_2H_4} = 0.058$. Many adjustments of the experimental value for $x^{ref}_{C_2H_4}$ were necessary in order to

obtain the near perfect experimental bifurcation; slight imperfections in the IR calibration along with IR drift were the sources of the problem. Imperfect steady-state bifurcation data are presented later for the stirred tank containing catalyst. In all cases, for sufficiently large gain, there are three steady states; the two external branches are stable and the one on or near the axis is unstable.

It is apparent from Fig. 1a that imperfect steady-state bifurcation can produce a discontinuity in $\hat{x}(u_e)$. Imagine the system to be operating on the lower branch of the dashed curve. If u_e is decreased to some value below u_e^c, the state of the system will jump to the upper branch thus making the lower branch unobtainable (even for $u_e > u_e^c$) without the introduction of a sizable perturbation. Our example of imperfect bifurcation is somewhat artificial since it describes the unstable behavior of a control system which ideally should be designed with gains far away from points of instability. The example is instructive, however, because it describes a general type of bifurcation phenomena that occurs naturally for certain problems, an example being the deformation of a disk under radial compression experiencing a uniform pressure normal to one of its sides.

It was impossible to obtain perfect steady-state bifurcation for the reactor with reaction. Figure 1b presents experimental data and modeling results for the reactor operating at a hydrogen gain of 150 (F_T^i = 100 sccm, w = 5 sccm, $x^i_{C_2H_4} = 0.15$, $x^i_{H_2} = 0.10$ and $x^{ref}_{C_2H_4} = 0.0537$). The solid curve results from model calculations based on Parameter Set I. The dashed curve was calculated using Parameter Set II. Clearly, this latter parameter set gives rise to some anomalous behavior (multiple hystereses) that was not observed experimentally. Thus, although the 0.05% Pt/Al_2O_3 parameters (Set I) yield a slightly inferior fit to steady-state rate data, they provide vastly superior agreement than does Parameter Set II under the test of steady-state bifurcation. Hence we conclude that the 0.05% Pt/Al_2O_3 equilibrium parameters and associated rate

coefficients should be used for any further model simulations.

Figures 1c and 1d present two examples of steady-state bifurcation for hydrogen gains of 0 and -150, respectively. They demonstrate complex, asymmetric, cusp-like pitchfork bifurcations; they are cusp-like because a plot of the turning point (u_e^c) versus the perturbation parameter δ would look like an asymmetric cusp (symmetric for the case without reaction). As before, the solid curves are model calculations (using Parameter Set I), which are in excellent agreement with the experimental data.

HOPF BIFURCATION

Feedback-induced Hopf bifurcation occurs when feedback gains are manipulated to force a leading eigenvalue pair of the linearized system to cross the imaginary axis and become a complex pair of eigenvalues with a real part that is greater than the real parts of the rest of the eigenvalues in the spectrum. At bifurcation, the eigenvalue pair resides on the imaginary axis so a theoretical condition for Hopf bifurcation is $p(i\omega) = 0$, where as before, $p(\lambda)$ represents the characteristic equation for the linearized model. Thus, algebraic expressions can be derived from the closed-loop system model that define equations for stability boundaries and oscillation frequencies at bifurcation (experimentally observable) in terms of feedback gains and system parameters. These expressions and experimental data can be used to compare rival models and determine parameters that might be inaccessible to steady-state or open-loop transient experiments. A particular advantage of closed-loop dynamic experiments is the counterintuitive result that information about fast processes becomes accessible even if there are other slower time scales that govern the system's open-loop behavior (Kuszta and Sinha, 1980).

Transport lag plays an important role in feedback-induced bifurcation. This fact was used to advantage for verifying the transfer function model of the reactor-IR analyzer-delay-mass flow

controller system without reaction. Time-delay and ethylene feedback gain were manipulated to identify experimentally a Hopf stability diagram that was favorably compared to a mathematical model for the closed-loop system (Prairie *et al.*, submitted). The system model includes CSTR dynamics, transport lag, and transfer functions for the mass flow controllers that were mentioned earlier.

The reactor containing 1 g of 0.5% Pt/Al_2O_3 (30 °C, 1 atm) was augmented by feedback in order to induce closed-loop nonlinear oscillations to demonstrate the type and quality of Hopf bifurcation data that is obtainable with the experimental system. The transition from steady state to oscillations was observed as a function of ethylene feedback gain u_e for three hydrogen gains u_h, 150, 0 and -150. A reference stationary point, $x^{ref}_{C_2H_4} = 0.0568$, was determined for a 100 sccm feed containing 15 sccm of ethylene and 10 sccm of hydrogen. Figure 2 shows how the system responded to changes in ethylene gain at each of the three hydrogen gains; in each case, the width, w, of both of the arctan forcing functions was 5 sccm. Actual bifurcation points can be estimated by extrapolating experimental data for the amplitude-squared versus feedback gain, based on the theoretical result that, to first order, a Hopf bifurcation parameter varies as the square of the resultant amplitude (Heinemann and Poore, 1981). Figure 3 presents such plots; they indicate 92, -52.7, and -160.5 as the Hopf bifurcation ethylene gains corresponding to the hydrogen gains of 150, 0, and -150, respectively.

The three experimental Hopf bifurcation point pairs, (u_e, u_h), are three points in a two-parameter decrement diagram for ethylene hydrogenation on 0.5% Pt/Al_2O_3 in the experimental CSTR operating at 30 °C, ambient pressure, and 100 sccm total feed flow. In a separate study, the authors generated many points in the decrement diagram for ethylene hydrogenation over 0.05% Pt/Al_2O_3 in the same reactor operating at 80 °C, ambient pressure and 100 sccm (Prairie and Bailey, 1987). For comparison, the 0.05% Pt/Al_2O_3 system underwent Hopf bifurcation at

the ethylene gains of -54, -60, and -66.5 when the hydrogen gain was fixed at 150, 0, and -150, respectively. Also, this system bifurcated to consistently higher oscillation frequencies when 0.05% Pt/Al_2O_3 was the catalyst. Some implications are discussed in the next section.

OPEN-LOOP DYNAMICS

Step-response experiments were performed to investigate the open-loop dynamics of the reactor containing 0.5% Pt/Al_2O_3. Figure 4 shows the ethylene effluent response to step-changes in the feed composition: 10% H_2 in He was switched to 20% C_2H_4 and 10% H_2 in He for case a, and 18% H_2 in He was switched to 18% C_2H_4 and 18% H_2 in He for case b. In both cases, the system came to steady state within 20 minutes. This is in marked contrast to similar step experiments over 0.05% Pt/Al_2O_3 that required more than six hours to achieve steady state (Prairie and Bailey, 1987).

Assuming the validity of the elementary Steps I-IV, the open-loop dynamic behavior can be analyzed in terms of two surface time constants in addition to the average residence time for the reactor. Nondimensionalization of the dynamic equations for the two fluid species and the two surface species results in one surface time constant for hydrogen adsorption (Step I), $\tau_{s1} = \frac{N_T}{F_T^i}$, and another for the catalyst poisoning reaction (Step II), $\tau_{s2} = \frac{N_T}{k'}$, where N_T is the total moles of adsorption sites and k' is the forward rate constant in Step II. A theoretical upper bound for τ_{s1} can be obtained by assuming all the Pt in the catalyst to be surface Pt. Accordingly, 1 g of 0.5% Pt/Al_2O_3 should result in a value for τ_{s1} which is no greater than 0.34 s. Similarly, 0.94g of 0.05% Pt/Al_2O_3 will have a τ_{s1} value of 0.032 s as a maximum. $F_T^i = 100$ sccm was used for both of these calculations.

Calculations using a transfer function model of the overall closed-loop (the details of which are left out for brevity, c.f., (Prairie and Bailey, 1987)) and a step-response simulator program

indicate that the values of τ_{s1} = 0.25 s and τ_{s2} = 4 s provide adequate approximations of both the Hopf-bifurcation and the step-response data for the reactor containing 0.5% Pt/Al_2O_3. This result differs markedly from findings for the 0.05% Pt/Al_2O_3 catalyst.

Contradictory results for the magnitude of τ_{s1} were obtained depending on the type of experiment that was performed on the reactor containing 0.05% Pt/Al_2O_3 (Prairie and Bailey, 1987). Reasonable agreement between the model and Hopf bifurcation data required $\tau_{s1} \simeq 1$ s while the slow step transients required τ_{s1} = 5000 s for a good fit. This contradiction plus some cycled feedstream results suggest that the proposed model is incomplete for describing ethylene hydrogenation on 0.05% Pt/Al_2O_3; however, it seems to be an adequate description of the reaction on 0.5% Pt/Al_2O_3. The observation of $\tau_{s1} >> \tau_{s1}^{max}$ suggests a very large reservoir for surface hydrogen. Hence it is likely that hydrogen spillover from the Pt crystallites onto the alumina support plays an important role in the reaction dynamics on the low-loaded catalyst. If this hypothesis is correct, it is reasonable that the effects of hydrogen spillover on the higher-loaded catalyst went unnoticed because of the masking effect of high conversion on the Pt crystallites. If hydrogen spillover or some other support interaction is important, we cannot expect the proposed reaction mechanism to be valid; theoretically, the model describes ethylene hydrogenation on Pt metal.

CONCLUSIONS

The application of feedback-induced bifurcation experiments for catalytic model evaluation has been presented. Complex experimental pitchfork bifurcations to steady-state multiplicity exhibit discontinuities and hystereses due to imperfect choices for the reference stationary point. Steady-state bifurcation data were used to discriminate between two rival parameter sets for ethylene hydrogenation over 0.5% Pt/Al_2O_3 at 30 °C and atmospheric pressure. Also, feedback-induced steady-state bifurcation experiments provide an efficient method for acquiring steady-

state reaction rate data over a wide range of gas-phase compositions. Hopf bifurcation and step-response experiments were described for this same reaction and compared with similar data for ethylene hydrogen over 0.05% Pt/Al_2O_3. A reaction mechanism proposed by Mullins and Saltsburg adequately describes steady-state and transient behavior (bifurcation and open-loop) for the reaction on 0.5% Pt/Al_2O_3. However, this model is incomplete for describing the dynamic behavior of the low-loaded catalyst.

NOTATION

A	IR absorbance, V
AR(ω)	amplitude ratio
F_T^i	total molar feedrate, sccm
G(ω)	transfer function in frequency domain
i	$\sqrt{-1}$
K, K_{eq}	equilibrium coefficients
k_i	rate coefficients, mol/min
N_T	total number of active sites, mol
p(λ)	characteristic equation
u	feedback gain (bifurcation parameter)
w	width of feedback function, sccm
x	vector of states
x	mole fraction
epsilon	oscillation amplitude
θ_i	fractional coverage
λ	vector of system parameters
λ	eigenvalue
τ	average residence time, s
τ_{s1}, τ_{s2}	surface time constants, s
φ(ω)	phase angle, rad
ω	frequency, rad/s

subscripts and superscripts

c	critical (fold-point)
e	ethylene
h	hydrogen
i	inlet condition
max	theoretical upper bound
o	initial condition
ref	reference condition (stationary point)
ss	steady-state bifurcation
v	vacant site

REFERENCES

Bianchi, D., G.E.E. Gardes, G.M. Pajonk, and S.J. Teichner (1975). Hydrogenation of ethylene on alumina after hydrogen spillover. *J. Catal.* **38,** 135-146.

Briggs, D.J., A.G. Dewing, R.B. Burden, R.B. Mayes, and P.B. Wells (1980). Support effects in ethane hydrogenation catalyzed by platinum. *J. Catal.* **65,** 31-35.

Heinemann, R. F., and A. B. Poore (1981). Multiplicity, stability, and oscillatory dynamics of the tubular reactor. *Chem. Engng. Sci.* **36,** 1411-1419.

Ibach, H., H. Hopster, and B. Sexton (1977). Analysis of surface reactions by spectroscopy of surface vibrations. *Surface Sci.* **1,** 1-24.

Kuszta, B., and J. E.Bailey (1982). Nonlinear model identification by analysis of feedback-stimulated bifurcation. *IEEE Trans. Autom. Control* **AC-27,** 227-228.

Kuszta, B., and N.K. Sinha (1980). On identification of linear systems with feedback: high gain feedback case. *Int. J. Systems Sci.* **11,** 403-409.

Lyberatos, G., B. Kuszta, and J.E. Bailey (1984a). Discrimination and identification of dynamic catalytic models via introduction of feedback. *Chem. Engng. Sci.* **39,** 739-750.

Lyberatos, G., B. Kuszta, and J.E. Bailey (1984b). Steady-state multiplicity and bifurcation analysis via the Newton-polyhedron approach. *Chem. Engng. Sci.* **40,** 947-960.

Lyberatos, G., B. Kuszta, and J.E. Bailey (1985). Normal forms for chemical reaction systems via the Affine trransformation. *Chem. Engng. Sci.* **40,** 199-208.

Mullins, M. E. (1982). Hydrocarbon reactions over transition metals: observation of surface hydrogen. Doctoral dissertation, University of Rochester.

Pajonk, G.M., S.J. Teichner, and J.E. Germain, Eds., (1983). *Spillover of adsorbed species,* Elsevier: Amsterdam.

Prairie, M.R, and J. E. Bailey (1987). Experimental and modeling investigation of steady-state and dynamic characteristics of ethylene hydrogenation on Pt/Al_2O_3. To appear in *Chem. Engng. Sci.*

Prairie, M. R, B.H. Shanks and J. E. Bailey . Intentional Manipulation of closed-loop time delay for model validation using feedback-induced bifurcation. Submitted.

Saltsburg, H., and M.E. Mullins (1982). Surface hydrogen in heterogeneous catalysis. *Ann. New York Acad. Sci.* 82-96.

Smith, C. B. (1983). Dynamic modelling and optimization of lumped chemical processes. Doctoral dissertation, University of Houston.

Soma, Y. (1979). Infrared spectra of ethylene adsorbed on transition metals at low temperature and hydrogenation of adsorbed species. *J. Catal.* **59,** 239-247.

Thomas, J.M., and W.J. Thomas (1967). *Introduction to the principles of heterogeneous catalysis.* Academic Press: London.

FIGURE CAPTIONS

1. (a) Perfect and imperfect steady-state bifurcation for the stirred tank without reaction. (b) Steady-state bifurcation for the reactor with reaction at $u_h = 150$; solid curve is for Parameter Set I, dashed curve is for Parameter Set II. (c) $u_h = 0$. (d) $u_h = -150$. $x^{ref}_{C_2H_4} = 0.0537$. Arrows indicate direction of data acquisition.
2. Closed-loop response near Hopf bifurcation. (a) $u_h = 150$. (b) $u_h = 0$. (c) $u_h = -150$. $x^{ref}_{C_2H_4} = 0.0568$.
3. Extrapolations of amplitudes, ε, from Fig. 2 to estimate Hopf bifurcation ethylene gains. (a) $u_h = 150$. (b) $u_h = 0$. (c) $u_h = -150$.
4. Step response trajectories: (a) 10% H_2 in He switched to 20% C_2H_4 and 10% H_2 in He, and (b) 18% H_2 in He switched to 18% C_2H_4 and 18% H_2 in He. Dashed lines indicate model calculations for $\tau_{s1} = 2.5$ s, and $\tau_{s2} = 4$ s.

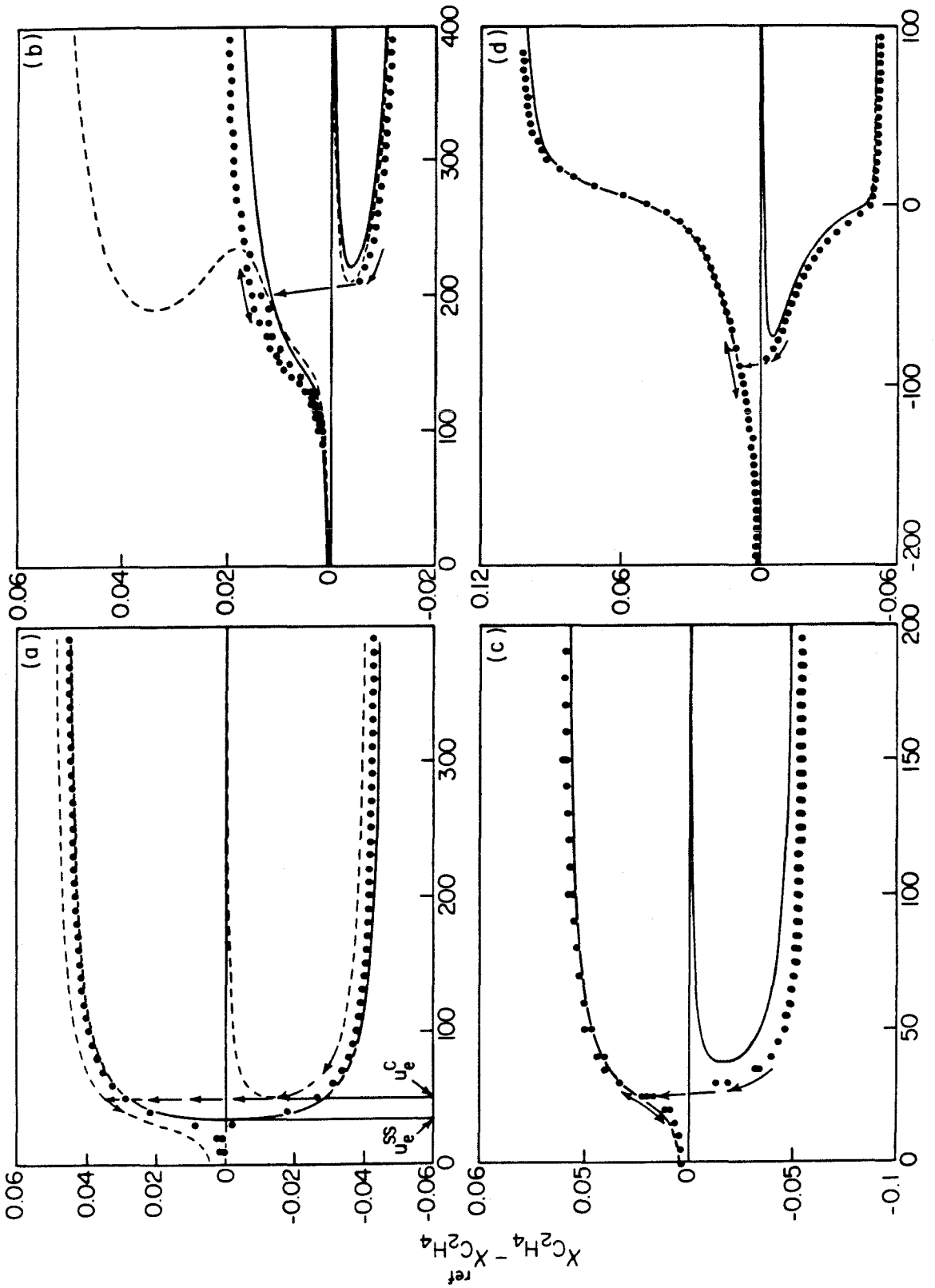

Figure 1

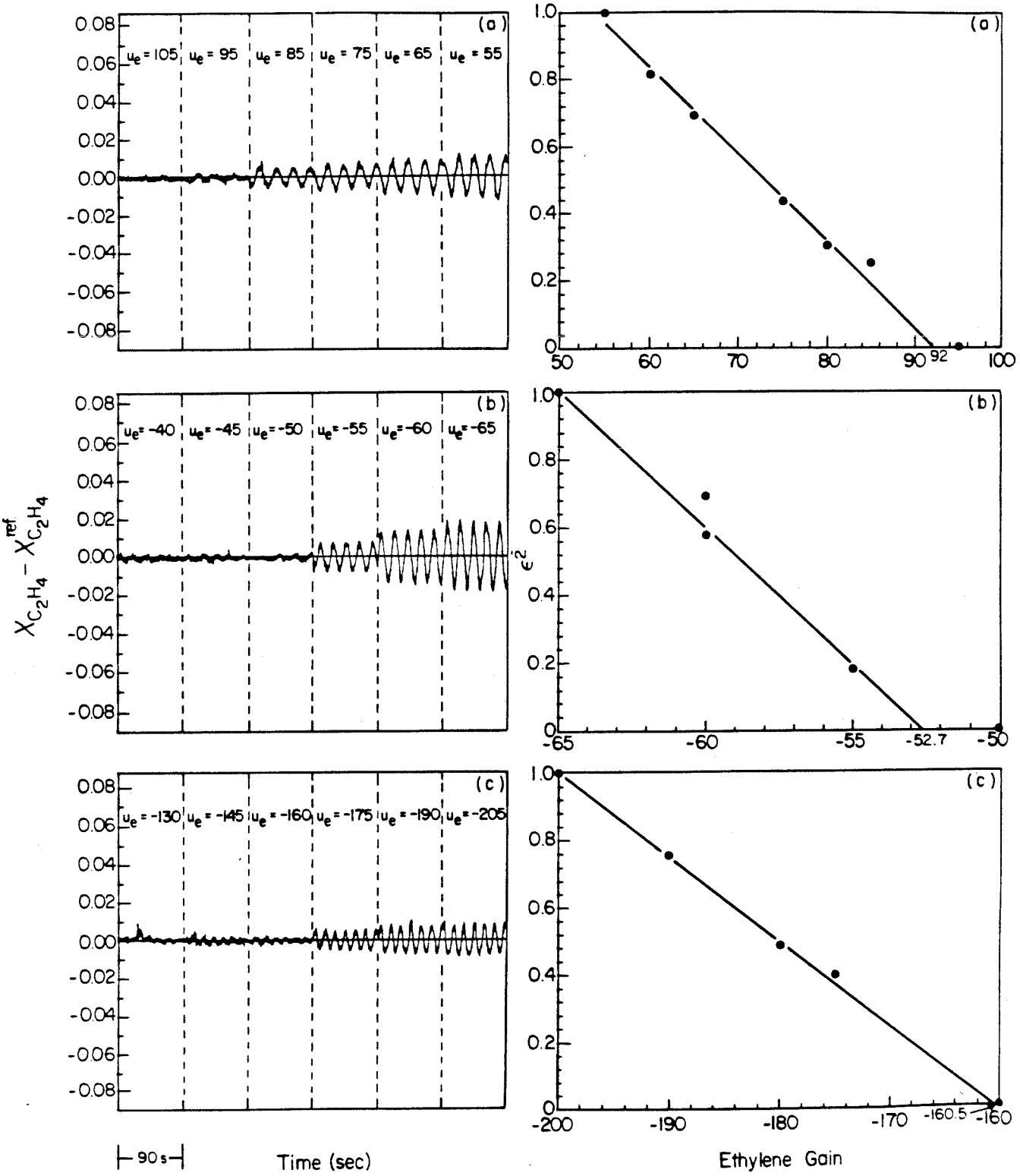

Figure 2

Figure 3

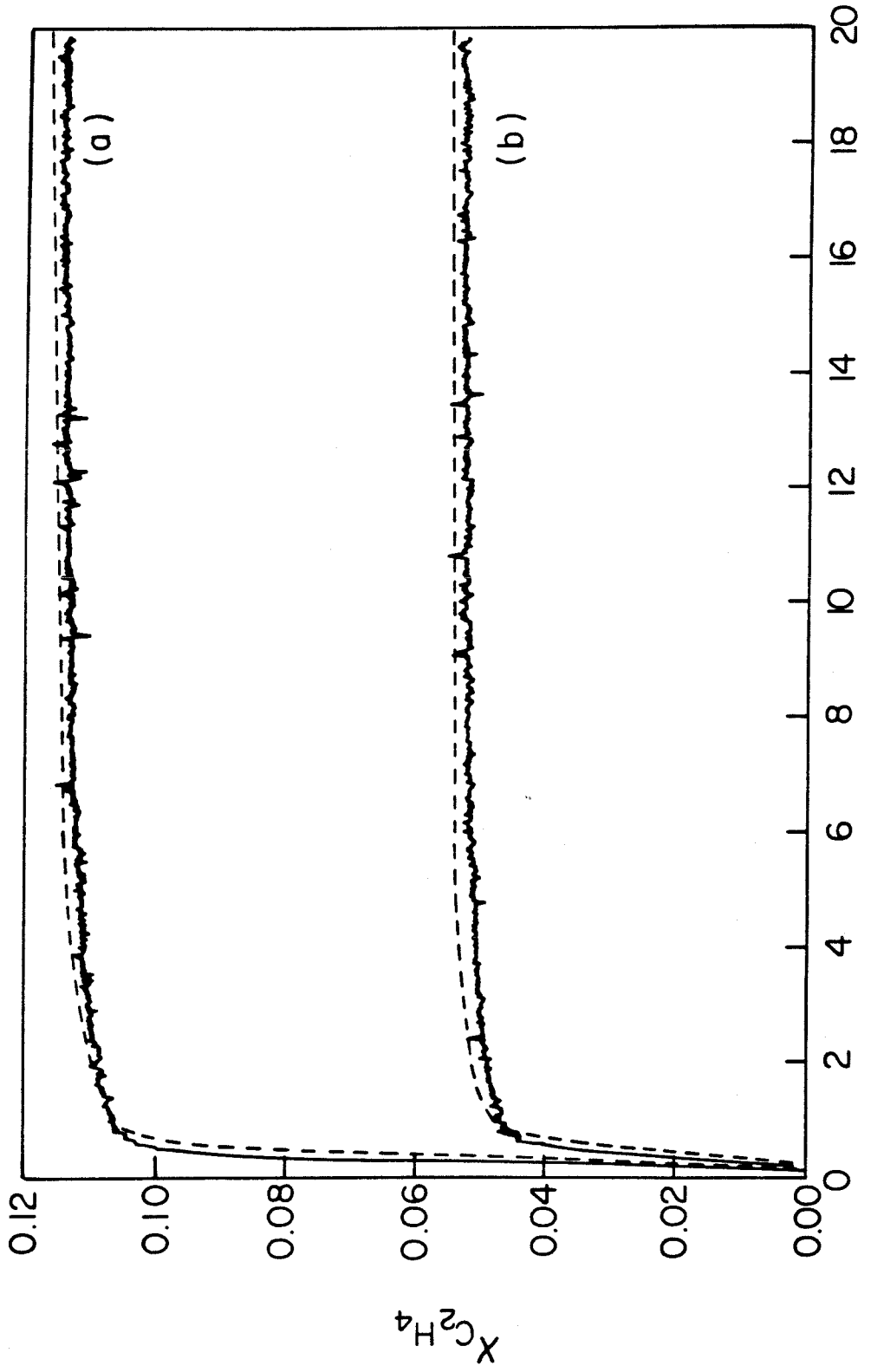
0.12
0.10
0.08
0.06
0.04
0.02
0.00
$\chi_{C_2H_4}$
0
2
4
6
8
10
12
14
16
18
20
Time (min)
(a)
(b)

Figure 4

CHAPTER 5

INFRARED STUDY OF HYDROGEN SPILLOVER DYNAMICS: THE EFFECTS OF ETHYLENE

BACKGROUND

In two recent investigations, isothermal step-response experiments applied to study ethylene hydrogenation on alumina-supported platinum in a fixed-bed CSTR showed dramatically different time scales for 0.05% Pt/Al_2O_3 (Prairie and Bailey, 1987), in comparison to 0.5% Pt/Al_2O_3 (Prairie and Bailey, 1986), for very similar operating conditions. All of the steady-state and step-response data presented in these studies are well-described by a single kinetic model; the two cases differ only in estimated dimensional rate parameters (for steady-state data), and in the time constants associated with dynamic balances on two surface species, namely (a) adsorbed atomic hydrogen, and (b) a hydrogen-deficient adsorbed ethylene species. The detailed mechanistic model and associated dynamic material balances are presented by Prairie and Bailey (1987).

In addition to the step-response method, the previous work also applied feedback-induced bifurcation (Prairie and Bailey, 1986,1987; Prairie *et al.*, submitted) and forced concentration cycling to investigate the validity of the proposed model and to estimate values for two surface time constants. In addition to step-response data, the proposed model is able to describe experimental feedback-induced bifurcation data for both catalysts provided that the time constant for surface hydrogen, τ_{s1}, and that for the hydrogen-deficient ethylene species, τ_{s2}, are properly chosen. The model is unable to describe the results of forced-cycling experiments applied to 0.05% Pt/Al_2O_3; however, qualitative features such as waveform and initial start-up transients are well reproduced with the model.

Table 1 presents the surface time constants which are necessary to reproduce accurately experimental step-response and feedback-induced bifurcation behavior for the two catalysts. As was pointed out previously by Prairie and Bailey (1987), these two experimental methods com-

plement each other since feedback-induced bifurcation tends to focus on faster processes while the step-response method can focus on slower behavior. Hence, the combined use of the two methods resulted in the observation of two very different time scales for ethylene hydrogenation on 0.05% Pt/Al_2O_3. When only a narrow range of time scales dominate, both techniques provide corroborative results, as is seen for 0.5% Pt/Al_2O_3.

The goal here is to identify possible causes of the paradoxical results presented in Table 1. The questions to be addressed are:

1. Why are two vastly different values for τ_{s1} necessary for a complete description of the transient process on 0.05%Pt/Al_2O_3?
2. Why was this disparity not observed for the higher-loaded 0.5% Pt/Al_2O_3 catalyst?

In order to resolve these questions it is important that their background be well understood. For this reason, the experimental conditions and relevant observations from the previous work are listed below:

a. Both catalysts consist of Pt, either 0.05% or 0.5% by weight, distributed in a thin external shell on one-eighth inch dia. alumina pellets. The shell thicknesses are approximately 70 μm and 700 μm, respectively.

b. Ethylene and hydrogen feed compositions between 0 and 20% and a total feed rate of 100 sccm was used for all experiments. The 0.05% experiments (0.94 g catalyst) were performed at 80 °C and those on 0.5% Pt/Al_2O_3 (1 g catalyst) were performed at 30 °C.

c. Steady-state conversion levels of the limiting reagent in the respective experiments were generally much higher for the 0.5% catalyst than for the 0.05% catalyst (80% as opposed to 35%).

d. Very slow loss of activity occurring over approximately 6 hrs was observed for the 0.05% Pt/Al_2O_3 following step changes from H_2(or He)– to C_2H_4– containing reaction environments.

e. The loss of activity produced a catalyst with a decreased, but significant stable level of activity.

f. No loss of activity was ever observed for the 0.5% Pt/Al_2O_3.

g. The 0.05% Pt/Al_2O_3 quickly regained activity upon introduction of H_2/He or pure He into the reactor (c.f., cycling data presented by Prairie and Bailey, 1987).

h. Modeling studies indicate that adsorbed hydrogen is somehow important in the slow deactivation process.

The reversibility of the deactivation, (g), and cessation of deactivation, (e), suggest that deactivation is not caused by an unknown impurity (such as O_2) in the ethylene feed which could have been adsorbing on the platinum to block active sites. Such a poison would adsorb strongly, and rapid reversibility would not have been observed. The fact that a very large value for τ_{s1} (which is defined as a ratio of adsorption sites to the total molar feed rate) is required to describe the slow deactivation suggests that a very large reservoir of active sites might account for the observed dynamics. In both catalysts the alumina support is the obvious choice for such a reservoir. If such a hypothesis is true, the high level of conversion which was employed for the 0.5% experiments in comparison to the 0.05% experiments, (c), could account for the fact that slow dynamics were not observed for the 0.5% catalyst, (f). The rapid transient response to high conversion for the 0.5% catalyst (Prairie and Bailey, 1986; Table 1) indicates that nearly all of the steady-state reaction can be attributed to the Pt metal. Therefore, the effects of another source of ethylene conversion (if one existed) were not detected due to masking by high conversion on

the Pt. This argument is reasonable since steady-state conversion levels (which are a direct result of Pt loading) are the only factors which differed significantly between the experiments with the two catalysts, (a,b).

INTRODUCTION

It is well documented that oxide supports can contribute to the catalytic activity of hydrogenation catalysts through the mechanism of hydrogen spillover (Antonucci *et al.*, 1982; Bianchi *et al.*, 1975; Lacroix *et al.*, 1986; Sinfelt and Lucchesi, 1963). Hydrogen spillover is a phenomenon by which hydrogen atoms chemisorbed on a supported metal (e.g., Pt, Rh, Ni) jump to the oxide support and then migrate by some diffusion-like mechanism to populate the support. The spilled-over hydrogen atoms can equilibrate with surface hydroxyl groups. The entire process is shown schematically in Fig. 1.

Diatomic gaseous hydrogen does not adsorb on alumina unless extremely high temperatures are employed. However, as was demonstrated by Kramer and Andre (1979), gaseous atomic hydrogen (generated using high-frequency discharge) can adsorb to form spillover-like hydrogen atoms. A review of research concerned with understanding hydrogen spillover is presented by Bond (1983). An important property of spilled-over hydrogen is its ability to act as an active site for catalyzing ethylene hydrogenation without itself being consumed (Bianchi *et al.*, 1975).

It is fairly certain that the rate-controlling step for hydrogen spillover on Pt/Al_2O_3 at low temperatures (< 400 °C) is the surface diffusion process (Baumgarten and Denecke, 1986; Bianchi *et al.*, 1983; Cavanagh and Yates, 1981; Dmitriev *et al.*, 1983; Kramer and Andre, 1979), and that equilibration with surface hydroxyls is rapid (Cavanagh and Yates, 1981). Also, removal of spilled-over hydrogen atoms seems to occur via reverse spillover (i.e., diffusion of spilled-over

hydrogens back to the metal, followed by association of hydrogen adatoms and desorption as H_2), rather than by recombination on the oxide followed by desorption (Beck and White, 1984; Conner *et al.*, 1983). The rate-limiting step for the process of reverse spillover is the associative desorption of diatomic hydrogen from the metal crystallites.

Alumina catalysts exhibit distinctly different infrared spectra depending on whether they contain hydroxyl (OH) or deuteroxyl (OD) groups. Thus, since spilled-over hydrogen is in rapid equilibrium with surface hydroxyls, deuterium spillover coupled with transmission infrared spectroscopy provides an excellent system for studying spillover dynamics. Spilled-over deuterium atoms are expected to exchange with hydroxyl groups according to OH + D(s) = OD + H(s) where (s) denotes spilled-over species. A large concentration of D(s) would shift the equilibrium to the right to form a large number of OD groups.

The technique of transmission infrared spectroscopy has been applied in a variety of ways to study hydrogen spillover using OH/OD exchange as an indicator. Cavanagh and Yates (1981) monitored OH/OD exchange at 20 °C on Rh/Al_2O_3 catalysts and concluded that surface diffusion is the rate-limiting process. They also observed that introduction of CO to the catalyst dramatically slows the rate of hydrogen spillover ; this effect was explained in terms of strongly bound CO admolecules blocking sites for hydrogen dissociation, thus greatly reducing the number of hydrogen adatoms available for spillover. Baumgarten and Denecke (1985,1986) used transmission FTIR to study OH/OD exchange on Pt/Al_2O_3 by monitoring IR absorbances at a single wavenumber (the peak of the OD absorbance band) for step changes between H_2– and D_2–containing feedstreams. Their data were interpreted in terms of two distinct reaction processes, one involving OH sites directly adjacent to Pt crystallites, and one diffusion-controlled process involving exchange with OH centers some distance away from the metal sources of hydrogen atoms. Conner *et al.* (1983) used transmission FTIR on a silica wafer which contained

a single spot of Pt/SiO_2 catalyst located at its center. Using a mask, they observed OH/OD exchange as a function of radial position and time following step changes from hydrogen to deuterium environments. Their data show positively that spillover can account for the hydroxyl exchange and that it involves diffusion away from metal centers. The underlying theme in all of these papers is that OH/OD exchange can be monitored using transmission infrared spectroscopy as an indicator of the extent of hydrogen spillover.

This paper describes the application of transmission infrared spectroscopy to study hydrogen spillover dynamics both in the presence and absence of gas-phase ethylene for a 0.05% Pt/Al_2O_3 catalyst at 80 °C. The experimental conditions which are employed carefully mimic those used during our previous work on the same catalyst. Thus it will be determined if hydrogen spillover effects possibly contributed to the slow step-response and cycled-feedstream results observed previously.

EXPERIMENTAL

APPARATUS

A transmission IR reaction cell very similar to cells used previously (Oh and Hegedus, 1982; Prairie *et al.*, in prep.) was constructed of two 4.4 cm dia. stainless steel vacuum flanges to which are mounted 20 mm dia. CaF_2 optical windows. The windows are held in place with threaded nuts and isolated from the reactor with silicon o-rings. The reactor cell supports thin catalyst wafers between the two windows. A typical wafer is 20 mm in diameter, 0.15 mm thick, and composed of about 75 mg of catalyst.

Feed gas enters the reactor through a 1.6 mm (1/16 in) stainless steel tube which is fitted to one of the flanges, and exits through a similar tube on the opposite flange. The cell is designed so entering fluid passes over one side of the wafer, then reverses direction, passes over the other

side, and exits. While ideal CSTR behavior is not expected, a step-response experiment performed with an inert wafer at 80 °C and 100 sccm produced a nearly perfect exponential response with a time constant of 4.6 s. Physical details concerning cell design are very similar to those described by Oh and Hegedus (1982).

The reactor cell is mounted in an aluminum box (10x10x5 cm) which houses a heating element and glass wool insulation. An exposed-tip, T-type thermocouple is mounted in the reactor cell with the tip located approximately 0.2 mm away from one side of the catalyst. All experiments described here were performed at 80 °C. Constant temperature was maintained using a variable transformer to contol the power supplied to the heater element.

Dual-beam IR spectra are obtained using the stock version of a Beckman IR-8 infrared spectrophotometer. Fast-response transient measurements are possible at single wavenumbers, in single-beam mode, by including a high-speed chopper (Laser Precision, Model CTX-534) in the sample beam and replacing the Beckman detector with a solid-state HgCdTe detector (Santa Barbara Research, Model 40742) coupled with a lock-in amplifier (Princeton Applied Research, Model 5101.) All of the single-wavenumber data presented here were obtained using a chopping rate of 400 Hz and a monochrometer slit width of 2 mm. A lock-in prefilter of 0.3 s and no postfilter were used. In this configuration, the single-beam IR system exhibits a time constant of less than 0.5 s. All data, from both the lock-in amplifier and from the IR-8, are recorded using the HP9825 data acquisition and control system described elsewhere (Prairie *et al.*, submitted).

The feed system used for the IR reactor is described in detail elsewhere (Prairie *et al.*, submitted); therefore, only a few important details are described here. Two banks of mass flow controllers regulate the flow rates of He (99.99996%), H_2 (c.p.), and C_2H_4 (c.p.) in one stream and He, D_2 (c.p.), and C_2H_4 in the other, in the ranges of 0 - 200 sccm, 0 - 20 sccm, and 0 - 20 sccm, respectively. A low-volume switching system allows for manual or automatic switching between

feedstreams for step-response and cycled-feedstream experiments. Reactor effluent flows through a continuous infrared analyzer where ethylene concentration is monitored. The total flow rate for all experiments described here was maintained constant at 100 sccm.

It has been pointed out that traces of water or oxygen in the reactor feed can contribute to the OH/OD exchange via a nonspillover mechanism (Bianchi *et al.*, 1983; Conner *et al.*, 1983). Dessicant columns followed by liquid nitrogen traps were installed on the H_2 and D_2 lines to eliminate water from those streams. Exchange which is enhanced by water in the He stream is accounted for in a separate experiment which is described later. No precautions were taken against O_2 impurities in the feed gases.

CATALYST

The catalyst was made by grinding 0.05% Pt/Al_2O_3 pellets (Engelhard) and pressing the resulting powder at 2200 psi to form a 67 mg wafer, 20 mm dia., and 0.145 mm thick. The original catalyst pellets were taken from the same supply which provided material for the ethylene hydrogenation work described previously (Prairie and Bailey, 1987). The fresh catalyst wafer was installed in the IR reactor and heated in 10% H_2/He to 80 °C for 24 hrs.

METHODS

Steady-state and step-response experiments were used in this study. Only single-beam IR measurements are presented. The double beam configuration was used intially to identify the predominant features in the IR spectrum; however, no such data are presented here. Infrared spectra are presented as detector output voltages (transmittance) for the energy range 4000 cm^{-1} to 2000 cm^{-1}. All single-wavenumber transient experiments were performed at 2460 cm^{-1}.

Step-response experiments involve switching from one feed stream to the other, while monitoring 2460 cm^{-1} and the effluent C_2H_4 concentration (when appropriate). Infrared spectra

were recorded before and after most of the step experiments. The scan time for one IR spectrum is 5.5 min.

RESULTS

Figure 2 presents IR spectra for the catalyst wafer subject to three different steady-state gas environments. Curve (a) is the spectrum observed just after the 24 hr pretreatment in 10% H_2. This spectrum was observed whenever the catalyst was allowed to equilibrate with a feed containing H_2 in He and is neither a function of catalyst history (i.e., previous exposure to either D_2 or C_2H_4 did not result in permanent changes) nor hydrogen concentration up to 20%. The broad absorbance band between 3700 cm^{-1} and 2600 cm^{-1} is attributed to hydroxyl groups on the alumina (Cavanagh and Yates, 1981). The narrow doublet at approximately 2300 cm^{-1} is due to ambient CO_2 (Erley and Blake, 1965) and is not observed during double-beam operation.

Curve (b) in Fig. 2 is the spectrum for 20% D_2 in He. As was true for H_2, this D_2 spectrum is always observed if the catalyst is equilibrated with any level of D_2, in the absence of H_2 and C_2H_4; it is insensitive to catalyst history and D_2 concentration. The D_2 spectrum shows relative to the H_2 spectrum, a marked increase in transmittance in the range of 3700 cm^{-1} to 2700 cm^{-1} accompanied by a transmittance decrease between 2700 cm^{-1} and 2000 cm^{-1}. Hydroxyl groups which absorb IR radiation in the range of 3700 cm^{-1} to 2700 cm^{-1} are exchanged with alumina-bound deuterium to form deuteroxyl groups which absorb between 2600 cm^{-1} and 2000 cm^{-1} (Cavanagh and Yates, 1981).

Curve (c) is the steady-state spectrum observed for a feed stream containing 10% D_2 and 10% C_2H_4. This spectrum is stable and reproducible. Under these conditions, ethylene conversion was 12% and the reactor effluent contained 8.9% D_2 and 8.9% C_2H_4. The spectrum shows characteristics of a surface containing both OH and OD groups. During this experiment the

steady-state reaction rate, and hence the rate of heat production, were not large enough to perturb the reactor temperature as measured by the thermocouple. Other experiments with a 20% H_2 and 10% C_2H_4 feed stream resulted in nearly 60% ethylene conversion and an 8 °C rise in the measured temperature.

Figure 2 clearly demonstrates that 2460 cm^{-1} is an excellent choice for the single wavenumber to use for monitoring OH/OD exchange in the transient experiments. This value provides good sensitivity to the OH/OD exchange and is unaffected by gas-phase ethylene (absorbs between 3200 cm^{-1} – 2800 cm^{-1}), ethane (absorbs between 3100 cm^{-1} – 2800 cm^{-1}), or carbon dioxide (Erley and Blake, 1965).

Figure 3 presents results for seven step-response experiments. Infrared transmittance values at 2460 cm^{-1} are plotted against time following the switch for the first two hours of experiments which lasted four hours. Negligible changes in step-response behavior and IR spectra were observed if more than four hours were allowed for equilibration.

The profile labeled B→C results for a switch from 20% H_2 to 20% D_2 in He. It suggests initially rapid OH/OD exchange, followed by a very slow exchange process. Equilibrium is reached after approximately 80 min. The reverse experiment, C→B is shown in the right hand side of Fig. 3. This transient is uniformly slower than its opposite, and more than two hours pass before equilibrium is reached. Since it is expected that OH/OD and OD/OH exchange occur by similar physical processes, the asymmetry of these two experiments is probably a manifestation of a nonlinear relationship between IR transmittance at 2460 cm^{-1} and hydroxyl(deuteroxyl) concentration.

An experiment was performed to check on the exchange rate in the absence of gas-phase hydrogen and deuterium. The reactor feed was switched from 20% D_2 in He to pure He. Results are labeled C→A in Fig. 3. Very slow reversal from a deuteroxyl to a hydroxyl surface is

observed, probably as a result of direct exchange with H_2O impurity in the He feed. This effect is very slow in comparison to the rate of exchange in the presence of H_2.

The curve labeled D→C results for a step from 20% H_2 and 20% C_2H_4 to 20% D_2 in He. The trajectory is nearly identical to that for the B→C experiment. Apparently, the exchange process is unaffected by the ethylene which is in the reactor and on the Pt initially. On the contrary, the opposite switch, C→D, produces an exchange profile which is markedly slowed in comparison to the step to H_2 in He (C→B). Also, the effluent gas-phase ethylene concentration trajectory for the C→D switch (Fig. 4) shows a response time which correlates precisely with that for spillover, and more than two hours are required for steady state to be reached.

A feed stream containing 10% H_2 and 10% C_2H_4 results in an IR spectrum very similar to that for H_2 in He shown in Fig 2(a). Switching from this feed to one containing 10% D_2 and 10% C_2H_4 results in the transient profile lableled E→F in Fig. 3. Exchange is much slower under these conditions than that observed for a switch to D_2 in He (B→C) and results in an intermediate extent of deuteroxylation. The reverse switch (F→E) results in hydroxyl exchange at the same rate as that observed for 20% H_2 and 20% C_2H_4 (C→D). Both produce a completely hydroxylated alumina surface.

Step experiment B→C was repeated on a blank alumina wafer to test the hypothesis that Pt is required for catalyzing the OH/OD exchange. Versal 250 alumina was first wetted in distilled water, then dried and calcined in air at 500 °C overnight to simulate conditions encountered during incipient wetness methods of catalyst impregnation. The alumina was then finely ground and pressed into a 50 mg wafer. The fresh wafer was introduced into the reactor and exposed to 20% H_2 at 80 °C for 24 hrs. Next, the IR spectrum for the alumina wafer was recorded; it closely resembles the IR spectrum in Fig. 2(a). Following this, step experiment B→C was performed; the results are shown in Fig. 5. Clearly, no OH/OD exchange took place. A similar sample of

Versal 250 alumina was then impregnated using incipient wetness with 0.5% Pt (from chloroplatinic acid) and pressed into a wafer. This wafer was then pretreated as usual and then step experiments similar to those outlined in Fig. 3 were performed. This new catalyst exhibited all of the qualitative features shown in Fig. 3. Therefore, it is certain that the Versal alumina used to make the alumina blank can indeed support OH/OD exchange if Pt is present. It is concluded that Pt(or another metal) is an essential ingredient for promoting the OH/OD exchange reaction. Moreover, exchange dynamics are apparently not strongly influenced by catalyst loading or alumina phase composition relative to the effects of the gas-phase composition.

Finally, step experiments similar to B→C and C→B in Fig. 3 were performed on the original 0.05% Pt/Al_2O_3 wafer to investigate the effects of gas-phase $H_2(D_2)$ concentration. Switches between 5% H_2 and 5% D_2 in He produced transient transmittance profiles identical to their counterparts in Fig. 3. Hence, the rate of exchange is not a function of hydrogen(deuterium) pressure in the range 5 - 20%. Consequently, the slowing effect due to C_2H_4 (Fig. 3, C→D, E→F, F→E) cannot be explained by the reduction of hydrogen pressure which accompanies reaction with ethylene.

DISCUSSION

The experimental results are summarized as follows:

1. The rate of OH/OD exchange due to water in the He feed is considerably slower than the exchange rate in H_2 or D_2.
2. Exchange rate is insensitive to gas-phase $H_2(D_2)$ pressure in the range of interest.
3. Platinum (or a similar H_2-dissociating catalyst) is necessary for the OH/OD exchange to occur.

4. Ethylene in conjunction with $H_2(D_2)$ markedly slows the rate of exchange.

5. The exchange rate is insensitive to the concentration of gas-phase C_2H_4 over the range of interest.

6. An IR spectrum for Pt/Al_2O_3 exhibits characteristics of a catalyst supporting both OH and OD groups in the presence of 10% C_2H_4 and 10% D_2.

7. The time required for effluent ethylene levels to reach steady state during reaction experiments correlates very well with the time scale of exchange.

It is evident from (1) and (3) above that hydrogen(deuterium) spillover is the principal mechanism by which the OH/OD exchange proceeds for 0.05% Pt/Al_2O_3 at 80 °C. Oxygen impurity in the H_2, D_2, and He feeds is unlikely to have contributed (via water formation on the Pt crystallites) more to the rate of exchange than that contributed by water in the He feed (Fig. 3, C→A). Therefore, it is concluded that the dynamic exchange experiments provide an accurate indication of spillover dynamics.

The observation that spillover rate is unaffected by hydrogen pressure is expected since the Pt sites are probably saturated with hydrogen adatoms for the temperature and range of hydrogen concentrations which were employed. Furthermore, since initial Pt coverage by ethylene does not affect initial spillover rates, it is concluded that reaction processes on the Pt crystallites are at quasi-steady state in comparison to spillover processes.

The means by which ethylene reduces the rate of spillover is not clearly understood. For example, it is conceivable that gaseous ethylene reacts with spillover hydrogen atoms, via an Eley-Rideal type process or some adsorbed intermediate, to remove them from the alumina, thus slowing the net rate of exchange. It is also possible that ethylene effects the spillover rate by dramatically altering the distribution of adsorbates on the platinum crystallites. If, as suggested

by hydrogenation experiments on 0.5% Pt/Al_2O_3 described earlier, chemical processes on the crystallites are very rapid relative to spillover processes, then the adlayer distribution on the Pt sites would be at quasi-steady state with respect to spillover. Consequently, introducing ethylene in the reactor immediately lowers the concentration of adsorbed hydrogen to a steady-state level characteristic of ethylene hydrogenation on platinum.

The steady-state fractional coverage of Pt sites by hydrogen, θ_H, calculated using the model and parameters proposed by Prairie and Bailey (1987) (0.05% Pt/Al_2O_3 at 80 °C) for 20% C_2H_4 and 20% H_2 in the reactor gas, is 0.13. For 10% C_2H_4 and 10% H_2, this value is 0.20. Therefore, step experiment C→B corresponds to a switch from $\theta_H = 1.0$ to $\theta_H = 0.13$, consequently reducing the driving force for surface diffusion by a factor of 8. A similar argument shows a 5-fold reduction in driving force for a switch to 10% C_2H_4. It is this driving force effect which probably accounts for the reduction in the rate of spillover in the presence of ethylene.

Earlier, discrepancies concerning the time scales for step-response experiments with ethylene hydrogenation were described. A qualitative interpretation including hydrogen spillover as one of the key processes is now proposed to account for this behavior. Bianchi *et al.* (1975) have suggested that spillover-activated alumina can provide sites for ethylene hydrogenation which proceeds through a reaction sequence such as:

$$C_2H_4(g) + H(s) \rightarrow C_2H_5(s) \quad (1)$$

$$C_2H_5(s) + H_2(g) \rightarrow C_2H_6(g) + H(s) \quad (2)$$

$$C_2H_5(s) + H(s) \rightarrow C_2H_6(g) \quad (3)$$

Equations (1-3) describe a chain mechanism with Eq. (2) as the propagating step and Eq. (3) as the terminating step (which results in consumption of spilled-over hydrogen atoms).

If steps (1) and (2) were at quasi-steady state with respect to the rate of spillover, then the slow decline in the activity of the 0.05% Pt/Al_2O_3 could be explained solely in terms of a balance on spilled-over hydrogen. Switching from H_2 in He to C_2H_4 and H_2 in He results in the immediate reduction of the concentration of hydrogen atoms on the Pt sites. This effect could promote *reverse* spillover which would lead to a lower concentration of spilled-over atoms, and thus to lower ethylene conversion levels. The effects of reverse spillover would be augmented by termination step (Eq. 3) to deplete the alumina of spilled-over hydrogen so that it could no longer contribute to the overall rate of hydrogenation. Reverse spillover is likely in the presence of ethylene since the rate-limiting step for reverse spillover, which is the associative desorption of hydrogen from Pt sites, is effectively bypassed by lowering the Pt-H concentration through reaction with ethylene. Any hydrogen that migrated back to the Pt crystallites via reverse spillover would be rapidly consumed by ethylene. Also, since spillover is limited by the rate of diffusion, it is reasonable that both forward and reverse spillover would exhibit similar dynamics. The observation that effluent ethylene trajectories occur on the same time scale as spillover is compatible with this argument.

It is proposed, then, that hydrogen spillover effects account for the slow decline in the catalytic activity of the 0.05% Pt/Al_2O_3 catalyst at 80 °C. Accordingly, in terms of modeling, the large time constant arises due to the spillover-related phenomena, and the smaller one accounts for ethylene hydrogenation on platinum. Only one characteristic time constant was observed for the higher-loaded 0.5% Pt/Al_2O_3 because it provided a sufficient number of Pt sites for nearly complete conversion of the limiting reagent, and therefore spillover was not a factor. More experiments using deuterium and hydrogen on very low-loaded catalysts (to eliminate conversion on Pt) coupled with transmission IR and mass spectroscopies would be helpful for identifying the true mechanism of ethylene hydrogenation on spillover alumina.

Finally, observation (6) concerning the intermediate spectrum in the presence of both D_2 and C_2H_4 is strong evidence in favor of the dissociative ethylene adsorption step

$$C_2H_4(g) + Pt \rightleftharpoons C_2H_3(Pt) + H(Pt). \quad (4)$$

which has been applied in earlier modeling investigations (Prairie and Bailey, 1986,1987; Saltsburg and Mullins, 1982). At steady state, such a hydrogen source is necessary to explain the observed IR spectrum which exhibits features of both OH and OD groups.

REFERENCES

Antonucci, P., N. Van Truong, N. Giordano, and R. Maggiore (1982). Hydrogen spillover effects in the hydrogenation of benzene over Pt/γ–Al_2O_3 catalysts. *J. Catal.* **75,** 140-150.

Baumgarten, E., and E. Denecke (1985). Hydrogen spillover in the system Pt/Al_2O_3, I. Fundamental observations. *J. Catal.* **95,** 296-299.

Baumgarten, E., and E. Denecke (1986). Hydrogen spillover in the system Pt/Al_2O_3, II. Experimental problems and influence of OH- or OD- coverage. *J. Catal.* **100,** 377-382.

Beck, D.D., and J.M. White (1984). Spillover of deuterium on Pt/TiO_2. 1. Dependence on temperature, pressure, and exposure. *J. Phys. Chem.* **88,** 2764-2771.

Bianchi, D., G.E.E. Gardes, G.M. Pajonk, and S.J. Teichner (1975). Hydrogenation of ethylene on alumina after hydrogen spillover. *J. Catal.* **38,** 135-146.

Bianchi, D., D. Maret, G.M. Pajonk, and S.J. Teichner (1983). Exchange of surface hydroxyls of silica by deuterium spillover. In *Spillover of adsorbed species,* G.M Pajonk, S.J. Teichner, and J.E. Germain, Eds., Elsevier: Amsterdam, pp 45-52.

Bond, C. (1983). A short history of hydrogen spillover. In *Spillover of adsorbed species,* G.M Pajonk, S.J. Teichner, and J.E. Germain, Eds., Elsevier: Amsterdam, pp 1-16.

Cavanagh, R.R., and J.T. Yates, Jr. (1981). Hydrogen spillover on Al_2O_3: A study by infrared spectroscopy. *J. Catal.* **68,** 22-26.

Conner, W.C, J.F. Cevallos-Candau, N. Shah, and V. Haensel (1983). Hydrogen spillover and surface diffusion: spillover from a point source. In *Spillover of adsorbed species,* G.M Pajonk, S.J. Teichner, and J.E. Germain, Eds., Elsevier: Amsterdam, pp 31-43.

Dmitriev, R.V., A.N. Detjuk, Ch.M. Minachev, and K.-H. Steinberg (1983). Investigation of hydrogen spillover on metal-containing catalysts by isotopic exchange. In *Spillover of adsorbed species,* G.M Pajonk, S.J. Teichner, and J.E. Germain, Eds., Elsevier: Amsterdam, pp 17-29.

Erley, D.S., and B.H. Blake (1965). *Infrared spectra of gases and vapors: Volume II - grating spectra.* Dow Chemical Company, Midland, Michigan.

Kramer, R., and M. Andre (1979). Adsorption of atomic hydrogen on alumina by hydrogen spillover. *J. Catal.* **58,** 287-295.

Lacroix, M., G.M. Pajonk, and S.J. Teichner (1986). Silica and alumina catalysts, activation by hydrogen spillover for the conversion of n-heptane at 270 °C. *J. Catal.* **101,** 314-322.

Oh, S.H., and L.L. Hegedus (1982). Dynamics of high-temperature carbon monoxide chemisorption on platinum- alumina by fast-response IR spectroscopy. In *Catalysis Under Transient Conditions,* A.T. Bell and L.L. Hegedus, Eds., ACS Symposium Series, No. 178, pp 79-103.

Prairie, M.R, and J.E. Bailey (1986). Application of feedback-induced bifurcation for evaluating steady-state and transient heterogeneous catalysis kinetic models. *Chem. Engng. Sci.* **41,** 937-944.

Prairie, M.R, and J.E. Bailey (1987). Experimental and modeling investigations of steady-state and dynamic characteristics of ethylene hydrogenation on Pt/Al_2O_3. *Chem. Engng. Sci.* In press.

Prairie, M. R, B.H. Shanks and J. E. Bailey . Intentional Manipulation of closed-loop time delay for model validation using feedback-induced bifurcation. Submitted.

Prairie, M.R., S.H. Oh, B.K. Cho, E. J.Shinouskis, and J.E. Bailey. Steady-state and transient studies of CO oxidation on alumina supported rhodium via transmission IR spectroscopy. In preparation.

Saltsburg, H., and M. E. Mullins (1982). Surface hydrogen in heterogeneous catalysis. *Ann. New York Acad. Sci.* 82-96.

Sinfelt, J. H., and P. J. Lucchesi (1963). Kinetic evidence for the migration of reactive intermediates in surface catalysis. *J. Amer. Chem. Soc.* **85,** 3365-3367.

Table 1. Comparison of modeling time scales for surface hydrogen dynamics on 0.05% and 0.5% Pt/Al_2O_3 catalysts.

Experiment / Catalyst	Hopf Bifurcation	Step-response
0.05% Pt/Al_2O_3	$\tau_{s1} = 1$ s	$\tau_{s1} = 5000$ s
0.5% Pt/Al_2O_3	$\tau_{s1} \leq 2.5$ s	$\tau_{s1} = 2.5$ s

FIGURE CAPTIONS

1. Schematic diagram of intermediates and processes in hydrogen spillover.
2. Steady-state IR spectra for 0.05% Pt/Al_2O_3 at 80 °C in: (a) 10% H_2, (b) 20% D_2, and (c) 10% D_2 + 10% C_2H_4, all diluted in helium.
3. Hydroxyl/deuteroxyl exchange dynamics presented as transient step-response IR transmittance profiles at 2460 cm^{-1} for a variety feed concentrations (listed in the key). The left side of the figure shows results for steps to deuterium-containing feeds, and the right side shows results for steps to hydrogen-containing feeds. The abscissa indicates time since the switch.
4. Transient response of gas-phase ethylene concentration in the reactor effluent for a step change in feed composition of 20% D_2 switched to 20% H_2 + 20% C_2H_4. The data were recorded simultaneously with the transient IR data in Fig. 3 (C→D).
5. Transient profile showing negligible OH/OD exchange on blank alumina at 80 °C. Transmittance at 2460 cm^{-1} is plotted against time-since-the-switch for 20% H_2 going to 20% D_2, in helium.

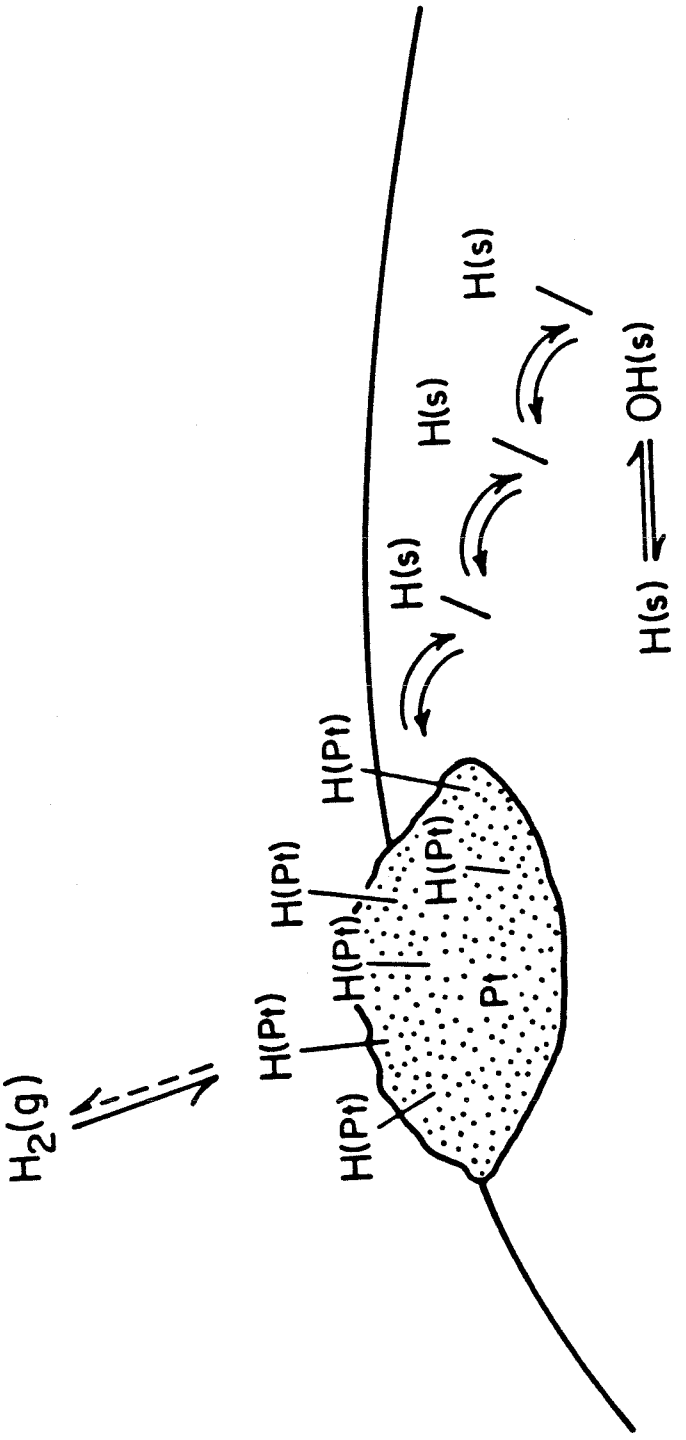

Figure 1

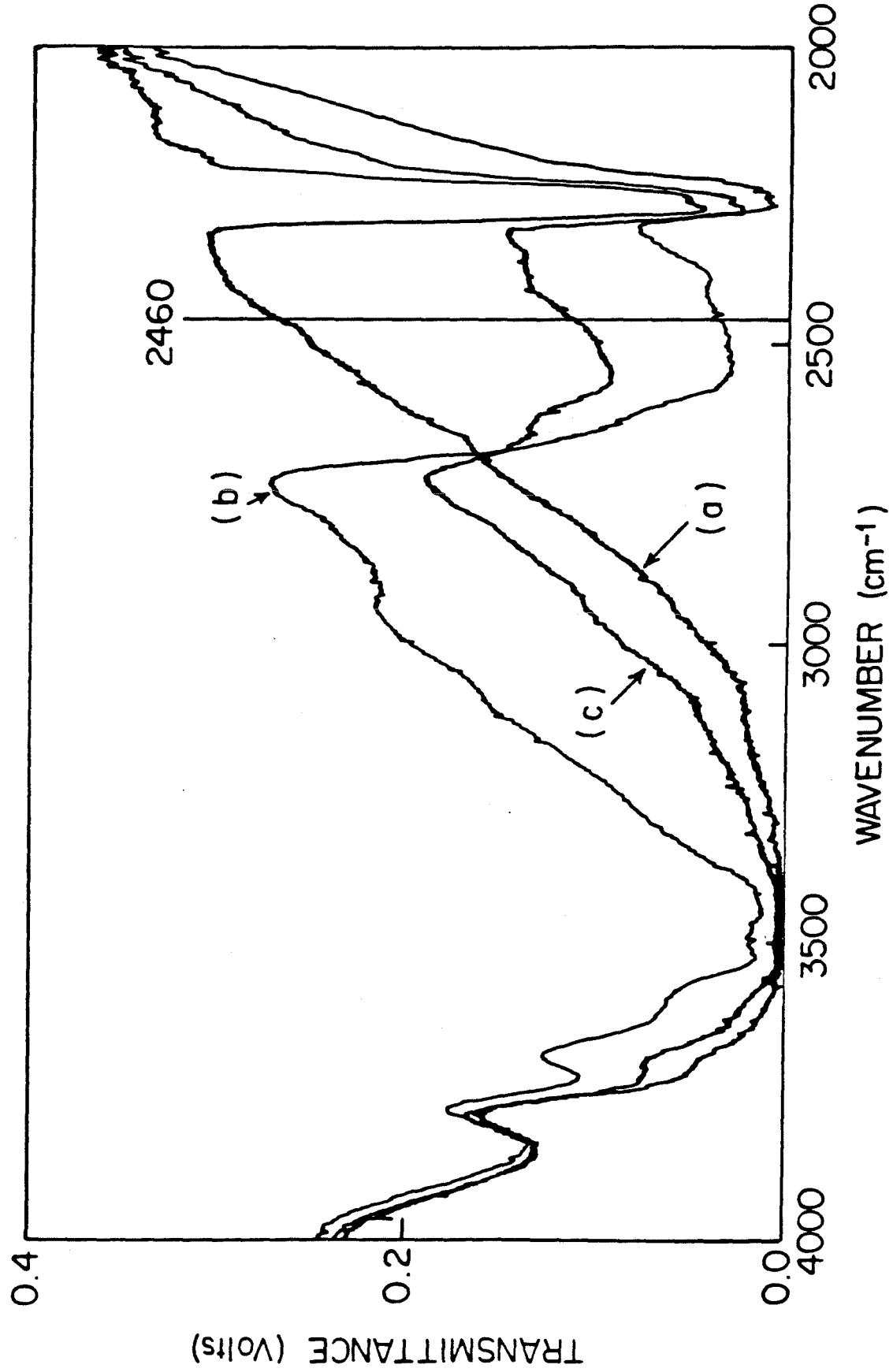
TRANSMITTANCE (Volts)
0.4
0.2
0.0
4000
3500
3000
2500
2000
WAVENUMBER (cm-1)
2460
(a)
(b)
(c)

Figure 2

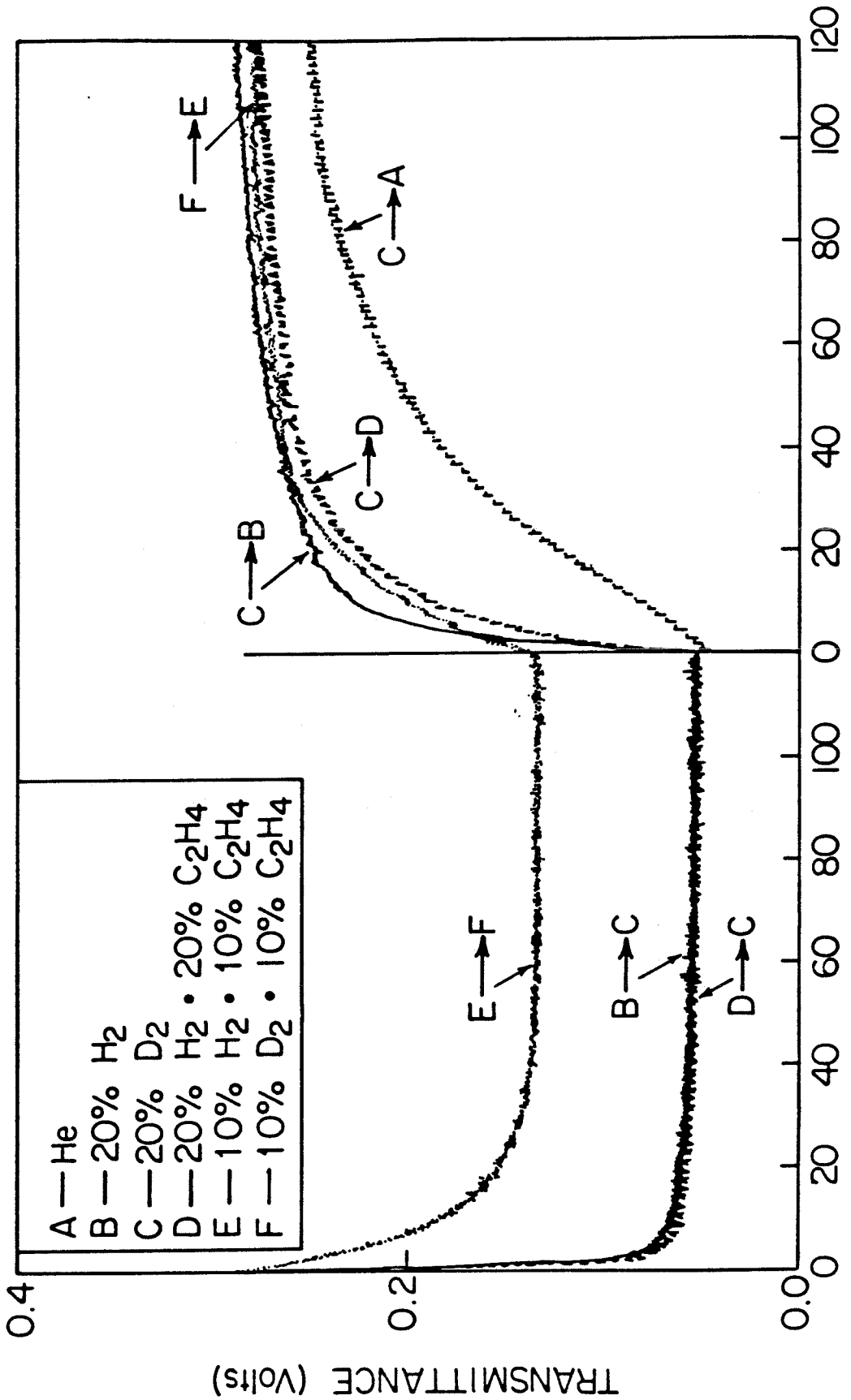
A — He
B — 20% H2
C — 20% D2
D — 20% H2 • 20% C2H4
E — 10% H2 • 10% C2H4
F — 10% D2 • 10% C2H4
TRANSMITTANCE (Volts)
0.4
0.2
0.0
0
20
40
60
80
100
0
20
40
60
80
100
120
TIME (min)
F → E
C → A
C → D
C → B
E → F
B → C
D → C

Figure 3

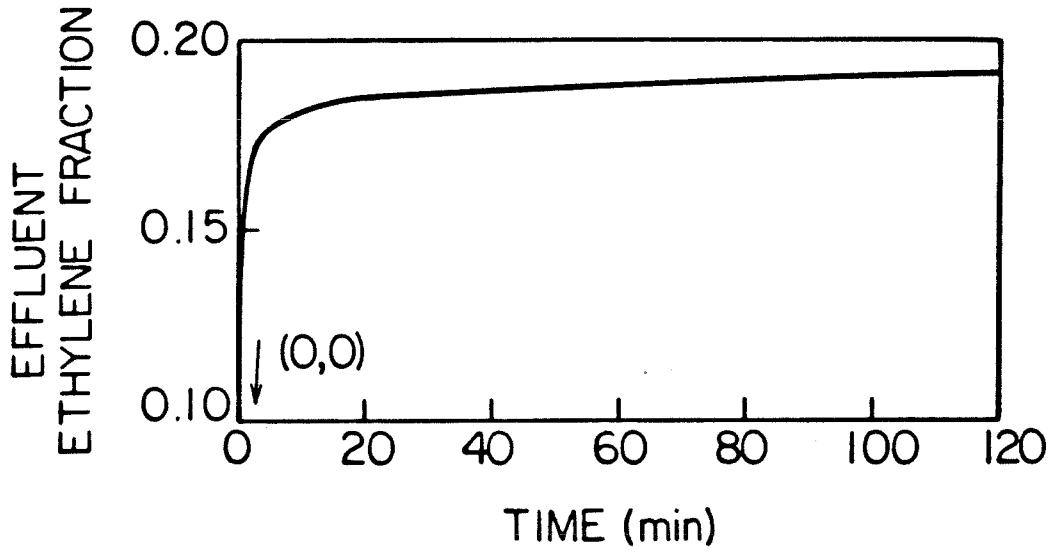
EFFLUENT
ETHYLENE FRACTION
0.20
0.15
0.10
(0,0)
0
20
40
60
80
100
120
TIME (min)

Figure 4

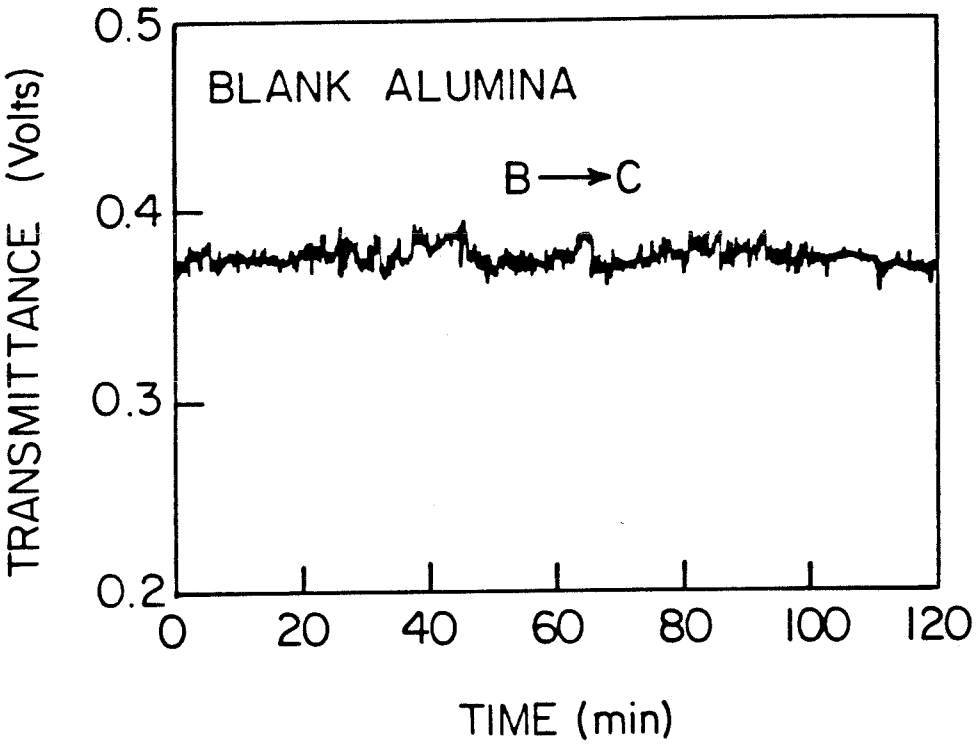
BLANK ALUMINA
B → C
TRANSMITTANCE (Volts)
0.5
0.4
0.3
0.2
0
20
40
60
80
100
120
TIME (min)

Figure 5

CHAPTER 6

STEADY-STATE AND TRANSIENT STUDIES OF CO OXIDATION ON ALUMINA-SUPPORTED RHODIUM VIA TRANSMISSION IR SPECTROSCOPY

INTRODUCTION

Many researchers have used infrared (IR) spectroscopy to study CO chemisorption on supported rhodium (e.g., Cavanagh and Yates, 1981; Primet, 1978; Rice *et al.*, 1981; Yates *et al.*, 1979). The predominant features in the IR spectrum for this system are a doublet at about 2100 and 2030 cm^{-1} corresponding to a dicarbonyl species ($Rh(CO)_2$) and a singlet near 2065 cm^{-1} attributed to linearly bound (terminal) CO (RhCO). Bridge-bonded CO (Rh_2CO) exhibits a broad peak near 1900 cm^{-1}. Although the chemical nature of the adsorbed CO species and the effects of experimental conditions (e.g., temperature, gas composition, dispersion, loading, support material, pretreatment, Rh oxidation state, etc.) on these species have been studied extensively, reports describing the application of IR spectroscopy to study steady-state *and* dynamic behavior of adsorbed CO during catalytic reaction with oxygen are less common.

Direct IR measurement of surface concentration (coverage) during forced and autonomous transients is a powerful method for elucidating elementary adsorption and desorption processes and is also extremely valuable for studying more complicated multi-species catalytic reactions. While gas-phase composition measurements are usually adequate for characterizing the steady-state kinetics of a catalytic reaction, those types of measurements are sometimes neither sensitive enough nor robust enough to obtain an accurate description of surface phenomena that may dictate transient behavior. Such descriptions of surface phenomena are essential for modeling of dynamic catalytic reactors. Also, since the molar capacity of a catalyst is usually very small with respect to the overall reactor capacity, gas-phase transients can be difficult to resolve, even when surface coverages undergo dramatic changes. Surface concentration measurements provide very sensitive estimates of the state of a catalytic system and therefore an excellent basis for model comparisons and parameter estimates. Accordingly, researchers have developed transmission infrared spectroscopy (TIR) (dispersive and Fourier transform) for *in situ* measurements of

surface coverages during reaction, adsorption and desorption on supported metal catalysts.

Oh and Hegedus (1982) designed a fast-response transmission infrared system for adsorption and desorption of CO on Pt/Al_2O_3 and found the rate of change in coverage to be profoundly influenced by internal diffusion. In another study, Elhaderi and Tsotsis (1982) used TIR spectroscopy to study autonomous oscillations during CO oxidation on Pt/Al_2O_3. These researchers were convinced that kinetic (and possibly transport) interactions rather than impurities were responsible for the observed bifurcations. An interesting TIR (Fourier transform type) study by Haaland and Williams (1982) showed that the peak position for linear CO on Pt depends on coverage in an inert environment but remains constant if oxygen is present. This observation was explained in terms of island formation. Islands of densely packed CO adsorbate (saturation coverage) are surrounded by areas of oxygen and bare metal and thus the linear-CO peak position remains constant at its saturation value. Studies by Kaul and Wolf (1984,1985) using transmission Fourier transform infrared spectroscopy and careful surface temperature measurements showed dramatic temperature excursions and sustained oscillations for CO oxidation on Pt/SiO_2. Their observations were explained in terms of complex energy transport processes and intra- and extra- particle nonuniformities. Recently, Barshad *et al.* (1985) used TIR spectroscopy to study CO oxidation over Pt/Al_2O_3 under forced transient conditions. These researchers obtained time-average IR spectra for cyclic operation which suggested a new form of adsorbed CO (one which is linearly adsorbed on a platinum atom sharing an oxygen adatom with its neighbors) as the reactive intermediate for CO_2 production.

Unfortunately, operating conditions which are best for TIR experiments (relatively thick wafer with high metal loading) also introduce transport effects which greatly increase the complexity of data interpretation. Thus, in addition to providing some basic information on CO adsorption, desorption, and oxidation on supported rhodium, an aim of this paper is to provide a

detailed qualitative and somewhat quantitative look at the effects of intraparticle diffusion and external mass transport on the simple processes of transient desorption and steady-state oxidation as they occur in a typical TIR spectroscopy-catalytic reactor system. After a description of the apparatus and the Rh/Al_2O_3 catalyst, experimental results are presented for IR calibration (molar coverage in terms of infrared absorbance at a fixed wavenumber.) Following this, transient CO adsorption and desorption experiments in the absence of O_2 are then summarized and analyzed using a mathematical model. Next, experiments for studying steady-state oxidation and step- and forced-cycling transient operation near stoichiometric reaction conditions are described.

EXPERIMENTAL

Materials and Methods

The experimental reactor is a stainless steel transmission IR cell constructed from two conflat flanges containing sapphire windows. The reactor cell contains a catalyst disc that is approximately 0.2 mm thick with a diameter of 2 cm. The disc is held perpendicular to one beam of a dual-beam Perkin-Elmer model 180 infrared spectrometer. Gas flows to the reactor through one of two rotameter-controlled feed manifolds. Carbon monoxide (Matheson 10% in He), O_2 (Matheson 10% in He), He (99.999%), and Ar (1250 ppm in He) are simultaneously available in each feedstream, and the reactor effluent and bypass lines are pressure balanced so as to avoid pressure surges that might occur when the reactor feed is switched from one feed bank to the other. The reactor feed can be switched from bank to bank either manually or with a DEC-MINC minicomputer to produce step- or cycled-feedstream inputs. Total flow rate for all experiments was 8 l/min at room temperature and 900 torr. The reactor is maintained at elevated temperatures with a heating tape surrounded by glass wool insulation. An unsheathed thermocouple in near

proximity to the pellet is used for feedback control of the reactor temperature. The feed to the reactor passes through a glass preheat section that brings it to reaction temperature.

Gas-phase analysis of the reactor effluent is accomplished via a UTI 100C mass spectrometer operating at approximately 10^{-5} torr. Reactor gas is sampled with a two-stage pressure reduction system that minimizes component separation due to differences in the molecular diffusivities of the constituent gases. Operating modes of the UTI 100C can be set manually or automatically with the MINC minicomputer. During manual operation, the steady mass spectrum of the reactor gas can be monitored over a range of mass numbers, and stored digitally if desired. Automatic control of the spectrometer allows for a transient record of peak intensities at several discrete mass numbers. During transient experiments, the signal intensities of four mass numbers (28,32,40,44) were measured at the sampling rate of 10 Hz.

The transmission IR spectrometer can be used to measure the entire IR spectrum of an equilibrated catalyst or to accomplish high speed absorbance measurements at a single wavenumber. The high speed measurements are accomplished using a 1 kHz chopper, a lock-in amplifier, and a fast-response Hg-Cd-telluride solid-state detector. Single-wavenumber measurements are made in a single-beam configuration and full spectra are recorded in the dual-beam mode. IR spectra and single-wavenumber transmittance data are measured and recorded with the MINC. More details of the experimental system are presented elsewhere (Oh and Hegedus, 1982).

It is frequently assumed that the flange type TIR cells like the one described here behave as ideal stirred tank reactors and hence that the catalyst wafer is everywhere subject to the same surface composition. Tracer step-change experiments for the cell approach ideal exponential behavior. However, the rapid reactor response makes the true shape of the residence time distribution function difficult to resolve. The residence time of the preheater is 0.23 s in comparison to

that of the reactor cell which is 0.008 s (room temperature, 900 torr); hence, most of the feed gas mixing occurs in the preheater. Under some experimental conditions, such as those encountered during transient desorption studies, the assumption of ideal CSTR behavior for the reactor is a reasonable approximation. However, under conditions of significant CO conversion, spatial gradients may exist in the gas-phase composition exposed to the catalyst pellet.

The supported Rh catalyst used in these experiments was prepared by impregnating Alon fumed alumina powder to incipient wetness with an aqueous $RhCl_3$ solution. The wet catalyst was allowed to dry overnight in a fume hood and the resulting pink solid was finely ground and calcined in flowing air at 500 °C for five hours. The catalyst was then pressed into approximately 100 mg pellets at 6 tons per square inch for five minutes. The pressed pellets were approximately 0.2 mm thick, 2 cm in diameter and 80-100 mg in mass. Quantitative analysis showed that the Rh/Al_2O_3 pellets contain 0.4-0.5% Rh and approximately 0.2% chloride by weight. Hydrogen chemisorption onto the fresh catalyst indicated a dispersion of 49%, based on 0.5% loading and a one-to-one Rh atom to hydrogen atom adsorption stoichiometry. A fresh 91 mg pellet was inserted into the reactor and pretreated per the following schedule:

1. Heat in He at 8 l/min and 900 torr to 450 °C.
2. Oxidize in 1% O_2 at 450 °C, 8 l/min and 900 torr for 1 hr.
3. Purge the reactor for 10 minutes in 8 l/min of pure He.
4. Reduce in 1% H_2 at 450 °C, 8 l/min and 900 torr for 1 hr.
5. Cool to operating temperature in 8 l/min of pure He.

After the pretreatment, 1% CO in He at 900 torr and 250 °C was admitted to the reactor. The resultant steady-state IR spectrum is shown in Figure 1a. The predominant structure is the dicarbonyl doublet at 2095 and 2026 cm^{-1}. Between the two peaks that make up the doublet is a

shoulder that corresponds to the linear CO stretching vibration. The presence of bridge-bonded CO is obscured since the sapphire windows start to absorb IR radiation at the lower wavenumbers. The spectrum in Figure 1a agrees qualitatively with observations by other workers, although a more definitive linear CO peak has sometimes been observed (Primet, 1978; Yates *et al.*, 1979). The lack of a strong linear CO peak here is suggestive of high dispersion, low loading, or partially oxidized rhodium (Cavanagh and Yates, 1981; Yates *et al.*, 1979). The small spike on the low-wavenumber side of the dicarbonyl doublet in Figure 1a and subsequent figures is caused by a grating change within the spectrophotometer. After recording the spectrum in Figure 1a, the reactor feed was switched to 1% O_2 in He, and after 30 minutes the spectrum in Figure 1b was recorded. At 250 °C, adsorbed dicarbonyl CO reacts rather slowly with oxygen. Cavanagh and Yates (1981) made a similar observation . Subsequently, the reactor was heated to 300 °C, and again 1% CO in He was introduced to the catalyst. The resulting spectrum is presented in Figure 1c. This spectrum shows a significant decline in peak height for dicarbonyl and somewhat better resolution of the linearly bonded CO shoulder. It is not obvious if the differences between Figures 1a and 1c are due to the elevated temperature or to surface-adsorbate interactions.

To investigate the effect of age (i.e., the effect of use), the reactor was briefly purged at 300 °C with He, then subjected to a 1% O_2 stream for 15 minutes, purged again, and finally allowed to equilibrate with a 1% CO stream. The resulting spectrum is shown in Figure 1d. A pronounced change in IR spectrum occured between the time when the pellet was first pretreated and when it has been slightly aged. Finally, the IR spectrum typical of a stabilized Rh/Al_2O_3 pellet is shown in Figure 1e. To get to this stage in its life, the catalyst was repeatedly reduced in CO, oxidized in O_2 and subjected to steady reaction conditions where both CO and O_2 were present in the reactor.

It was not possible by any treatment applied to restore the catalyst to its original condition as indicated by the adsorbed CO spectrum. In particular, re-pretreatment per steps 1-5 above hardly affected the IR spectrum for adsorbed CO on the stabilized catalyst. Accordingly, the spectrum shown in Figure 1e is taken to be representative of the stabilized catalyst. This permanent change in the nature of the catalyst cannot be explained in terms of Rh oxidation alone because changes in the Rh oxidation state have been shown to be reversible at these temperatures (Oh and Carpenter, (1983). Sintering is a likely candidate for the permanent change in the catalyst. However, comparison of H_2 chemisorption results for the fresh catalyst with titration data for the stabilized catalyst does not support this hypothesis.

Since characterization of the CO oxidation reaction on supported Rh under relatively realistic operating conditions is a central goal of this research, all further experiments were done with the stabilized catalyst. Also, this allows reproduction of the catalyst state (with respect to adsorbed CO infrared spectrum) for different types of experiments.

CO Coverage Versus IR Absorbance at 2035 cm^{-1}

The IR spectra of adsorbed molecules are functions of temperature and adsorbate concentrations. For a given coverage, peak heights as well as peak positions are temperature dependent. Given this situation, to establish a relationship between CO coverage and IR absorbance at a single wavenumber, it is necessary to choose an operating temperature suitable for an entire set of experiments. Three factors contributed to the choice of 300 °C as the operating temperature for this work: (a) adsorbed CO desorbs in He at a significant rate at 300 °C, (b) the CO oxidation reaction is reasonably fast at 300 °C, and (c) lower temperatures result in complications arising from autonomous oscillations, which are discussed in a later section. The importance of factors (a) and (b) will become evident from descriptions of experimental methods that appear later in this section.

At a given temperature, the IR absorbance spectrum provides a direct measure of the amount of CO on the metal surface. The measurable variable that theoretically correlates with surface concentration is the integrated IR absorbance band intensity for the species in question. However, provided that a unique, one-to-one relationship exists between band area and IR absorbance at a single wavenumber, then using the single-wavenumber measurement for estimating surface coverage is justified. This fact was used to establish a quantitative relationship between IR absorbance at a single wavenumber and CO coverage. Unfortunately, the position of the linearly bonded CO peak shifts towards higher energy as coverage increases, complicating the choice of a good wavenumber for single-line coverage measurements. The shift to higher energy is actually a shift towards the gas-phase CO stretch and is probably due to dipole-dipole coupling in the adsorbed layer. Unlike the linearly bonded species, the peak positions for dicarbonyl CO remain unaffected by CO coverage.

Figure 2 shows how the IR spectrum for the catalyst varies with CO concentration in the reactor gas at 300 °C. Each spectrum was recorded after the pellet was allowed to equilibrate with a different concentration of gas-phase CO, each of which was established by slightly adjusting the CO rotameter valve to admit a range of CO concentrations into the reactor cell. Resolution of the calibration of the CO rotameter is at its worst near the very low level of gas-phase CO that is sufficient to cover the Rh surface. Thus it is impossible to be precise as to the exact gas concentrations giving rise to the various spectra in Figure 2. Each spectrum represents the catalyst in the stabilized condition with the uppermost trace corresponding to the maximum achievable coverage at 300 °C. Maximum coverage is reached at approximately 0.1% gas-phase CO. Figure 2 clearly demonstrates why 2035 cm^{-1} was chosen as the value to use for the single-wavenumber experiments. At 2035 cm^{-1}, coverage and absorbance have a unique relationship (i.e., single wavenumber absorbances correlate one-to-one with integrated band intensities) with

maximum sensitivity. Lower wavenumbers result in ambiguity in the absorbance-coverage relationship, while higher wavenumbers result in less sensitivity.

The calibration curve in Figure 3 was constructed from titration experiments at 300 °C and 2035 cm^{-1}. Each point in Figure 3 was obtained through the following procedure:

1. Allow the catalyst to equilibrate with 1.5% CO at 300 °C and 900 torr while monitoring IR absorbance at 2035 cm^{-1}.
2. Switch reactor feed to pure He and monitor absorbance at 2035 cm^{-1}.
3. Follow CO desorption with the IR spectrometer.
4. When the desired absorbance is reached, switch the reactor feed to 1.5% O_2 and 0.0125% Ar in He.
5. Monitor CO_2 and Ar on the mass spectrometer at m/e = 44 and m/e = 40, respectively.

Argon was present in the O_2 stream as a calibration standard from which CO_2 levels were calculated. Carbon dioxide production for each data point was calculated using the equation

$$\%CO_2 = \int_0^{\tau_e} (I_{44}(t) - I_{44}^e) \times \frac{0.0125\%}{I_{40}^e - I_{44}^e}\, dt \qquad (1)$$

where

$I_{44}(t)$ = CO_2 transient mass spectrometer signal

I_{44}^e = background CO_2 level

I_{40}^e = eventual 0.0125% Ar mass spectrometer signal

and

τ_e is a time sufficiently long after the switch to oxygen feed so that CO_2 production is negligible.

Then, knowing the total molar flow rate through the reactor, an estimate for the total amount of CO_2 produced during each titration was possible. Inherent in this analysis is the assumption that the mass spectrometer is equally sensitive to CO_2 and Ar and the assumption that the nonequimolar stoichiometry does not cause the molar effluent rate to be significantly different from the molar feed rate. The first assumption is common in this type of analysis; however, there is potential for underestimating the CO_2 level by as much as 20% (UTI publication). Errors in this estimation do not affect CO coverage estimates. However, such errors bias rate calculations presented later. At the low adsorbate/reactant mole fractions involved here, the second assumption is clearly a satisfactory approximation.

The amount of CO_2 produced in each titration is equal to the amount of CO that was present on the catalyst at the time of the switch to O_2 feed if the rate of CO desorption (in the presence of oxygen) is much slower than the rate at which adsorbed CO is consumed by reaction with oxygen. It has previously been reported that CO inhibits the oxidation reaction, indicating that CO adsorbs much faster than it desorbs in a gaseous environment containing both reactants (Oh *et al.*, 1986). Figure 4 presents transient profiles from a typical titration experiment. The lowest curve in the figure is the transient IR absorbance at 2035 cm^{-1} and 300 °C. Clearly, the slope during oxidation (starting with the switch to oxygen-containing feed at the time denoted t_o) is much greater than that during desorption into helium ($t<t_o$). Consequently, the rate of reaction is much faster than the rate of desorption. Also, negligible CO was observed in the reactor effluent with the mass spectrometer during a few representative titration runs. It is concluded that essentially all of the CO on the catalyst corresponding to the IR absorbance at time t_o in Figure 4 was converted to CO_2.

With reference to the calibration curve in Figure 3, the maximum production of CO_2 observed using the titration technique was approximately 3.77 μmol. This value was corrected for

the zero absorbance offset that was probably due to CO uptake by surfaces not contained within the catalyst pellet (assuming negligible adsorption on alumina). The corrected maximum CO uptake is 3.2 μmol which corresponds to 72% disperse Rh on the 91 mg catalyst pellet, assuming one-to-one CO adsorption stoichiometry. For comparison, hydrogen chemisorption experiments indicated that the fresh catalyst consists of 49% disperse Rh on Al_2O_3. If 49% is assumed to be the correct value for the stabilized catalyst, then 3.2 μmol CO on the 91 mg pellet translates into 1.48 CO molecules per surface Rh atom, or possibly $Rh_2(CO)_3$ overall adsorption stoichiometry. It is unlikely that the catalyst gained active sites during stabilization (49% dispersion initially, compared to 72% assuming linear CO on the stabilized catalyst). Assuming that Rh in the stabilized catalyst is 49% dispersed, two possibilities may be imagined: (*i*) the CO-saturated catalyst is 50% covered by linearly bound CO and 50% covered by dicarbonyl CO, or (*ii*) $Rh_2(CO)_3$ is the true adsorption stoichiometry for the stabilized catalyst. The IR spectra for the stabilized catalyst in Figures 1 and 2 show very little contribution from the dicarbonyl species so (*i*) is unlikely. From a phenomenological point of view, explanation (*ii*) is reasonable. Such a species has been postulated previously and was assigned to a coverage-varying single peak occuring between 1900 and 1920 cm^{-1} (Rice *et al.*, 1981). This peak was not observed for our stabilized catalyst pellet, however. Further research is needed in order to clarify this issue.

The data in Figure 3 were fit to a quadratic function using a nonlinear least squares procedure resulting in

$$\theta_{CO} = 6.8A^2 + 0.29A \qquad (2)$$

where θ_{CO} is fractional coverage by CO (based upon 3.2 μmol total coverage) and A is IR absorbance at 2035 cm^{-1}. The fact that the measured IR absorbance actually represents an integral over a spectrum of coverages through the catalyst pellet dictates that Eq. (2) is only valid for converting single-wavenumber absorbances into fractional coverages if a flat (position-independent)

coverage profile exists within the catalyst. However, a local equivalent of Eq. (2) which is valid for comparing model calculations to experimental data for transient operation can be obtained by making the substitution $A = 2la$ into Eq. (2) and inverting the relationship to obtain $a(\theta_{CO})$. Here, l is the pellet half-width and $a(\cdot)$ is the local absorbance which has the units of cm^{-1}. With the new inverse formulation, model calculations of $\theta_{CO}(x)$ can be converted to local absorbances $a(x)$ which can then be integrated over the thickness of the pellet to provide integral absorbances, $A(\cdot)$, which are directly comparable to experimental absorbance data.

RESULTS AND DISCUSSION

CO Adsorption and Desorption

The technique of using TIR spectroscopy to study CO coverage transients during adsorption and desorption in the absence of O_2 has several important advantages over using steady-state and transient oxidation techniques for inferring CO adsorption and desorption kinetics. First, the effects of temperature and gas-phase concentration can be directly related to CO adsorption/desorption kinetics without the necessity of unraveling the complicating details of oxygen adsorption and surface reaction. Second, for step experiments between low levels of gas-phase CO and pure He, gas-phase dynamics are unimportant because the catalyst surface responds much more slowly than does the reactor and hence the reactor gas can be assumed at quasi-steady state. Finally, most CO reactions with oxygen over supported noble metals at ambient pressure operate in regimes characterized by greater than 90% CO coverage so only a very limited range of CO coverages can be studied under reaction conditions. On the other hand, following desorption transients with TIR spectroscopy provides a simple method for studying desorption rate over the entire range of CO coverage, and hence a method for investigating the influence of CO coverage and temperature on desorption parameters.

Experiments were performed in which CO feed concentration step-changes were introduced into the reactor to probe selectively the elementary processes of CO adsorption and desorption on Rh/Al_2O_3. It has been suggested that the activation energy for CO desorption is dependent on CO coverage for Pt and Rh (Cant and Donaldson, 1981; Herz and Marin, 1980; Oh *et al.*, 1986). Temperature was used as a parameter to study this effect. The reactor feed was switched between pure He and three different CO concentrations at four different temperatures while maintaining the pressure and temperature at 900 torr and 8 l/min, respectively. Feed concentrations were 0.115%, 0.51%, and 0.90% CO and the four temperatures were 280 °C, 300 °C, 325 °C, and 350 °C.

Figure 5 shows integral IR absorbance at 2035 cm^{-1} and gas-phase CO adsorption transients for three CO concentrations at 300 °C. Figure 6 presents adsorption transients as a function of temperature for a step increase in CO concentration from 0% to 0.115%. Desorption transients are presented in Figure 7 as a function of temperature for the step down from 0.51% CO to pure He. Desorption data for the other two step decrease experiments are not presented since the form of the desorption profiles did not depend significantly on the magnitude of the decrease. Also, resolution of the gas-phase CO measurements was such that it was not possible to discern any differences in this measurement for the four different temperatures; hence only one gas-phase desorption transient is plotted. The absorbance data in Figures 5, 6 and 7 clearly are more sensitive indications of the state of the system than are the gas-phase CO measurements.

It can be seen in Figure 5 that the concentration of CO has a major effect on the adsorption profiles in the range 0.115% - 0.51% CO, but changing the height of the CO step from 0.51% to 0.90% results in little change in both the gas-phase and surface CO transients. These results suggest that internal diffusion limitation is important here since adsorption is known to be a very fast process (Oh and Hegedus, 1982; Oh *et al.*, 1986).

Equilibrium absorbances and transient profiles are functions of temperature as shown in Figure 6 for the case of 0.115% CO. However, for the other two CO concentrations, these properties did not depend on temperature (not shown). Temperature dependence of the adsorption profiles for low CO levels is a result of adsorption-desorption competition. Desorption rate depends strongly on temperature and is higher at higher temperatures. At the lower CO concentrations, adsorption, which is first-order in gas-phase CO concentration and temperature independent, is slower and thus the desorption contribution to the overall response becomes more important. The result is that at low CO levels, the net rate of CO adsorption and the equilibrium coverage depend significantly on temperature.

The adsorption/desorption model presented by Oh and Hegedus (1982) is in excellent agreement with the desorption experiments. A material balance on the gas-phase CO within the catalyst pellet yields

$$\varepsilon \frac{\partial C_{CO}}{\partial t} = D_e \frac{\partial^2 C_{CO}}{\partial x^2} + N_s \rho_p (r_d - r_a) \tag{3}$$

and for the surface

$$\frac{\partial \theta_{CO}}{\partial t} = r_a - r_d \tag{4}$$

where r_a and r_d represent the rates of CO adsorption and desorption per active site. The effective diffusivity, D_e, for CO in the catalyst pellet was estimated to be 0.025 cm^2/s by assuming the pore size distribution which was reported by Oh and Hegedus (1982) and using the random-pore model for bidisperse catalysts as detailed by Smith (1981). Similarly, a value of 0.024 cm^2/s was calculated for O_2. Here, ε is the void fraction of the pellet and was taken to be 0.59. The catalyst has density ρ_p = 1.52 g/cm^3 and and site density (based on 50% dispersion) $N_s = 2.37 \times 10^{-5}$ mol/g. These values have previously been used to describe a catalyst pellet very similar to the

one used here (Oh and Hegedus, 1982). The appropriate boundary and initial conditions are

$$\frac{\partial C_{CO}}{\partial x}(l,t) = 0 \tag{5}$$

$$C_{CO}(0,t) = 0 \tag{6}$$

$$C_{CO}(x,0) = C_{CO,o} \tag{7}$$

$$\theta_{CO}(x,0) = \theta_{CO,o} \tag{8}$$

where $\theta_{CO,o}$ is the steady-state solution of Equation 4 with C_{CO} taken as $C_{CO,o}$. The pellet half-thickness is denoted l. Only spatial-integral IR absorbances are observable with the TIR technique so the model quantity comparable to the desorption profiles is the time-dependent integral absorbance

$$A(t) = 2\int_0^l a(\theta(x,t))dx \tag{9}$$

where, as before, a( ) is the local absorbance derived from coverage calculations using the inverse of Eq. (2).

The adsorption rate of CO is proportional to the product of the impingement flux and the probability that an impingent CO molecule will become chemisorbed on the Rh surface.

$$r_a = \sigma\sqrt{\frac{RT}{2\pi M_{CO}}}S_{CO,o}C_{CO}(1-\theta_{CO}) \tag{10}$$

where σ is the inverse of the area density of sites taken to be 3.75×10^8 cm^2/mol (Oh *et al.*, 1986). The CO desorption rate is

$$r_d = k_d \exp\left[\frac{-E_d(\theta_{CO},T)}{RT}\right]\theta_{CO} \quad . \tag{11}$$

The parameters S_{CO}, k_d, and the function $E_d(\theta_{CO},T)$ are necessary to complete the model.

The use of desorption energies that depend linearly on coverage has enjoyed recent application for modeling thermal desorption as well as catalytic reaction (Bonzel and Ku, 1973; Herz and Marin, 1980; Oh *et al.*, 1986). Physically, this dependence may be related to attractive or repulsive interactions among the CO admolecules, causing desorption energy to vary with varying coverage.

It was not possible to find a single set of parameters $S_{CO,o}$, k_d, and a linear function of coverage for E_d which provide good agreement between the model and the data for all temperatures considered. Instead, agreement between the model and the experimental data was obtained using a desorption energy which varies with temperature as well as with coverage according to the parameters given in Table 1 with $E_d(\theta_{CO},T) = E_d + \alpha_{CO}\theta_{CO}$. Figure 7 shows excellent agreement between experimental data and model calculations of A(t) (solid curves) using the parameters in Table 1. Best results are obtained when $k_d = 1.0 \times 10^{14}\ s^{-1}$ which compares with $1.6 \times 10^{14}\ s^{-1}$ reported by Oh *et al.* (1986). An initial sticking probability, $S_{CO,o}$, of 0.5 was used (Oh *et al.*, 1986).

Desorption profiles were also calculated for each temperature using the desorption energy of $E_d = 31.6 - 4.5\theta_{CO}$ which was reported by Oh *et al.* (1986). Unfortunately, neither this function nor any other temperature independent function depending linearly or quadratically on θ_{CO} could adequately describe all of the data, even when k_d and $S_{CO,o}$ were allowed to vary. The desorption energy dependence presented in Table 1 is necessary to describe the experimental desorption profiles.

The modeling results are surprising for two reasons. First, and most importantly, at low temperature (<300 °C), the apparent desorption energy increases with coverage suggesting the unlikely possibility of attractive admolecule interactions. The more common observation of desorption energy decreasing with coverage was found for 350 °C. Extrapolation of the data in

Table 1 indicates that the result of Oh *et al.* (1986) would be reached at a temperature of approximately 450 °C. The second interesting observation concerns the temperature dependence on E_d. It is impossible to determine if the desorption coefficient variation with temperature is a result of the desorption energy or the pre-exponential factor since, in general, both can be expected to be functions of temperature (Taylor and Weinberg, 1978), and the mathematical form of the rate law precludes separation of the two components. Although the temperature dependence might be an intrinsic feature of the supported catalyst, another possibility is that the dependencies given in Table 1 are merely correcting for variations in IR spectra with temperature. However, the observation that maximum absorbance for the 0.90% CO adsorption experiments was not affected by temperature suggests that this explanation is unlikely. No conclusions concerning the temperature dependence in the activation energy are possible at this point without further experimentation, possibly via temperature programmed desorption spectroscopy for CO on the supported Rh catalyst.

Direct measurement of CO coverage via TIR spectroscopy during desorption from the supported Rh/Al_2O_3 catalyst has demonstrated some interesting features. Through this work, two areas for further research have been identified. They should answer the questions: (1) Why does the apparent desorption energy increase with increasing coverage for the supported catalyst?, and (2) What is the nature of the desorption rate coefficient dependence on temperature? It should be emphasized that these features can be easily overlooked while modeling steady-state oxidation data that only traverse a narrow range of CO coverages.

Steady-state Oxidation

Temperature dependence of the rate of the CO oxidation reaction in the transmission IR reactor cell at 900 torr total pressure, with an 8 l/min throughput and stoichiometric feed composition of 1.0% CO and 0.50% O_2, is presented in Figure 8. Preliminary experiments revealed that,

under similar conditions, the measured overall reaction rate increases with increasing O_2 concentration and is greatest when the CO feed rate provides stoichiometric effluent reactant ratios as used here. Since transport limitations are expected to be worst when the intrinsic rate is largest, it is reasonable that the overall rate data in Figure 8 are global reaction rates that are most likely to be affected by transport limitations. The abrupt change in apparent activation energy that occurs near 275 °C is strong evidence suggesting that transport limitations significantly influence overall rates. The steepest part of the Arrhenius plot yields an apparent activation energy of 13 kcal/mol which is approximately one half of the previous findings of 29 kcal/mol for alumina supported Rh and 30 kcal/mol for Rh(111) (Oh *et al.*, 1986).

It is useful to examine the physical differences between the catalyst wafer used here and the supported Rh/Al_2O_3 that was used by Oh *et al.* (1986). The catalyst used in that previous study consisted of 3 mm diameter alumina beads that were impregnated to a depth of approximately 30 μm at 0.01 wt. % loading and 12% dispersion. The pellet used in this study is 0.2 mm thick and loaded with approximately 0.5 wt. % Rh at 49% dispersion. These facts alone indicate that the Thiele modulus for the pellet is approximately 48 times greater than that of the beads investigated earlier. Thus, even at low temperatures, the present reactor system has much greater potential for diffusion-limited operation than does the system used previously. If at low temperatures the reaction rate is limited by internal diffusion, operating at higher temperatures produces observed reaction rates limited by the rate of external mass transport (Carberry, 1976). The regime limited by external mass transport is characterized by an apparent activation energy of 2.7 kcal/mol.

Observable moduli, ϕ_o, (Thiele moduli based on observables) were calculated for the data in Figure 8. The modulus, ϕ_o, is 1.1 at 152 °C, 5.5 at 300 °C, and 6.6 at 450 °C. Following the criterion that one should expect no serious diffusional limitations ($\eta \geq 0.7$) for $\phi_o < 1$ (Aris, 1975), it is concluded that transport limitations are almost unavoidable for CO oxidation on Rh/Al_2O_3 in

the temperature range of interest, given the TIR reactor configuration. Much lower loaded, thinner catalysts would be necessary to eliminate diffusional resistances. Although the criterion based on ϕ_o is strictly valid for first-order kinetics, ϕ_o greater than 5 indicates severe diffusional limitations for most cases of Hougen-Watson bimolecular kinetics (Roberts and Satterfield, 1966).

The catalyst and operating conditions used in this study were chosen primarily to facilitate simultaneous transmission IR and mass spectrometer measurements, thus the use of a thick wafer (for mechanical strength as well as for large adsorption capacity) and high loading of dispersed Rh. While these conditions preclude the determination of intrinsic kinetic parameters without detailed modeling of simultaneous transport and reaction, they do enable coordinated, time-resolved surface and gas-phase measurements under reaction conditions of practical interest which reveal very interesting features, even though the IR measured coverages are integral (or spatial-average) values over a position-dependent coverage profile within the pellet.

Figure 9 illustrates steady-state reaction rate dependence on the effluent CO concentration at 300 °C and 900 torr for two given oxygen effluent concentrations, 0.25% and 0.50%. The coverage data in Figure 9 were calculated from IR measurements and Eq. (2). The surface concentration of adsorbed CO (dashed curves) undergoes a transition from negligible coverage to high equilibrium coverage as the gas composition passes through the stoichiometric ratio. (The observed insensitivity of the coverage data to CO concentration indicates flat coverage profiles justifying the use of Eq. 2.)

These data do not exhibit the CO inhibition effect which was observed by Oh *et al.* (1986). The absence of a maximum rate and the lack of negative-order kinetics are not surprising in view of the significant transport resistances in this system. It is seen from Figure 9 that adsorbed CO within the catalyst pellet remains negligibly low until the bulk CO concentration exceeds twice

the bulk oxygen concentration. This result and the observed rate profiles suggest two things. First, the near zero CO surface coverage under net-oxidizing conditions implies negligible gas-phase CO concentration at the pellet surface because CO bonds strongly to Rh, and thus, if present in any significant amount at atmospheric pressure, CO would almost completely cover the metal surface and inhibit the intrinsic reaction rate. Hence, all of the CO_2 production occurs in a thin layer near the external surface of the pellet. Second, the monotonic kinetics suggest that, at 300 °C, external mass transfer controls the reaction rate until it plateaus as a result of oxygen limitation which begins near the stoichiometric ratio. Beyond the stoichiometric CO level, subsequent addition of CO to the reactor does not affect the rate and merely results in saturation of the vacant Rh sites in the pellet interior.

The 0.5% O_2 rate data in Figure 9 can be used to estimate the value for k_m, the external mass transfer coefficient. The observed reaction rate can be written

$$r_{obs} = S_p k_m (C_{CO,b} - C_{CO,s}) \tag{12}$$

and hence

$$\frac{\partial r_{obs}}{\partial C_{CO,b}} = S_p k_m \left[1 - \frac{\partial C_{CO,s}}{\partial C_{CO,b}} \right]. \tag{13}$$

where the subscripts b and s denote gas-phase quantities in the bulk and at the pellet surface, respectively. The coverage profiles in Figure 9 indicate that $\frac{\partial C_{CO,s}}{\partial C_{CO,b}} \cong 0$ for small $C_{CO,b}$. Then from the data for 0.5% O_2,

$$\lim_{C_{CO,b} \to 0} \frac{\partial r_{obs}}{\partial C_{CO,b}} \cong 319 \text{ cm}^3/\text{s} = S_p k_m. \tag{14}$$

Equation (14) indicates that $k_m \cong 51$ cm/s, a result which compares favorably with 60 cm/s which was obtained by Oh and Hegedus (1982) using 14.8 l/min flowrate in a similar reactor cell. The

true value for k_m is probably larger than 51 cm/s since the initial slope is still somewhat affected by oxygen concentration at $C_{O_2} = 0.5\%$. Also, errors associated with the assumption concerning mass spectrometer sensitivities would produce an underestimated value for k_m.

The monotonic dependence of the observed kinetics on the bulk gas-phase CO concentration is interpreted through a modeling study of the effects of internal diffusion and external mass transfer on the steady-state rate behavior for a catalyst pellet having the dimensions of the one used here. Model equations and parameters were taken from reference Oh *et al.* (1986). Briefly, CO adsorption rate is written as impingement flux times a temperature-independent sticking coefficient. CO desorption is proportional to the fractional coverage of CO with a coverage-dependent activation energy. Oxygen adsorption is first-order in vacancies and irreversible. The reaction step is of the Langmuir-Hinshelwood type and has an activation energy which depends linearly on oxygen coverage. This model and its parameters have been used successfully to describe intrinsic rate data for CO oxidation over supported and single crystal Rh catalysts. The model demonstrates strong CO inhibition similar to what has been observed for CO oxidation on Pt.

A brief description follows which summarizes the modeling technique applied to study transport effects on observed reaction rates using the Biot number, Bi, as as the manipulated variable. (Recall that $\mathrm{Bi} = \frac{k_m l}{D_e}$ is a ratio of intapellet diffusion resistance to external mass transfer resistance.) For computational simplicity, the value of 0.025 cm^2/s was used for the effective diffusivity of both CO and O_2. The steady-state material balance on CO yields

$$k_m(C_{CO,b} - C_{CO,s}) = \left[2\rho_p N_s D_e \int_0^{C_{CO,s}} r(C, \frac{1}{2}(C - C_{CO,b}) + C_{O_2,b}) dC \right]^{\frac{1}{2}}. \qquad (15)$$

where $r(C_{CO},C_{O_2})$ is the (implicitly defined) intrinsic steady-state reaction rate surface expressed as

a function of local CO and O_2 reactant concentrations. Each value of the integrand is calculated by solving the implicit, nonlinear model surface and gas-phase material balances for the intrinsic reaction rate given the local gas-phase CO and O_2 concentrations. The validity of zero as an excellent approximation for the pellet center-line CO concentration (the lower limit for the integral) was verified by employing solutions of the appropriate complete boundary value problem. Note that oxygen dependence is explicitly accounted for in the integrand. Equation (15) can be solved to find $C_{CO,s}$ for given values of $C_{CO,b}$ and $C_{O_2,b}$ and the result can be inserted into Eq. (12) to calculate the observed rate as a function of the bulk CO concentration. Care must be taken to change the lower integration limit for calculations made in the oxygen limited regime. Given bulk oxygen and carbon monoxide concentrations, the integral can be calculated numerically until it and the external transport term are equal, at which point the pellet surface CO concentration, $C_{CO,s}$, will be determined. The curves in Figure 10 were calculated following this procedure with $C_{O_2,b}$ = 0.5%, T = 300 °C and the pressure at 900 torr. The Biot number was computationally manipulated by changing k_m.

The model study in Figure 10 shows an important result. Qualitatively, a wide range of observed kinetics can result for strongly inhibited reactions, depending on Bi. For low Bi (*i.e.*, external mass transfer control), monotonic kinetics are expected. As Bi increases, a maximum in the observed rate appears and its position moves to lower values of $C_{CO,b}$. Although not presented in Figure 10, the effectiveness factor for Bi = 92 and $C_{CO,b}$ = 1% is 0.06. For the catalyst pellet used in these experiments, Bi ≅ 24 and the model and the data show qualitative disagreement. The model does not exhibit an intrinsic reaction rate that is large enough to produce essentially zero gas-phase CO concentration as observed experimentally. The model shows, however, that monotonic kinetics are possible for sufficiently low Bi. A model with higher intrinsic reaction rate would shift the monotonic kinetics to higher Bi. No attempt was made to evaluate better

model parameters for the steady-state rate data because of the difficulties associated with estimation of multiple parameters from limited data for a distributed system.

Transient Oxidation

Figure 11 presents transient CO_2 production and CO coverage data for step- changes in feed composition across stoichiometric conditions. Figure 11a shows the step-up from a lean (net-oxidizing) feed of 0.25% CO and 0.25% O_2 (balance He) to a rich (net-reducing) feed of 1.4% CO and 0.25% O_2. Figure 11b shows the reverse rich-to-lean step experiment. The switches occurred at t=5 s in both cases. Both reactor feedstreams and downstream pressure drop on the bypass line were carefully balanced to avoid pressure surges during switching, thus eliminating pressure imbalances as an explanation for the CO_2 spikes in Figure 11.

The overshoot in CO_2 production in Figure 11a results from the conversion of gas-phase and surface oxygen that was stored within the catalyst pellet relative to the final steady-state intrapellet oxygen distribution at the CO rich conditions. Similarly, the smaller spike for the rich-to-lean experiment results when stored CO is converted to CO_2 as the catalyst comes to the new steady-state conditions. Residual gas-phase reactants probably do not contribute significantly to the observed peaks since the mean residence time of the reactor, 0.008 s, is much smaller than the duration of the peaks as seen in Figure 11 (the response for a step-change to a CSTR reaches 63% of its final value in one time constant).

The differences in the two peak heights can be rationalized in terms of the relative magnitudes of the sticking coefficients and gas fluxes for the two reactants. During lean operation, the catalyst interior becomes saturated with oxygen. This oxygen becomes available for reaction when the switch to a rich feed occurs. Initially, the reaction rate depends on the CO sticking coefficient, CO flux, and external mass transport and is relatively large because of the abundance

of reactive oxygen at the pellet surface. The rate then quickly falls off as easily accessible oxygen is consumed, and the diffusion of CO into the catalyst controls the rate until all stored oxygen disappears. At this point the catalyst becomes nearly saturated with CO and operates in a steady-state regime characteristic of an oxygen-limited process. Subsequent switch to lean conditions allows the stored CO to react. However, since the oxygen sticking coefficient is much smaller than that for CO (Oh *et al.*, 1986), and the oxygen flux is estimated to be 5.6 times smaller (based on the ratio of partial pressures) than the CO flux during the rich conditions, the resultant burst of CO_2 is accordingly much smaller.

An elbow in the CO coverage trajectory for the lean-to-rich switch (Figure 11a) appears just as the CO_2 peak diminishes. The subsequent slow approach to the steady-state CO coverage is accompanied by a slow decline in CO_2 production. This approach to steady-state is significantly slower than CO adsorption in the absence of oxygen (Figure 5). The fast response of the surface (as viewed by IR absorbance measurements) during the rich-to-lean switch (Figure 11b) relative to the desorption trajectories in Figure 7 suggests that the reaction step is much faster than CO desorption at 300 °C.

The existence of the CO_2 production peaks for step-changes across stoichiometric reactant conditions suggests the possibility of improving the time-average CO conversion by forced cycling. Enhancement of CO conversion has previously been observed over three-way automotive catalysts during step changes in feedstream composition (Herz *et al.*, 1983; Schlatter and Mitchell, 1980). Figure 12 presents results from cycled feedstream experiments. In each case, the periodic behavior observed after several cycles of feed forcing is shown. Initial transients are not indicated. Feed compositions were those used for the step experiments described above, and the cycling periods, τ, were 2s, 4s, and 8s. Net-reducing and net-oxidizing feeds were each applied for one-half of the cycling period.

Table 2 contains time-average CO_2 production rates and time-average CO coverages for the forcing periods that were tested. Relevant limiting cases are presented for comparison. The value for very large periods relative to all system response times is sometimes referred to as the quasi-steady-state limit and was calculated by simply averaging the two steady-state rates corresponding to the two input feed compositions (Bailey, 1977). In the other extreme, as τ approaches values very small compared to all system response times, the rate and coverage will approach the values corresponding to steady-state operation at the mean feed composition (Bailey, 1977). The time-average coverages in Table 2 were derived from the application of Eq. 2 to A(t) data and hence only the qualitative trends are meaningful.

It is seen from Table 2 that average CO_2 production rate increases with decreasing cycling period over the range of periods studied. In fact, for τ = 2 s, the time-average rate is equal to the estimated steady-state rate at the time-average feed composition, and is apparently already at the relaxed steady-state asymptote. The expected time-average reaction rate in the limit of very fast cycling was estimated as follows. The time-average feed composition is 0.875% CO and 0.25% O_2 which is well above the stoichiometric ratio and probably in the flat section of the diffusion-limited observed rate curve for an oxygen feed of 0.25% (cf. Figure 6). Hence the observed reaction rate at the time-average feed composition is probably near, but certainly less than, 10.8 μmol/s which was observed for the CO rich feedstream.

Although results for cycling periods shorter than 2 s were not obtained, the fact that time-average CO coverage is highest for the smallest periods studied does not bode well for the possibility of rate enhancement by cycling. Still, the transient CO_2 trajectories during cycling suggest the possibility of rate enhancement by some cycling scheme, and it is still a matter for speculation and further investigation, possibly using duty-fraction as another variable (Taylor and Sinkevitch, 1983).

A Note on Autonomous Oscillations

During attempts to collect steady-state kinetic data at 200 °C, sustained autonomous oscillations were discovered. Figure 13 displays CO_2 production rates and IR absorbances that resulted when two different steady streams were fed to the reactor operating at 200 °C and 900 torr. From these limited data it appears that oscillation frequency increases with increasing O_2 concentration. No oscillations were observed for the reactor operating at 300 °C. As was observed for CO oxidation on Pt (Kaul and Wolf, 1985), Figure 13 shows that net decreases in CO_2 production occur simultaneously with net increases in the average CO surface coverage within the wafer. This could be a result of localized intrinsic rate inhibition by adsorbed CO, but because of the complex, coupled transport and reaction processes that might be involved here, (including possibly significant temperature gradients across the pellet), detailed interpretation of the transient profiles is difficult. The oscillations reported here are qualitatively similar to another report of CO oxidation oscillations on supported Rh (Tufan and Lintz, 1983).

Sustained oscillations for CO oxidation on platinum metals have been reported many times for single crystal, unsupported polycrystalline, and supported polycrystalline catalysts (e.g., Ertl *et al.*, 1982; Lynch and Wanke, 1984; Sales *et al.*, 1982; Scheintuch and Schmitz, 1977). Several different hypotheses and models have been proposed to account for these observations (Jensen and Ray, 1982; Lynch *et al.*, 1986; Pikios and Luss, 1977; Slin'ko and Slin'ko; 1978) but no general, comprehensive theory has yet emerged. Transmission IR spectroscopy can be a valuable tool for correlating surface coverage with gas-phase concentrations during autonomous oscillations.

Recently, Kaul and Wolf (1984,1985) used Fourier transform transmission infrared spectroscopy in conjunction with a very sensitive foil thermocouple to study CO oxidation over a Pt/SiO_2 catalyst wafer in a reactor very similar to the one used here. By masking areas of the

catalyst and using several thermocouples, Kaul and Wolf were able to characterize the onset of oscillations by the onset of inhibition and by the transition from a regime of spatially uniform operation (no spacial variation over the pellet) to a regime of nonuniform operation where localized hot spots coexist with catalyst regions that are cooler (sections where the rate is inhibited by CO). In addition, these researchers found that mixing within their reactor cell played an important role in the dynamic behavior of the system. In fact, oscillations were altered severely when Kaul and Wolf (1986) added an external recycle loop to their TIR cell. Similar behavior is expected for the Rh/Al_2O_3 catalyst and reactor cell used here. It is impossible to deduce the cause of the observed oscillations. However, the similarity between this apparatus and that of Kaul and Wolf suggests that complex kinetic/transport interactions might be important.

SUMMARY

The experimental and modeling results presented above are summarized as follows:

1. TIR spectra of CO chemisorbed on 0.5% Rh/Al_2O_3 demonstrate irreversible change in the nature of the catalyst as a result of catalyst use in a reactive environment. Initially the Rh primarily supports dicarbonyl CO but eventually stabilizes in a state characterized by a more linearly bound CO adlayer.

2. TIR absorbance measurements during transient adsorption and desorption studies at several temperatures in the range 280-350 °C exhibit interesting temperature and coverage dependent behavior which is significantly different from what has been previously reported for unsupported catalysts.

3. Surface CO measurements and simultaneous gas-phase CO_2 measurements during CO oxidation over a range of temperatures (150-450 °C) and CO concentrations (up to 1.5% CO at 900 torr) demonstrate the importance of accounting for internal and external mass transfer

limitations in interpreting the results of typical TIR spectroscopic studies.

4. Transient step and forced cycling operation across stoichiometric conditions produce peaks in CO_2 production that are a result of O_2 and CO storage within and on the catalyst pellet.

NOTATION

A	Integral IR absorbance at 2035 cm^{-1}
$a(\cdot)$	Local IR absorbance at 2035 cm^{-1}
Bi	Biot number, $\frac{k_m l}{D_e}$
C	Gas-phase concentration, mol/cm^3
D_e	Effective diffusivity, cm^2/s
E_d	Desorption energy, kcal/mol
h_T	Thiele modulus
I	Mass spectrometer signal intensity
$\hat{k}$	Arbitrary (pseudo-)first-order rate coefficient
k_d	Desorption pre-exponential, s^{-1}
k_m	External mass transfer coefficient, cm/s
l	Pellet halfwidth, cm
M_{CO}	Molecular weight of CO, g/mol
N_s	Catalyst site density, mol sites per gram of catalyst
R	Universal gas constant
$r(C_{CO},C_{O_2})$	Intrinsic reaction rate, s^{-1}
r_a	Adsorption rate, s^{-1}
r_d	Desorption rate, s^{-1}
r_{obs}	Observed reaction rate, s^{-1}
$S_{CO,o}$	Initial CO sticking probability
S_g	Specific area, cm^2/g
S_p	Total external pellet surface area, cm^2
T	Temperature, K
t	Time, s
t_o	Time for onset of titration experiment, s
x	Position along pellet axis, cm
ε	Pellet void fraction
η	Effectiveness factor
θ	Fractional coverage
$\hat{\theta}$	Spatial-average surface coverage
ρ_p	Pellet density
σ	Inverse area density of sites, cm^2/mol
τ	Forcing period, s; Arbitrary long time for stabilization, s
ϕ_o	Observable modulus

sub- and superscripts

b	Bulk
CO	Carbon monoxide
e	eventual
O_2	Oxygen
o	Initial value
s	External pellet surface
40	m/e 40 (Ar)
44	m/e 44 (CO_2)

REFERENCES

1. Aris, R. *The Mathematical Theory of Diffusion and Reaction in Permeable Catalysts, Vol. 1;* Oxford University Press: London, 1975.
2. Bailey, J. E. In *Chemical Reactor Theory: A Review* L. Lapidus and N. R. Amundson, Eds.; Prentice-Hall, 1977; p 758.
3. Barshad, Y., Zhou, X., and Gulari, E. *J. Catal.* **1985,** *94,* 128.
4. Bonzel H. P. and Ku R. *Surface Sci.* **1973,** *40,* 85.
5. Cant, N. W. and Donaldson, R. A. *J. Catal.* **1981,** *71,* 320.
6. Carberry, J. J., *Chemical and Catalytic Reaction Engineering;* McGraw Hill, Inc.: New York, 1976.
7. Cavanagh, R. R. and Yates, Jr., J. T. *J. Chem. Phys.* **1981,** *74,* 4150.
8. Elhaderi, A. E. and Tsotsis, T. T. *Chemical Reaction Engineering - Boston;* J. Wei and C. Georgakis, Eds.; American Chemical Society: Washington, 1982; Symposium Series 196, p 77.
9. Ertl, G., Norton, P. R., and Rustig, J. *Phys. Rev. Letters* **1982,** *49,* 177.
10. Haaland, D. M. and Williams, F. L. *J. Catal.* **1982,** *76,* 450.
11. Herz, R. K., Kiela, J. B., and Sell, J. A. *I. & E. C. Prod. Res. Dev.* **1983,** *22,* 387.
12. Herz, R. K. and Marin, S. P. *J. Catal.* **1980,** *65,* 281.
13. Jensen, K. F. and Ray, W. H. *Chem. Engng. Sci.* **1982,** *37,* 1387.
14. Kaul, D. J. and Wolf, E. E. *J. Catal.* **1984,** *89,* 348.
15. Kaul, D. J. and Wolf, E. E. *J. Catal.* **1985,** *91,* 216.
16. Kaul, D. J. and Wolf, E. E. *Chem. Engng. Sci.* **1986,** *41,* 1101.
17. Lynch, D. T., E. Gerhard, and Wanke, S. E. *J. Catal.* **1986,** *97,* 456.
18. Lynch, D. T. and Wanke, S. E. *J. Catal.* **1984,** *88,* 333, 345.
19. Oh, S. H., and Carpenter, J. E. *J. Catal.* **1983,** *80,* 472.
20. Oh, S. H., Fisher, G. B., Carpenter, J. E., and Goodman, D. W. *J. Catal.* **1986,** *100,* 360.
21. Oh, S. H. and Hegedus, L. L. *Catalysis under Transient Conditions;* A. T. Bell and L. L. Hegedus, Eds.; American Chemical Society: Washington, 1982; Symposium Series 178, p 79.
22. Pikios, L. A. and Luss D. *Chem. Engng. Sci.* **1977,** *32,* 191.
23. Primet, M. J. *J. Chem. Soc.; Faraday Trans.* **1978,** *74,* 2570.
24. Rice, C. A., Worley, S. D., Curtis, C. W., Guin, J. A. and Tarrer, A. R. *J. Chem. Phys.* **1981,** *74,* 6487.
25. Roberts, G. W., and Satterfield, C. N. *I. & E. C. Fundam.* **1966,** *5,* 317.

26. Sales, B. C., Turner, J. E., and Maple, M. B. *Surface Sci.* **1982,** *114,* 381.

27. Scheintuch, M. and Schmitz, R. A. *Catal. Rev.-Sci. Eng.* **1977,** *15,* 107.

28. Schlatter, J. C. and Mitchell, P. J. *I. & E. C. Prod. Res. Dev.* **1980,** *19,* 288.

29. Slin'ko, M. G. and Slin'ko, M. M. *Catal. Rev.-Sci. Eng.* **1978,** *17,* 119.

30. Smith, J. M. *Chemical Engineering Kinetics;* McGraw-Hill Inc: New York, 1981.

31. Taylor, C. K. C. and Sinkevitch, R. M. *I. & E. C. Prod. Res. Dev.* **1983,** *22,* 45.

32. Taylor, J. L. and Weinberg, W. H. *Surface Sci.* **1978,** *78,* 259.

33. Tufan, G. and Lintz, H. G. *Proceedings of the 5th International Symposium on Heterogeneous Catalysis, Varna, Part II;* 1983.

34. UTI Spectrometer; published data.

35. Yates, Jr., J. T., Duncan, T. M., Worley, S. D. and Vaughan, R. W. *J. Chem. Phys.* **1979,** *67,* 1219.

Table 1. Desorption energy parameters required for accurate modeling of transient desorption using the relationship $E_d(\theta_{CO},T) = E_d + \alpha_{CO}\theta_{CO}$.

T (°C)	E_d (kcal/mol)	α_{CO} (kcal/mol)
280	26.15	1.8
300	26.6	1.0
325	27.15	0.0
350	27.7	-1.0

Table 2. Time-average results from cycled feedstream experiments (periods 2, 4, and 8 s) and calculated from asymptotic theory for periods approaching zero and infinity.

Period, τ (sec)	Time-average CO_2 production rate, $\bar{r}$ (μmol/s)	Approximate time-average CO coverage
0	10.8	0.78
2	10.8	0.55
4	10.4	0.44
8	10.0	0.38
∞	9.2	0.39

FIGURE CAPTIONS

1. IR spectra for CO on Rh/Al_2O_3. (a) Fresh catalyst saturated at 250 °C. (b) Same catalyst after 30 min treatment in O_2 at 250 °C. (c) Saturated at 300 °C. (d) Oxidized and again saturated at 300 °C. (e) stabilized catalyst at 300 °C.
2. IR spectra as function of coverage at 300 °C for the stabilized catalyst. The largest peak indicates the saturated catalyst and corresponds to 1% CO in He. The other spectra correspond to different levels of gas-phase CO, all of which are less than 0.1% (in He).
3. IR absorbance calibration at 2035 cm^{-1} and 300 °C. The solid line corresponds to $P = 0.57 + 25.6A^2 + 1.09A$ where P is CO_2 production in μmol and A is IR absorbance at 2035 cm^{-1}.
4. Typical titration data showing IR absorbance at 2035 cm^{-1} and mass spectrometer intensities at m/e = 44 (CO_2) and m/e = 40 (Ar). The abscissa shows time beginning 2 sec before the switch to O_2.
5. Transient adsorption data at 300 °C illustrating the effects of gas-phase CO concentration following step changes in feed composition. ——— 0.115% CO, – – – – – 0.51% CO, ····· 0.90% CO.
6. Transient adsorption data showing the effects of temperature for a step increase in CO concentration of 0.115%. – – – – – 280 °C, ——— 300 °C, · · · · · · 325 °C, —·— 350 °C.
7. Transient desorption data (noisy) and model results (smooth) for four temperatures and a step decrease in CO concentration of 0.51%. The gas-phase CO profile normalized with the 0.51% CO step height is indicated with a solid curve.
8. Arrhenius plot of rate data for 1% CO and 0.50% O_2 stoichiometric reactor conditions.
9. Steady-state rate data for 0.50% O_2 and 0.25% O_2 in the reactor effluent at 300 °C. Solid curves indicate CO_2 production and dashed curves indicate CO coverage. Triangles are for 0.5% O_2 and squares indicate the 0.25% O_2 data.
10. Calculated effect of the Biot number, Bi, on observed rate for 0.50% O_2 at 300 °C.
11. Transients for step changes across the stoichiometric point at 300 °C. (a) Lean-to-rich: 0.25% CO and 0.25% O_2 switched to 1.4% CO and 0.25% O_2 in the reactor feed. (b) Rich-to-lean: 1.4% CO and 0.25% O_2 switched to 0.25% CO and 0.25% O_2. Dashed curves indicate integral absorbances at 2035 cm^{-1} and solid curves indicate CO_2 production.
12. Cycled feedstream data at 300 °C. (a) Period = 2 s. (b) Period = 4 s. (c) Period = 8 s. Solid curves indicate CO_2 production and dashed curves indicate integral absorbances at 2035 cm^{-1}.
13. Experimentally observed sustained autonomous oscillations at 200 °C. (a) CO_2 production and (b) IR absorbance at 2035 cm^{-1} for a lean feed containing approximately 0.25% O_2. (c) CO_2 production and (d) Integral IR absorbance at 2035 cm^{-1} for a lean feed containing approximately 0.50% O_2.

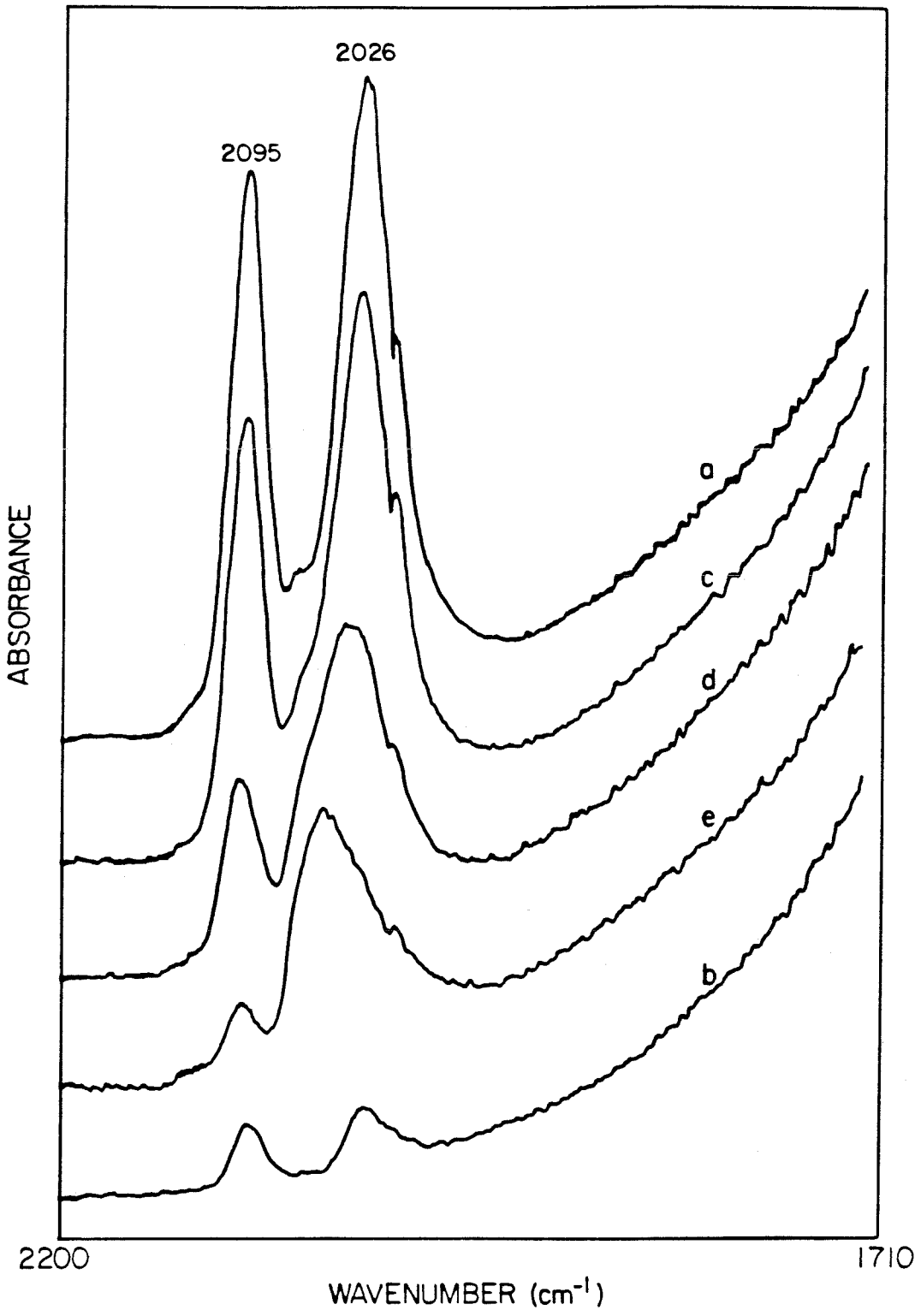

Figure 1

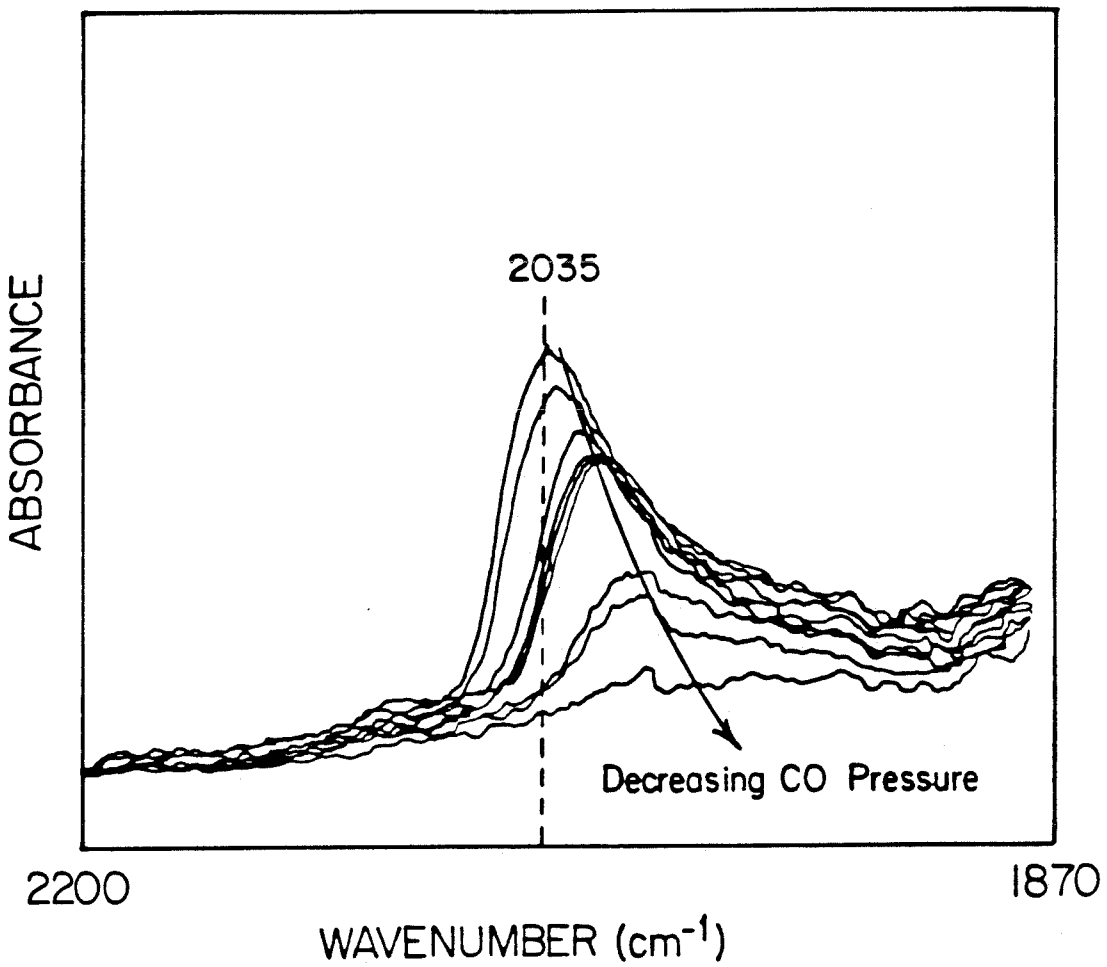
2035
ABSORBANCE
Decreasing CO Pressure
2200
1870
WAVENUMBER (cm-1)

Figure 2

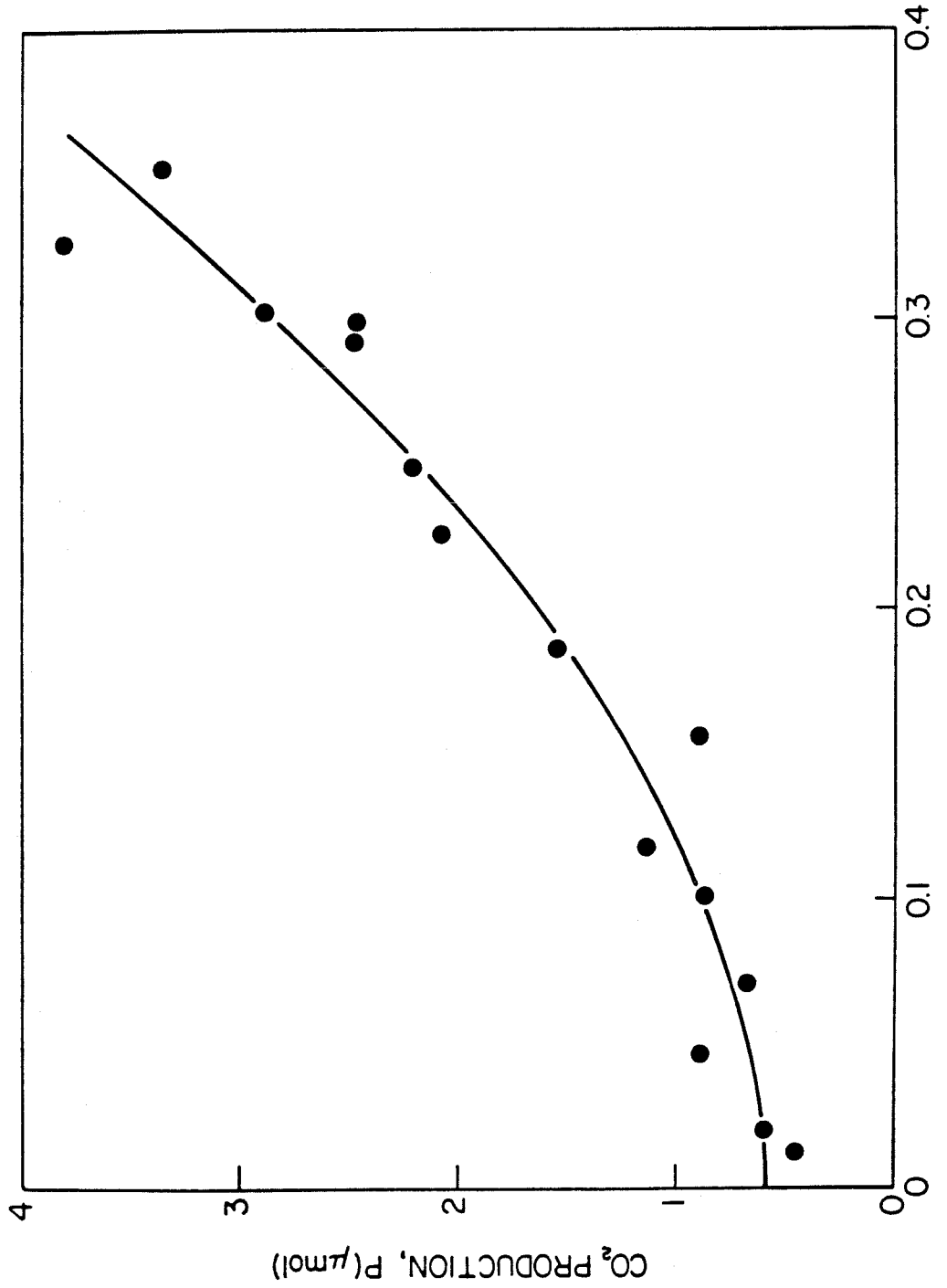
CO2 PRODUCTION, P(μmol)
0
1
2
3
4
0
0.1
0.2
0.3
0.4
IR ABSORBANCE, A (at 2035 cm-1)

Figure 3

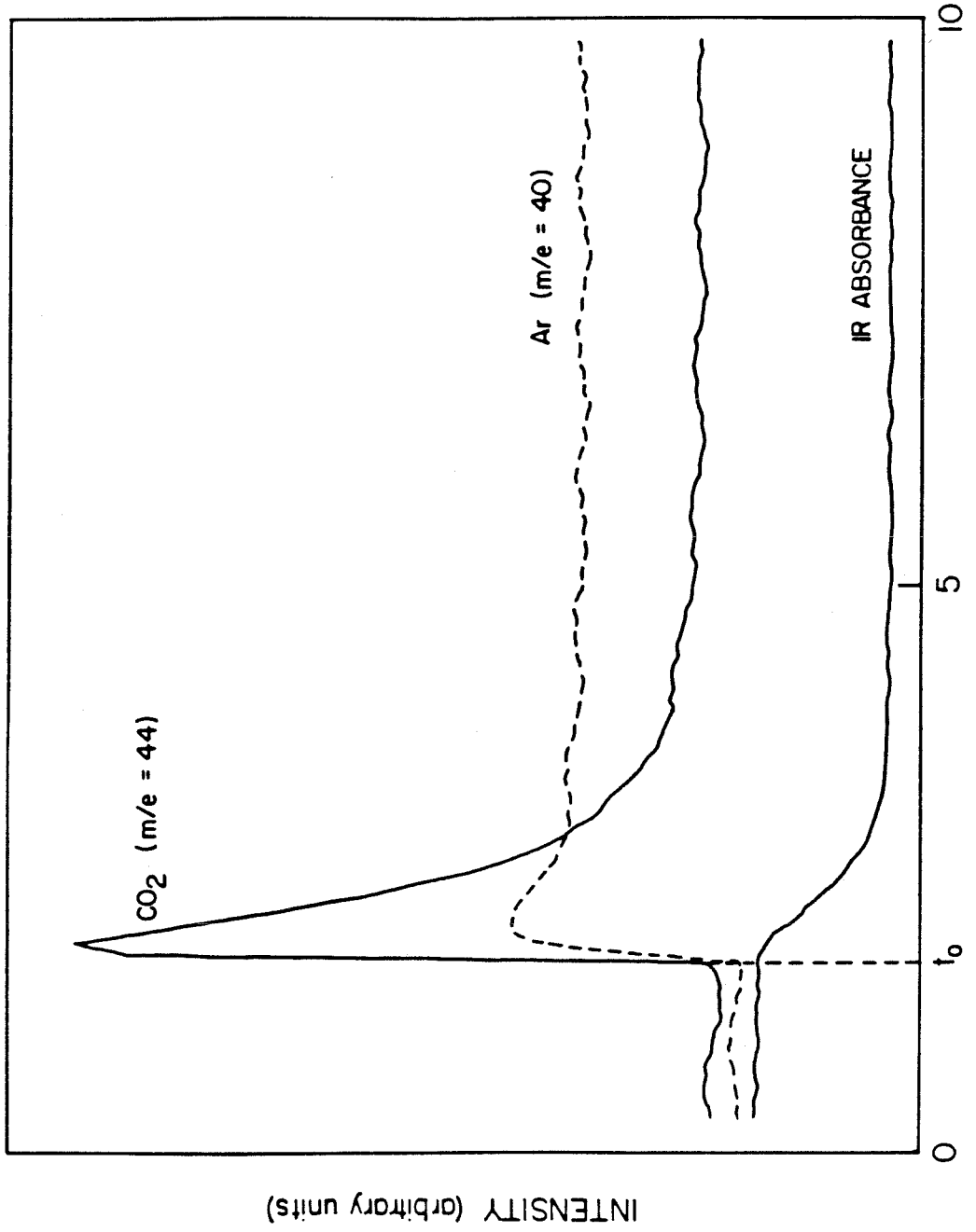
CO_2 (m/e = 44)
Ar (m/e = 40)
IR ABSORBANCE
t_o
0
5
10
TIME (sec)
INTENSITY (arbitrary units)

Figure 4

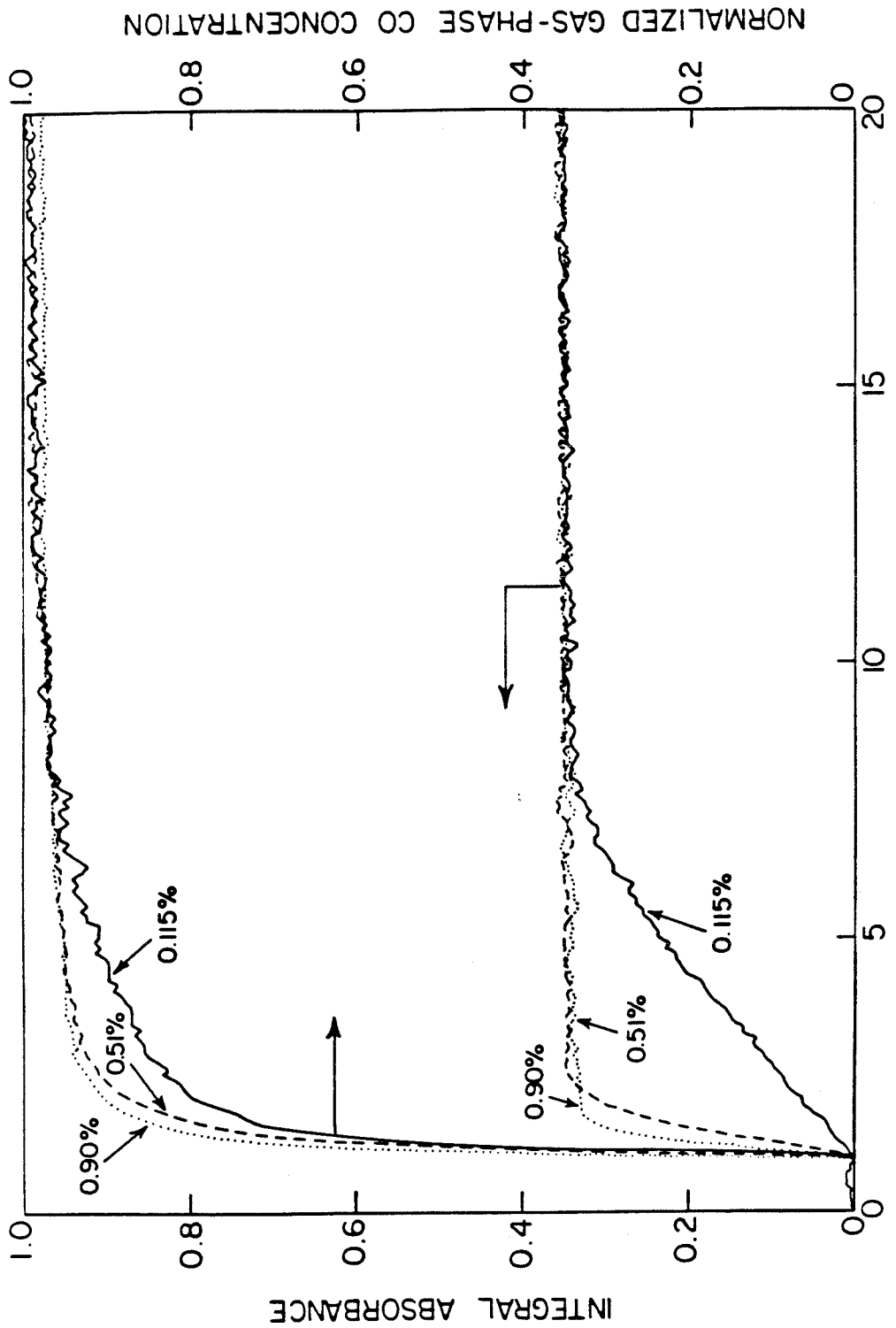
NORMALIZED GAS-PHASE CO CONCENTRATION
INTEGRAL ABSORBANCE
TIME (sec)
0.115%
0.51%
0.90%
0.115%
0.51%
0.90%
0
0.2
0.4
0.6
0.8
1.0
5
10
15
20

Figure 5

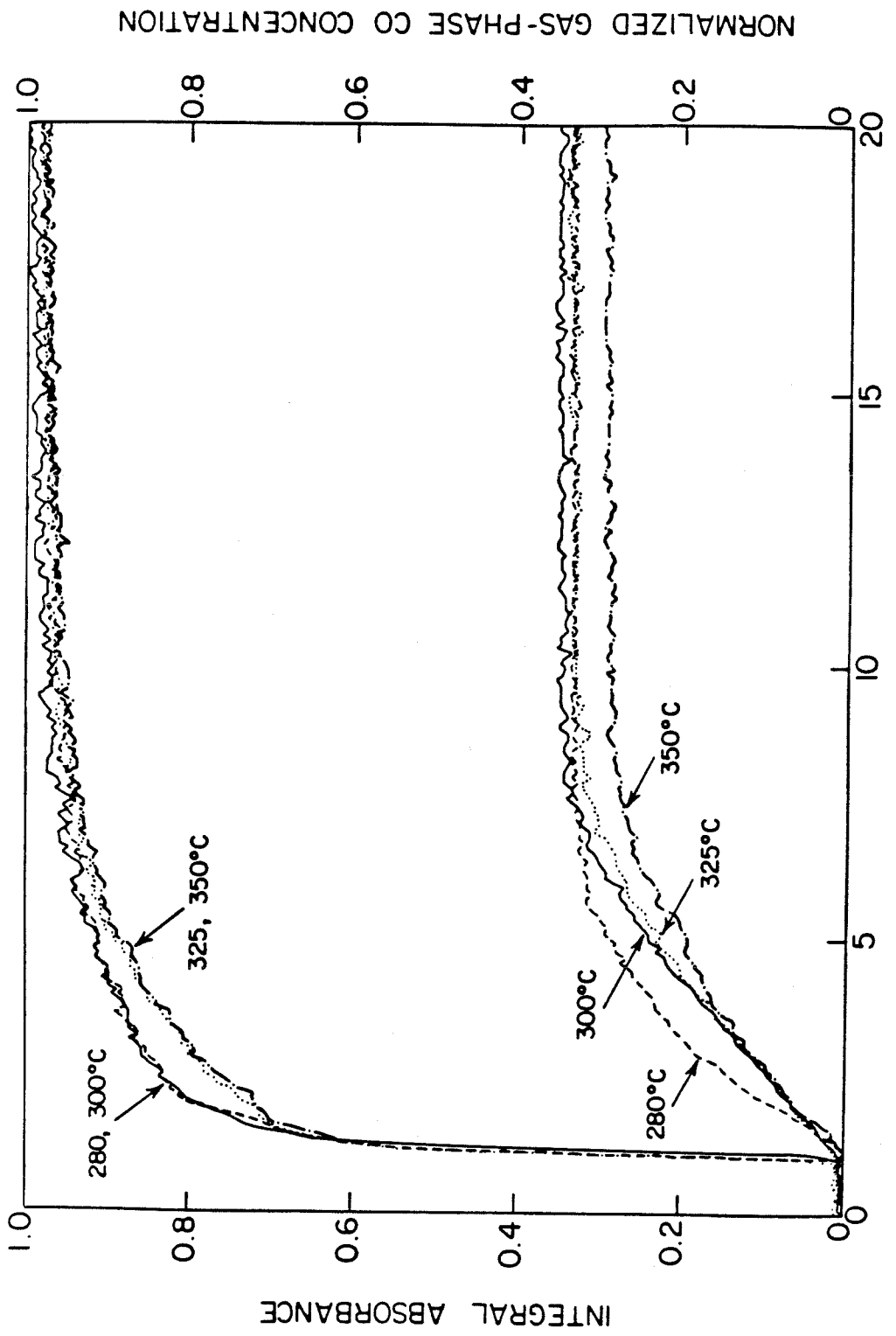
NORMALIZED GAS-PHASE CO CONCENTRATION
INTEGRAL ABSORBANCE
TIME (sec)
280, 300°C
325, 350°C
280°C
300°C
325°C
350°C

Figure 6

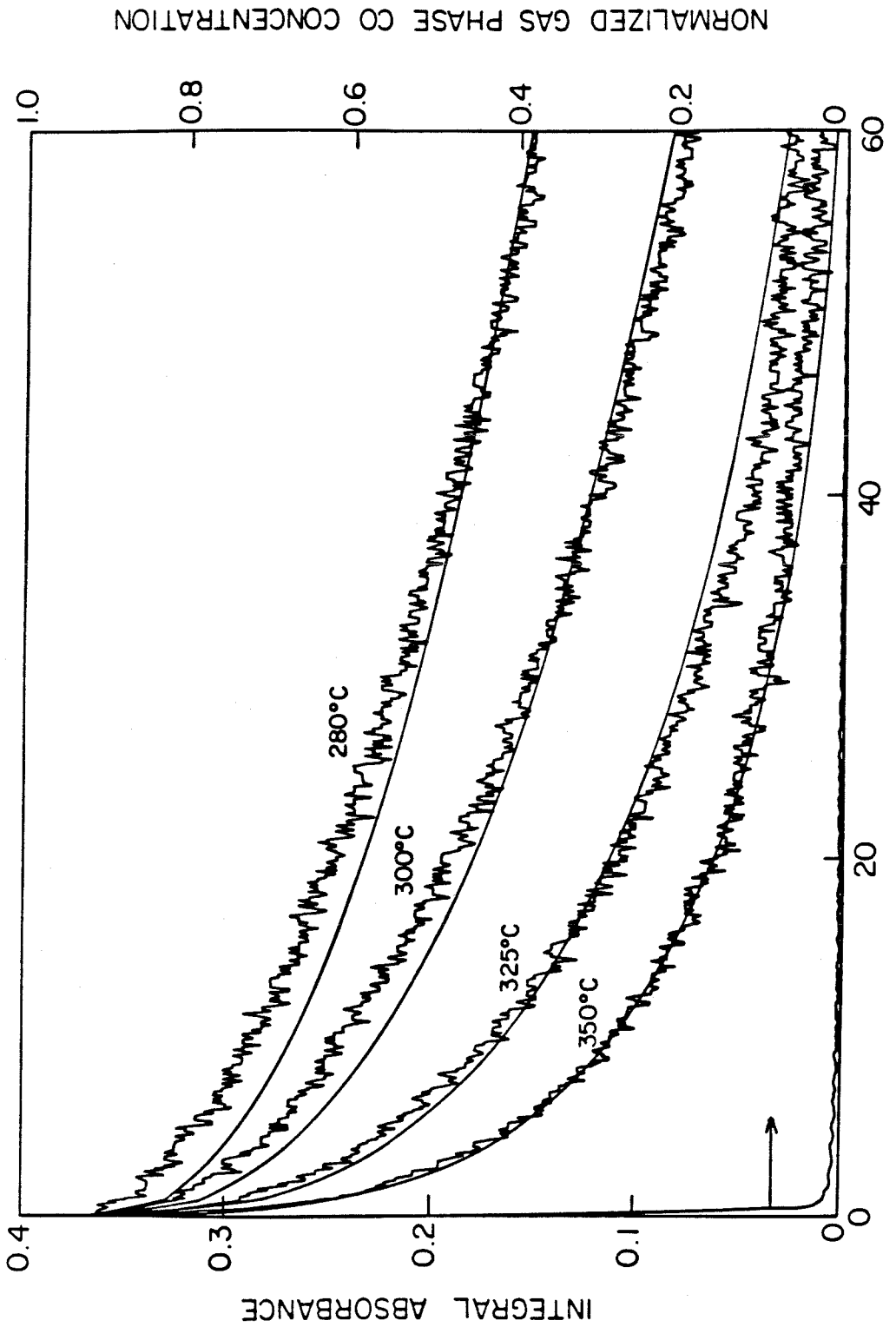
NORMALIZED GAS PHASE CO CONCENTRATION
1.0
0.8
0.6
0.4
0.2
0
60
40
20
0
TIME (sec)
0.4
0.3
0.2
0.1
0
INTEGRAL ABSORBANCE
280°C
300°C
325°C
350°C

Figure 7

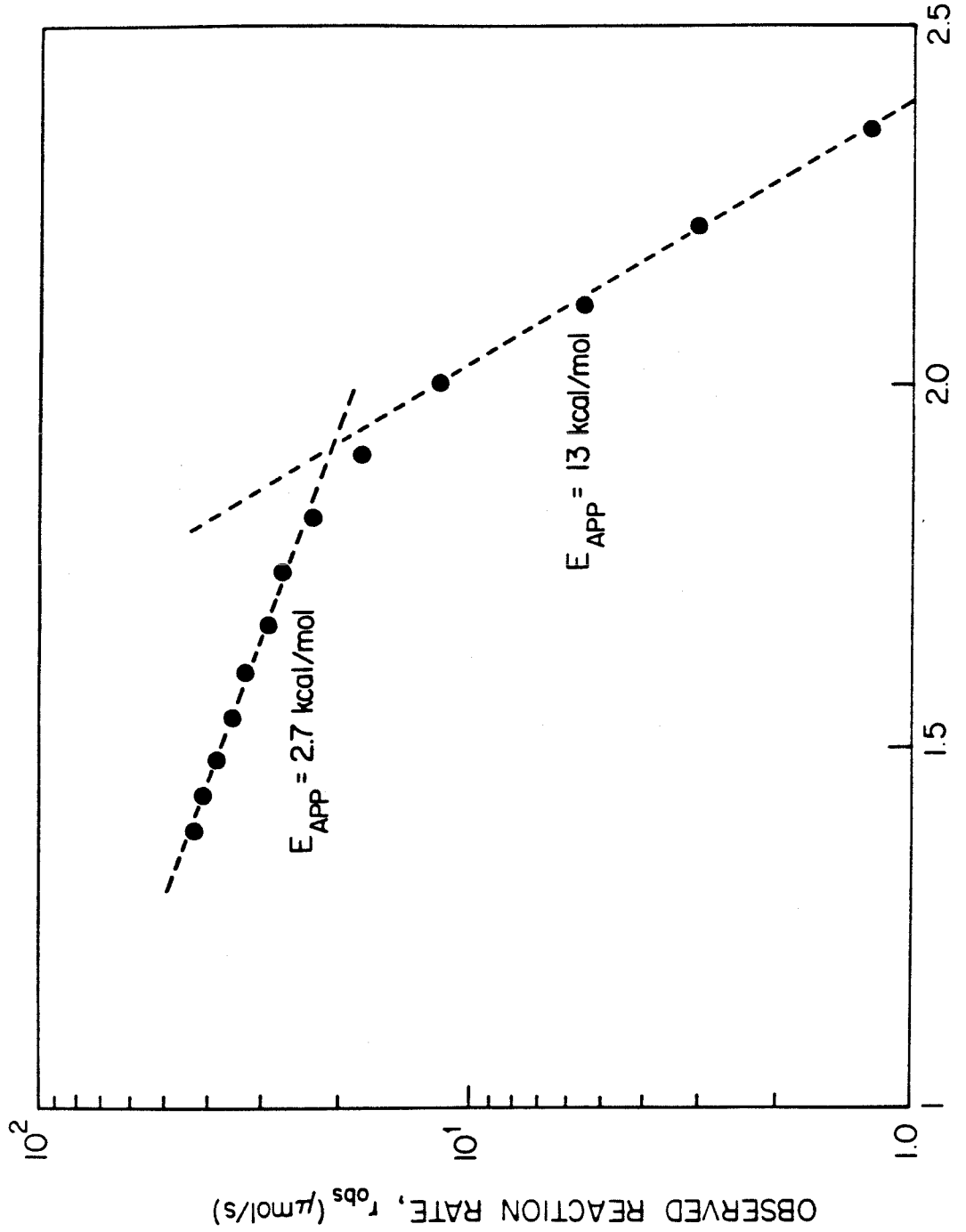
OBSERVED REACTION RATE, r_{obs} (μmol/s)
10^2
10^1
1.0
1.5
2.0
2.5
1000/T (K^{-1})
E_{APP} = 2.7 kcal/mol
E_{APP} = 13 kcal/mol

Figure 8

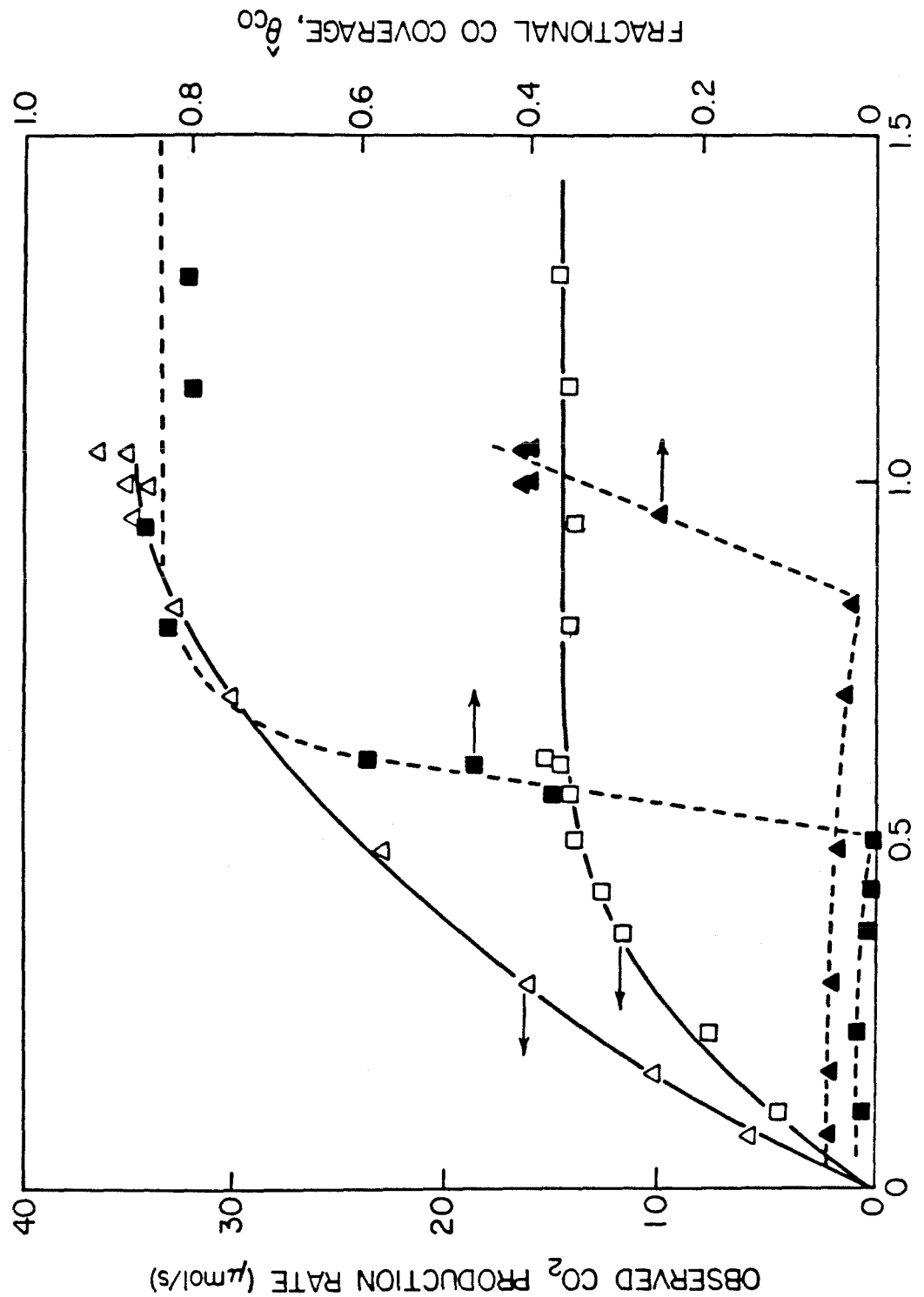
OBSERVED CO_2 PRODUCTION RATE (μmol/s)
FRACTIONAL CO COVERAGE, θ_{CO}
EFFLUENT CO CONCENTRATION (%)
0
10
20
30
40
0.2
0.4
0.6
0.8
1.0
0.5
1.0
1.5

Figure 9

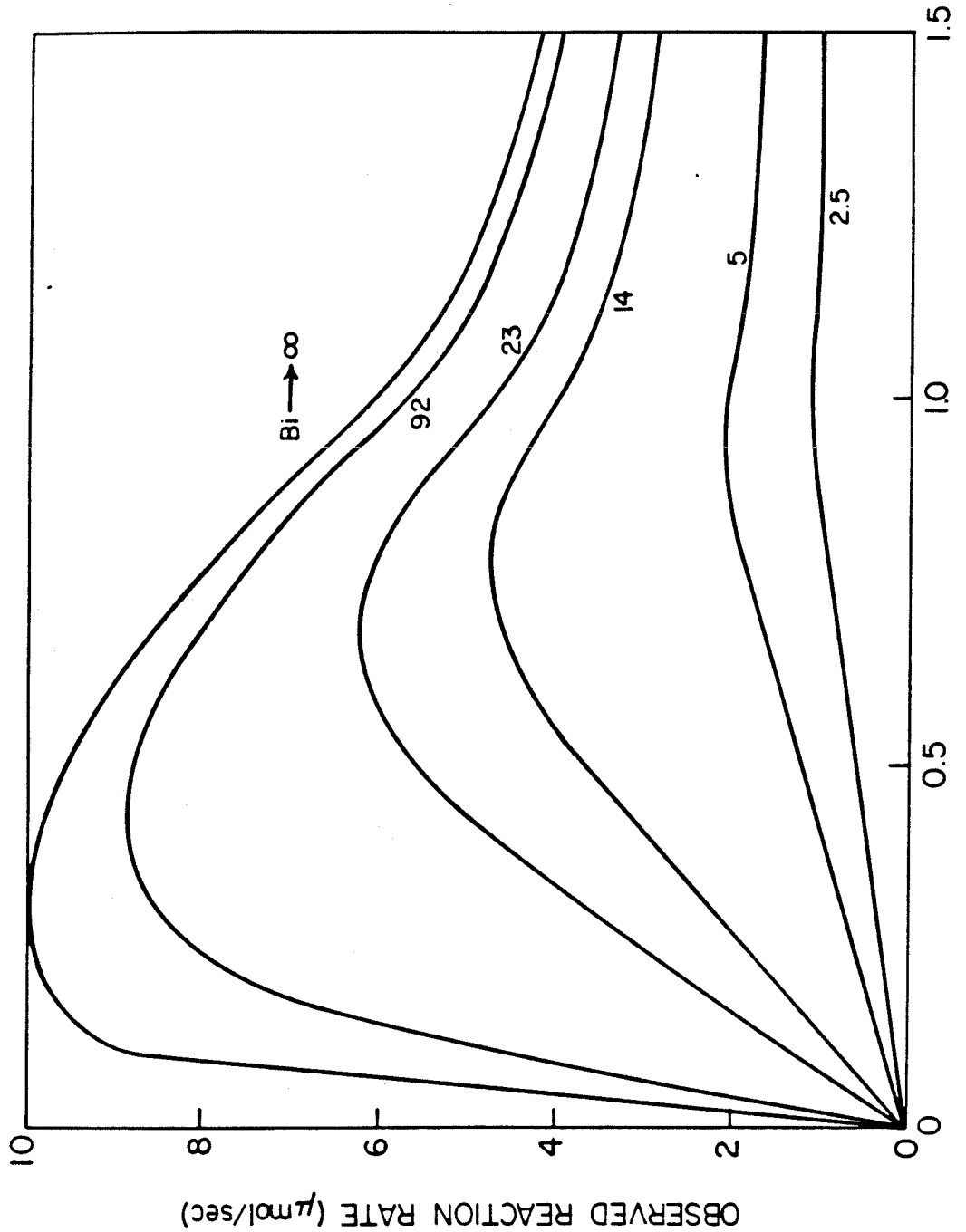
OBSERVED REACTION RATE (μmol/sec)
0
2
4
6
8
10
0
0.5
1.0
1.5
CO CONCENTRATION (%)
Bi → ∞
92
23
14
5
2.5

Figure 10

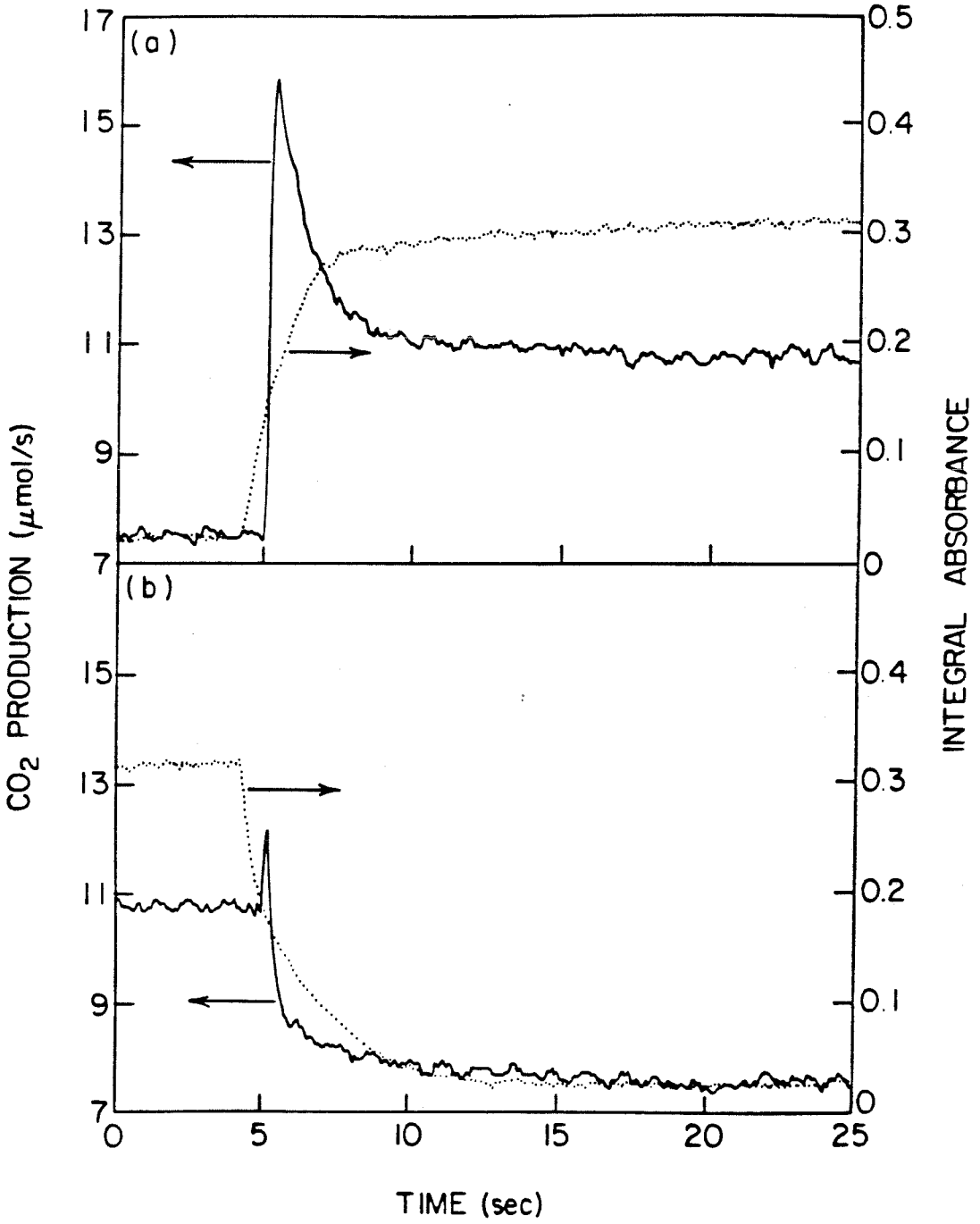
(a)
(b)
17
15
13
11
9
7
0.5
0.4
0.3
0.2
0.1
0
0
5
10
15
20
25
CO_2 PRODUCTION (μmol/s)
INTEGRAL ABSORBANCE
TIME (sec)

Figure 11

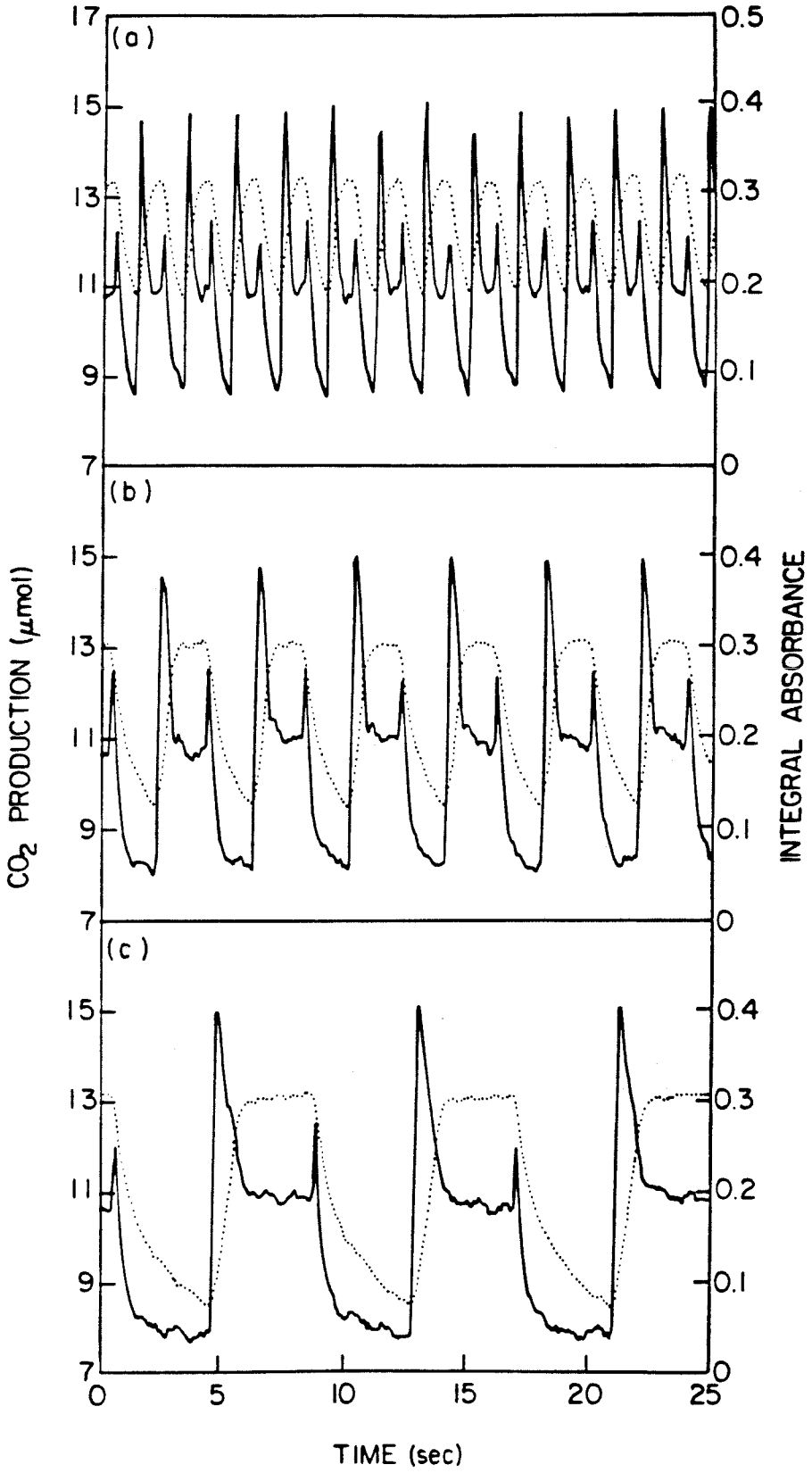
(a)
(b)
(c)
17
15
13
11
9
7
0.5
0.4
0.3
0.2
0.1
0
0
5
10
15
20
25
TIME (sec)
CO_2 PRODUCTION (μmol)
INTEGRAL ABSORBANCE

Figure 12

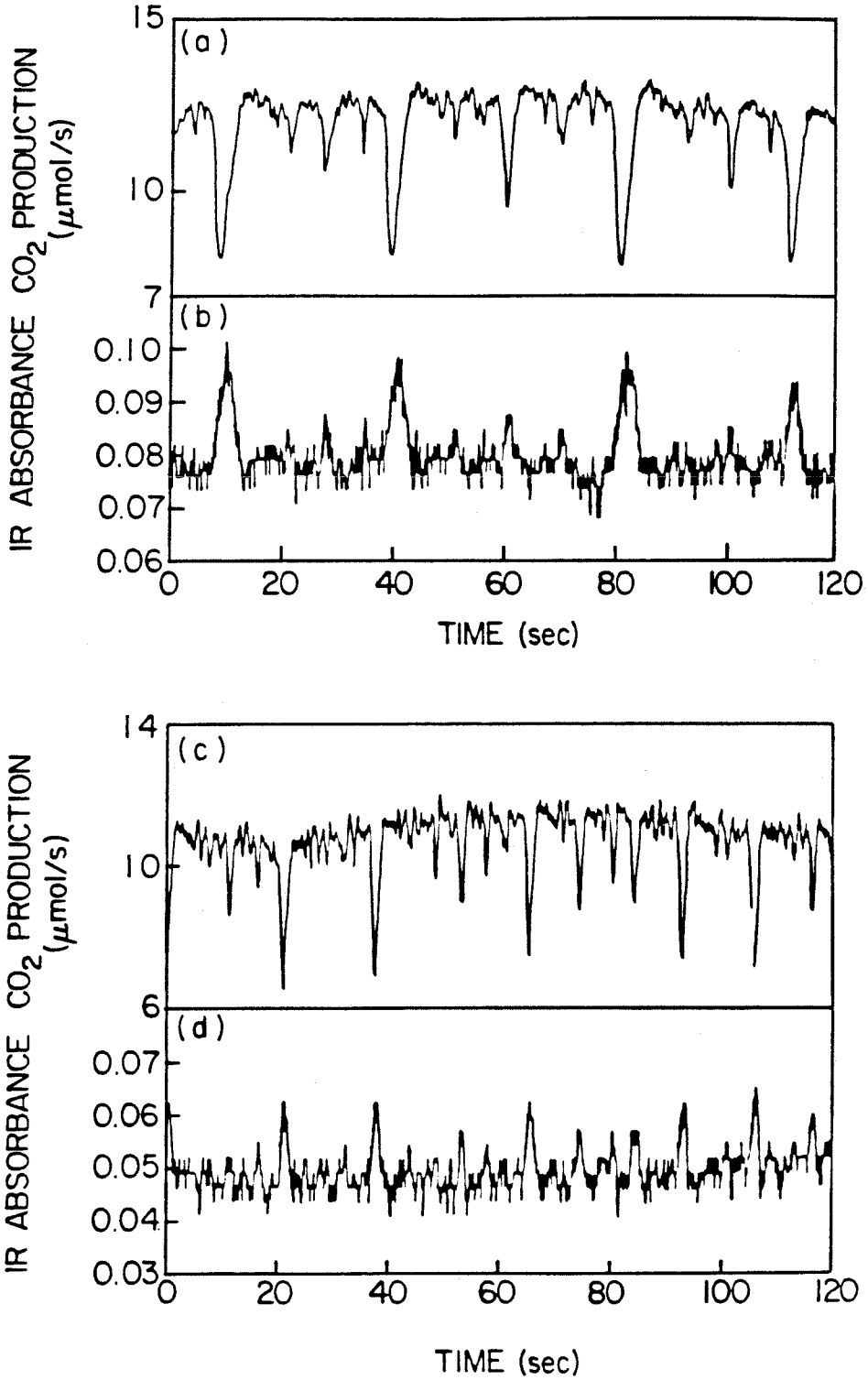
15
(a)
10
7
IR ABSORBANCE CO_2 PRODUCTION (μmol/s)
(b)
0.10
0.09
0.08
0.07
0.06
0
20
40
60
80
100
120
TIME (sec)
14
(c)
10
6
(d)
0.07
0.06
0.05
0.04
0.03
0
20
40
60
80
100
120
TIME (sec)

Figure 13

CHAPTER 7

CONCLUSIONS

A robust strategy based on steady-state, step-response, forced-cycling, and feedback-induced bifurcation techniques has been proposed for dynamic modeling of heterogeneous catalytic reactions. Used alone, any one of these techniques could yield an inaccurate description of the overall reaction. However, a model which accurately describes data from such a wide variety of experiments would almost certainly be reliable for design, control, and dynamic optimization purposes. Since specific conclusions for each process studied are presented in the previous chapters, this section will concentrate on general conclusions concerning the experimental modeling strategy.

The feasibility of feedback-induced bifurcation studies for catalysis modeling has been demonstrated. Feedback-induced bifurcation experiments are systematic and relatively simple to perform and analyze. Hopf bifurcation experiments can illuminate system characteristics unnoticeable through step-response methods. Also, Hopf bifurcation data provide sensitive information for model discrimination and are useful for estimating certain model parameters and time constants. Feedback-induced steady-state bifurcation experiments can be used to discriminate among rival models as is shown in Chapter 4 for ethylene hydrogenation on 0.5% Pt/Al_2O_3. They also provide a very systematic means for acquiring steady-state reaction rate data over a wide range of gas compositions. Steady-state bifurcation experiments also provide a simple understanding of the common phenomenon of imperfect (cusp) bifurcation.

Unfortunately, any application of the feedback-induced bifurcation technique utilizing gas-phase measurements and feed composition manipulations will be affected rather severely by transport lag (time delay) within the closed-loop system. As was shown in Chapter 2, time delay can be useful as a parameter for investigating bifurcation behavior of simple systems. However, in general, time delay is undesirable because it tends to mask dynamic contibutions from more important elements in the system. This problem can, to some extent, be overcome by acquiring,

experimentally, a very large portion of the Hopf stability boundary. In particular, regions of the Hopf boundary near the steady-state stability boundary yield sensitive data for a significant range of time scales. Feedback-induced Hopf bifurcation experiments will, in general, be most useful for studying systems involving several quite different time scales.

Future uses for the technique of feedback-induced bifurcation include feedback to gas feed composition based upon surface infrared measurements and application to biological fermentation reactors (O'Neil and Lyberatos, 1986). Surface infrared studies should be particularly enlightening since the applied feedback will necessarily cut across the system through the highly nonlinear processes of adsorption, desorption, and surface reaction. Application to bioreactors will have the advantage that time delay can be ignored because of the very large time scales typically associated with biological kinetics.

Forced concentration cycling over a range of forcing periods probably provides the most discriminating data for catalysis modeling. Start-up transients provide information akin to that obtainable using step-response methods, while time trajectories and time-average rates for (steady) periodic operation at a variety of forcing periods provides information concerning the interaction of processes occurring on several time scales. In addition, forced-cycling can suggest possibilities for productivity and/or selectivity enhancements by nonsteady operation. Unfortunately, it is difficult to use forced-cycling experiments for model development. Utilization of cycling data in most cases requires sophisticated numerical simulations in trial-and-error fashion. For these reasons forced-cycling data are used most effectively for fine-tuning of a predetermined, good model (e.g., developed using steady-state, step-response, feedback-induced bifurcation, and surface infrared techniques) and final model validation.

It is important to mention that, although the four techniques combined provide an excellent basis for model validation, it is sometimes necessary to resort to experiments aimed at exploring

specific details concerning the reaction mechanism and kinetics. Such was the case for ethylene hydrogenation on 0.05% Pt/Al_2O_3 where the applied strategy produced a serious discrepancy in the model. The discovery of this discrepancy prompted the infrared study of hydrogen spillover in Chapter 5.

A strong program in catalysis modeling must have as its foundation a synergistic interaction utilizing principles and techniques from both catalysis science and chemical reaction engineering.

REFERENCE

O'Neil, D.G., and G. Lyberatos, (1986). Feedback identification of continuous microbial growth systems. *Biotech. and Bioeng.* **XXVIII,** 1323-1333.